PROCESSING OF A HYBRID SOLID OXIDE FUEL CELL PLATFORM

A Dissertation
Presented to
The Academic Faculty

By

Raymond H. Oh

In Partial Fulfillment
Of the Requirements for the Degree of
Doctor of Philosophy in the
School of Materials Science and Engineering

Georgia Institute of Technology

May 2006

Processing of a Hybrid Solid Oxide Fuel Cell Platform

Approved by:

Dr. Joe Cochran, Advisor
School of Materials Science and
Engineering
Georgia Institute of Technology

Dr. Hamid Garmestani
School of Materials Science and
Engineering
Georgia Institute of Technology

Dr. David McDowell
School of Mechanical Engineering
Georgia Institute of Technology

Dr. Thomas Sanders
School of Materials Science and
Engineering
Georgia Institute of Technology

Dr. Robert Speyer
School of Materials Science and
Engineering
Georgia Institute of Technology

Date Approved: December 7, 2005

===

Acknowledgements

I would like to thank Dr. Joe Cochran for being a wonderful advisor over the course of my masters and doctoral studies. His continual guidance, optimism and insights allowed me to reach completion of my academic research career. I would like to also thank Dr. Tom Sanders for continuing to push, challenge and expect better things from me. Dr. David McDowell and Dr. Robert Speyer were always patient and willing to share their wisdom and insights on all things mechanical, thermal and thermomechanical. Discussions with Dr. Hamid Garmestani led me down the path of studying and understanding XRD stress measurements. I am also very grateful to Dr. Jim Lee and Richard Schaeffer for their assistance with successful experiments and bailing me out of unsuccessful ones. The rest of the Georgia Tech MSE faculty and staff have continued to be supportive and encouraging in all matters academic and administrative. Thank you.

In terms of constructing this work, I would like to express my appreciation to Dr. Iuliana Dragomir-Cernastacu for assistance and discussions regarding XRD stress measurements. Jason LeMasters and Ben Dempsey provided much framework and insight into the world of finite element modeling. Thanks to Louis Ferranti for help with wave speed measurements and letting me beat him on our 5K runs.

I would like to recognize the many graduate students I have encountered within the Sanders/Cochran group for their continual help, support, humor, and friendship: Justin Clark, Kevin Hurysz, Jason Nadler, Ben Church, Tracie Durbin, Le' Hayes, Tammy McCoy, Monique McIntosh, Wes Seay, Matt Trexler, Peter Chamberlain,

iii

Michael Middlemas, and Chris Rocket. Additional thanks go towards Greg Kennedy, Jeff King, Silvia Liong, and Curtis Neff.

My parents have never ceased in their encouragements and prayers. I would not be where or who I am without them. My sister Rebecca continues to be my verbal punching bag yet still remains a loving friend. She is a much better person than I. Thank you to all of my friends at KCPC for providing a Christ centered community and many wonderful memories. Finally I would like to thank Esther Hong for so many things, but especially for her patience, understanding and continual belief in me.

Table Of Contents

List of Tables

List of Figures

Summary

Solid oxide fuel cell platforms consisting of alternating cellular layers of yttria-stabilized zirconia electrolyte and Fe-Ni metallic interconnects (Fe45Ni, Fe47.5Ni, Fe50Ni) were produced through the co-extrusion of two particulate pastes. Subsequent thermal treatment in a hydrogen atmosphere was used to reduce iron and nickel oxides and co-sinter the entire structure. Issues surrounding this process include the constrained sintering of the layers and the evolution of residual stress between the dense, fired layers.

Sintering curves for individual components of the layers were measured by dilatometry to ascertain each material's impact on overall sintering mismatch. X-ray diffraction, scanning electron microscopy and weight loss were utilized to examine phase evolution within the Fe-Ni alloys during reduction. YSZ powders densified above ~1050°C and shrinkage was rapid above the sintering temperature. Shrinkage of the interconnect occurred in two stages: reduction and the initial stages of sintering concluded around ~600°C, plateauing shortly and continuing at ~900°C as pore removal and grain growth ensued simultaneously. Constrained sintering resulted in the formation of remnant porosity within the interconnect layers.

Interconnect compositions were chosen in efforts to minimize disparities in thermal expansion with the electrolyte. Residual strains on the surfaces of the layers were measured by x-ray diffraction. Corresponding stresses were calculated using the $\sin^2\psi$ method. Grain growth within the interconnect prohibited random planes to be measured so stress measurements were confined to the ceramic layers.

Various material properties such as thermal expansion were collected and employed in a modified finite element model [1] to estimate residual stresses in the platform. A method for determining a crucial parameter, the "zero stress temperature" was outlined and incorporated. Modeled values were found to agree well with XRD values, providing indirect confirmation of the zero stress temperature calculations. Discrepancies were attributed to microcracks found within the layer that arose due to residual stress values surpassing the tensile strength of the zirconia.

1   Introduction

With its promises of highly efficient and environmentally friendly energy, fuel cells have remained a constant topic of research and scientific discussion. Research interest continues to increase as the need for an alternative, clean energy source grows. The principles behind fuel cells are not new; Grove reported the first operational fuel cell in the early nineteenth century [2] and the underlying ideas have continually developed since then.

Fuel cells operate on electrochemical principles. Their energy is derived from the reduction/oxidation reaction of a fuel such as hydrogen and an oxidant such as oxygen. The efficiency of a fuel cell is dictated by factors regarding the kinetics and driving forces of the electrochemical reactions. These factors can be improved through the introduction of superior materials and enhanced processing techniques.

The primary goals of this work focus on the latter of these two. While concerns often surround how the material components will perform in the fuel cell operating environment, their successful production is not an insignificant matter. If the fuel cell cannot be manufactured, how the materials operate under fuel cell conditions becomes moot. A novel process designed to fabricate metallic honeycombs from oxide precursor extrusions (Section 2.3.1) has been expanded to allow for the production of cellular, multi-layer co-extrusions. An end product consisting of alternating layers of a solid-state electrolyte (yttria-stablized zirconia) and metallic interconnect (Fe-Ni alloys) provides a

self-contained fuel cell platform. Subsequent deposition of electrodes in the inner cell walls forms the finished fuel cell.

The introduction of an interface between two materials creates several processing issues. Extrusion shapes particulate pastes to a desired form. These must subsequently be sintered to densify and impart strength on the final product. When adjacent, joined ceramic components are initially heated together, a *co-sintering* condition arises where the sintering behavior of each component influences the densification of all components in the overall system. The sintering behavior of the ceramic powders that comprise each component must be fully understood to manipulate the density of each component in concert with one another. For metal interconnects produced by reduction of oxides, the associated shrinkage will also affect the sintering kinetics and final densification. Co-sintering can be considered a "heat-up" issue since sintering occurs as a powder compact is fired. However, components are also affected during the "cool-down" portion of the process. At this point, the components are presumably dense, each with their own respective materials properties. Residual thermal stresses result if the rates of thermal contraction between the materials are too large. Thermal expansion thus becomes an important consideration not only for maintaining structural integrity during operation, but throughout processing as well.

This research is thus divided into two separate portions. The first investigates methods to comprehend and minimize the differences in the densification of the electrolyte and interconnect materials. Dilatometry studies (Section 3.5) were conducted to observe how each individual component shrinks as well as how various modifications alter their sintering behavior. For the multi-component interconnect, characterization

using x-ray diffraction and electron microscopy was conducted during various points of the firing curve to track the development of various phases and microstructures. (Section 4.5)

Material selection for the electrolyte and interconnect largely stemmed from the second concern of this research. Yttria-stablized zirconia (YSZ) is the most common solid-state oxygen ion conducting electrolyte. Its properties are well defined and it has been exhaustively studied. Because of this, preliminary investigations began with a search for an interconnect that could match with the properties of YSZ. With the advent of improved processing and new potential electrolyte materials, operating temperatures for fuel cells have dropped to the point where alloys could be considered for interconnect materials. Research interest in this realm has grown and a number of investigators have investigated the properties of a number of potential alloys. Initial results indicated that Fe-Ni binary alloys could have a thermal expansion match amenable to processing with YSZ.

As discussed previously, thermal expansion differences lead to inherent stresses that remain after firing. The second portion of this work seeks to gain a deeper understanding regarding the residual stress in the platforms. Three interconnect compositions close to the Fe50Ni binary alloy were co-extruded with YSZ to examine the influence of thermal expansion on residual stress.

X-ray diffraction (Section 3.7) was used to measure residual stresses on the outer walls of the platforms using the $sin^2\psi$ method. Measurements in the ceramic layer were taken both parallel and perpendicular to the extrusion direction at various locations.

One question of interest surrounding residual stress involves the temperature at which the residual stress initially starts to build on cooling. It is often presumed that diffusional mechanisms such as creep, plastic flow and recrystallization operate at higher temperatures to fully relax ceramic and ceramic/metallic laminates. At a critical temperature, these mechanisms cease to exist, and residual stresses increase from this point. Knowledge of this temperature would give insight into relaxation mechanisms as well as allow for more accurate modeling and improved heat treatment. Section 3.9.1 outlines an analysis for determining this "zero stress" temperature.

LeMasters [1] developed a finite element model to simulate and study the evolution of stress during the initial and steady state operation of these multi-layered fuel cells. With additional refinement, this model could also be implemented to simulate the building of residual stress during processing cool down. Using the data collected here, LeMasters' work is built upon by implementing his model to compare experimental and simulated residual stress values. This is further elaborated upon in sections 4.7 and 4.8.

This work is a reflection of both engineering and science. While its motivation is rooted in obstacles surrounding processing of the solid oxide fuel cell platform, the issues examined in this work can be extrapolated to other similar problems. Co-sintering and residual stress are a concern for any multi-component fuel cell system, electronics, and structural laminate materials.

2   Background and Literature Review

2.1   Solid Oxide Fuel Cells

Fuel cells are devices that generate energy from the electrochemical conversion of a fuel

and oxidant [3]. A basic fuel cell is comprised of three components: (Figure 2.1) an

electrolyte sandwiched between two electrodes (an anode and cathode). Under operating

conditions, fuel enters and is oxidized at the anode portion of the cell, liberating

electrons. Electrical power is produced as electrons flow from the anode to the cathode.

Oxidant on the cathode side accepts electrons and is reduced to an ionic species. The

circuit is completed by the diffusion of oxidant ions through the electrolyte. In practice

fuel cells are not used individually, but in modular stacks where a fourth component-an

electrical interconnect joins the individual cells. Since the reactants are often in the

gaseous state, the interconnect usually serves to separate fuel and oxidant as well.
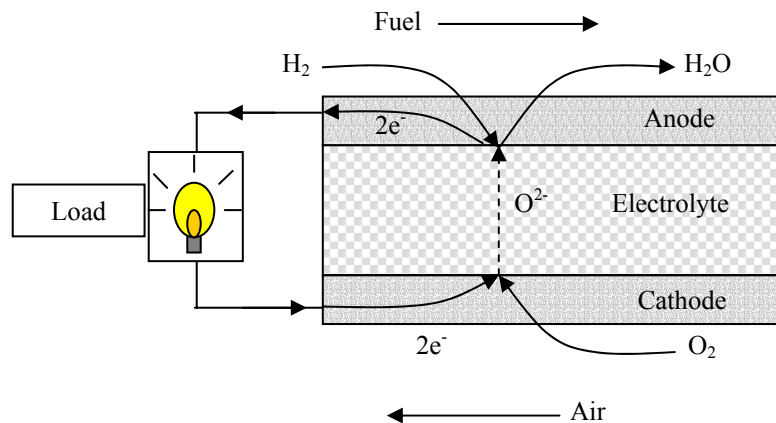
Figure 2.1 Schematic of hydrogen solid oxide fuel cell components and the principles of fuel cell operation.

Since the energy stored in the fuel is converted electrochemically and not through combustion, it is not subject to Carnot cycle limitations, so the energetic efficiency of a fuel cell is significantly higher (~50%) [4, 5]. If the heat produced by the fuel cell is recaptured, efficiencies can reach ~80%. Fuel cells also produce much less polluting byproducts than traditional combustion processes. Additional advantages of fuel cells previously mentioned include their modular construction and potential for cogeneration of energy (electrical and thermal) [3].

For a basic hydrogen fuel cell, the electrochemical reactions can be summarized as [2]:

$$H_2 \rightarrow 2H^+ + 2e^- \tag{2.1.1}$$

$$O_2 + 4e^- \rightarrow 2O^{2-} \tag{2.1.2}$$

$$2H^+ + O^{2-} \rightarrow H_2O \tag{2.1.3}$$

The sum of these reactions gives an overall reaction:

$$H_2 + \tfrac{1}{2}O_2 \rightarrow H_2O \tag{2.1.4}$$

For which the Gibbs free energy is defined as:

$$G = G^o + RT \ln\left(\frac{a_{H_2O}}{a_{H_2} a_{O_2}^{1/2}} \right) \tag{2.1.5}$$

where a_x is the activity of species "x", G^o is the Gibbs free energy of formation and R is the gas constant. The Gibb's free energy is related to the electrical work of the cell as:

$$\Delta G = -nFE$$

(2.1.6)

where F is Faraday's constant, E is the voltage of the fuel cell and n is the number of electrons generated and consumed in the complimentary reactions. Substituting Equation 2.1.5 into Equation 2.1.6, we obtain the Nernst equation:

$$E = E^o - \frac{RT}{nF} \ln \left(\frac{a_{H_2O}}{a_{H_2} a_{O_2}^{1/2}} \right)$$

(2.1.7)

where E^o is the open circuit voltage (OCV), the potential of the unloaded cell. For a fuel cell to perform, current must be drawn from the cell, however in practice operating voltage drops as the current density increases. This voltage drop, or overpotential/overvoltage results from irreversibilities or losses due to kinetics of the electrode reactions [6, 7]. Fuel cell efficiency is improved through the minimization of the aforementioned overpotentials. This is achieved through the development of superior materials or enhanced processing techniques.

2.2   SOFC Materials

2.2.1   Electrolyte

Fuel cells can be categorized by their operating pressure and temperature regime or by the type of fuel they use, but most often fuel cells are classified by their electrolyte material. As its name implies, solid oxide fuel cells (SOFC) employ a solid state doped oxide as the electrolyte. The dopant atoms form oxygen vacancies within the lattice structure, which allow O^{2-} ions to conduct through the electrolyte. These materials were first reported by Nernst [8] in the late nineteenth century as he searched for a replacement for refractory metal filaments. To achieve adequate ionic conductivity, SOFC's are run at much higher temperatures (800-1500°C) compared to other fuel cells.   High temperature operation also improves efficiency through enhanced conversion of the fuel, but it also places more rigorous constraints on the material components used in the SOFC. SOFC's are often referred to as ceramic fuel cells since these are generally the only materials that remain chemically and mechanically stable at the high operating temperatures. The most common solid-state electrolyte is yttria-stabilized zirconia (YSZ) [3, 9]. Although a variety of other oxides (i.e. scandia-stabilized zirconia, gadolinia-doped ceria) [5, 10, 11] have also been investigated for fuel cells, none of these provide as good a balance of chemical stability, mechanical strength and ionic conductivity as YSZ.

2.2.2   Electrodes

For electrodes, doped lanthanum manganites are commonly used for cathodes since these materials have good oxidation resistance and electronic conductivity. Lanthanum

manganite is a perovskite material that is doped with strontium or other lower valence cations. The dopant concentration provides a range of conductivity and thermal expansion that can be adjusted for optimal processing and operational properties [3].

The anode must facilitate the adsorption and oxidation of hydrogen from the fuel, so it must be an electronic conductor. Since anodes are subject to a reducing atmosphere, metals can be used as anode materials, and Ni/YSZ and Co/YSZ cermets provide a good balance between conductivity and expansion match with other components [12].

2.2.3   Interconnect

The SOFC electrical interconnect is the most complex of the four fuel cell components. The operating conditions of the fuel cell create stringent requirements for the material that are well documented [13-15]. The interconnect must be stable in both the reducing and oxidizing atmospheres of the anode and cathode and dense enough to separate gases on either side of the cell. It must be a good electronic conductor and be chemically and thermally compatible during processing and operation with the other components of the cell. Doped lanthanum chromites meet most of the above requirements and have proven to be suitable for conventional ceramic fuel cells. However the largest drawbacks for these materials are their high cost and poor sintering behavior, which prevents their gastightness [3].

Metallic alloys have usually been exempt from consideration as interconnects because of oxidation/corrosion problems at the higher fuel cell operating temperatures, which are necessary to achieve adequate conductivity in the electrolyte. However, with the advent of improved electrolyte conductivity, both through processing and design (i.e. thinner layers) [16], and superior materials [10, 11], fuel cell operation can now occur at

temperatures suitable for alloy interconnects (600-800°C). The high electrical conductivity, ease of formability, and lower cost of metals and alloys make this a welcome development.

The majority of alloys currently investigated for fuel cell interconnects are comprised of various binary and ternary compositions based on the Fe-Ni-Cr ternary system [13, 15, 17]. These are summarized in Figure 2.2. Alloy selection is usually approached from the perspective of first finding an alloy with sufficient oxidation resistance and a good match in thermal expansion [17-19]. Additional concerns such as interfacial reactions with other components, [17] thermodynamic stability of the scale, [20] scale conductivity [21] and reasonable costs while important, are often secondary considerations. Adequate oxidation resistance is necessary to preserve the electrical conductivity and gas sealing properties of the metal. As alloying elements, chromium and aluminum provide continuous adherent oxide scales that prevent further oxidation. Since alumina is considered an insulating oxide, the majority of interconnect alloy candidates researched are chromia formers [15]. The addition of small amounts of certain rare earth elements (Y, La) have been well documented in improving the oxidation protection properties of chromium [22]. These rare earth elements are believed to promote the initial formation of an oxide layer as nucleation sites and serve as retardants for the diffusion of scale forming elements.
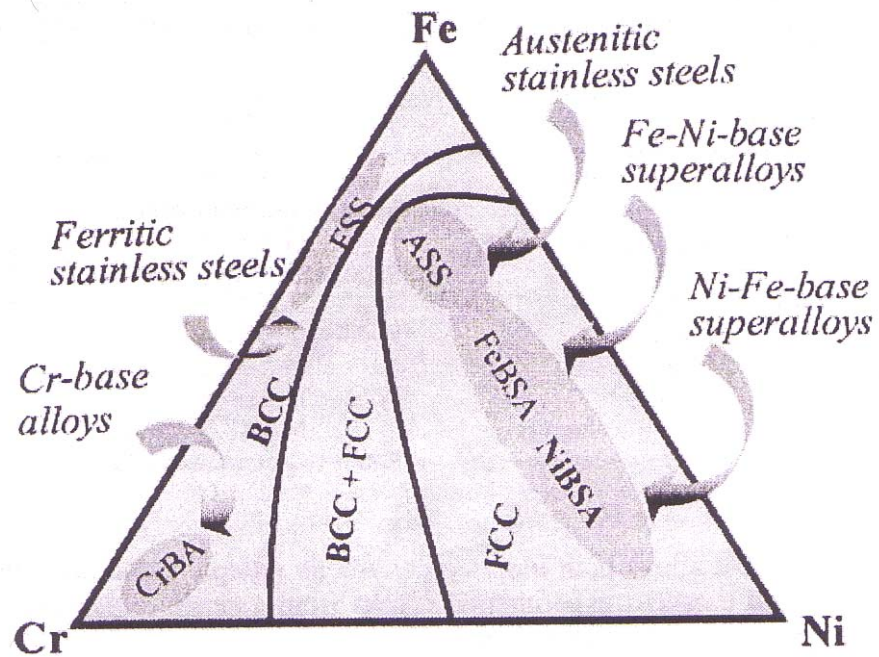
Figure 2.2 Potential fuel cell interconnect alloys based on the Fe-Ni-Cr ternary system [15].

2.2.4 Fe-Ni Alloys

Iron and nickel lie adjacent to one another on the periodic table and so it is unsurprising that they form solid solutions (α, γ (Fe,Ni)) or other substitutional cubic phases (FeNi$_3$). One interesting aspect of this system is the change in crystal structure from the iron rich BCC alloys to the nickel rich FCC alloys. As Figure 2.2 indicates, Fe-Ni alloys are considered for fuel cell interconnect applications as the basis for superalloys. Nickel is well known to serve as the foundation for corrosion resistant, high temperature alloys and iron is often an addition to reduce costs. The binary alloys alone are generally not considered since this system fails to produce an adherent and protective oxide layer. The oxides of iron (FeO, Fe$_2$O$_3$, and Fe$_3$O$_4$) form non-uniform layers that spall under fuel cell conditions. NiO similarly does little to impede diffusion and protect the alloy. Due to these reasons, little attention has been paid to this system for interconnects.
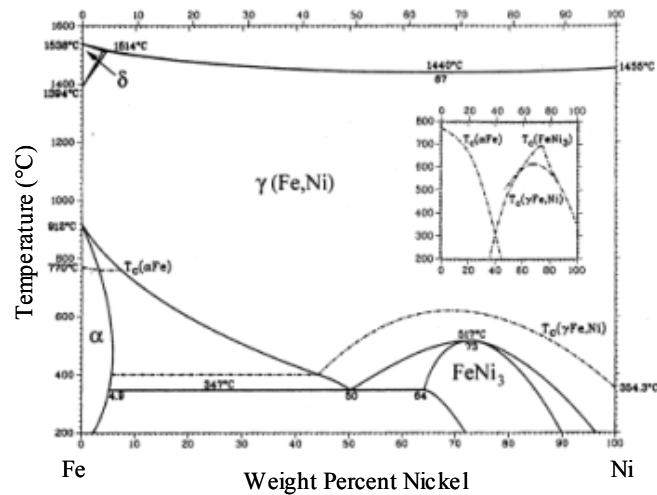
Figure 2.3 Fe-Ni binary phase diagram, after [23].

However, the Fe-Ni binary is well known for another reason altogether. The intriguing thermal expansion behavior of this system is well established and has been extensively studied. In 1897 Guillaume discovered the thermal expansion behavior of Fe-Ni alloys containing ~35 wt% Ni [24]. These alloys were quickly given the name "invar" to indicate the thermal expansion behavior being *invar*iable with temperature. The material quickly found use in precision areas where the reduction of thermal expansion would be useful. Many more compounds and systems (i.e. FePt, FeNiCo) have been found since then that also exhibit invar type properties.

Despite the large amounts of research devoted to the subject, a full understanding and explanation of the invar effect still eludes the realm of solid state physics. It is generally agreed that the presence of two spin states forms the basis for the invar effect: a low spin/low volume (paramagnetic) state and a high spin/high volume (ferromagnetic) state. The energy between the two states decreases with increasing nickel concentration. At a critical composition, thermal excitation between these two states counteracts the thermal lattice expansion [25, 26]. This phenomenon is not limited to expansion, but to other properties of the alloy including bulk modulus (elinvar effect), lattice parameter, heat capacity and magnetization [27].

Figure 2.4 indicates that the invar effect disappears with an increase in temperature with the effect essentially eliminated above 600°C. It is also observed that the average CTE forms a valley around the invar composition and that the CTE can be manipulated by simply varying the composition. This phenomenon serves as the basis for investigating alloys with a thermal expansion match with the YSZ electrolyte. The

average CTE of YSZ is ~10.5 x 10^{-6} K^{-1} and Figure 2.4 shows that a composition of Fe50Ni would have a good CTE match.
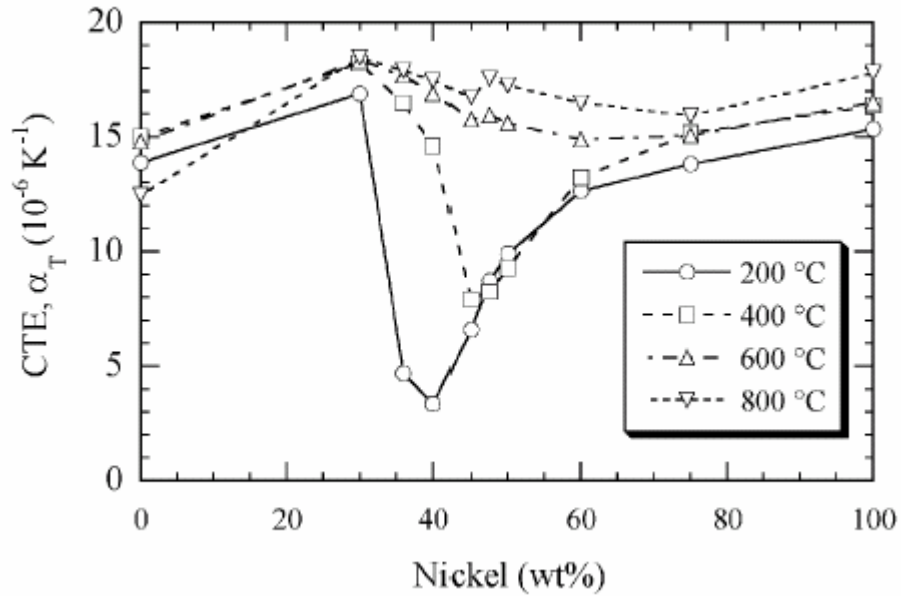
Figure 2.4 Average CTE values for FeNi alloys at various temperatures. The lines only serve to illustrate trends and do not reflect continuous data points. [14]

As mentioned previously, this system would likely suffer from poor oxidation resistance. The design approach would thus be to initially find a base alloy with a good expansion match and then work towards additional alloying or processing methods that could improve the oxidation resistance of these materials without sacrificing the desired thermal expansion behavior.

2.3   Solid Oxide Fuel Cell Fabrication

In conventional fuel cell fabrication, one particular component (typically the anode [3, 16]) serves as a structural support and the other components are sequentially added. The support must be mechanically robust, so a thicker, denser substrate is desirable. However, this is often contrary to other desirable properties of the components. For example, it is desirable for the electrolyte to be as thin as possible to achieve superior conductivity. To enhance reaction kinetics, the anode and cathode should be porous for a larger gas/electrolyte/electrode reaction interface. Supports are often produced through traditional ceramic processing methods such as extrusion, tape casting, or tape calendaring.   Additional segments of the fuel cell are added through a variety of techniques such as screen-printing, slurry coating, and chemical vapor deposition. Traditional geometries include planar and tubular designs, which are illustrated in Figure 2.5 and Figure 2.6 respectively. Each have their own advantages/disadvantages and unique challenges. The planar design provides higher power density whereas the tubular design does not require seals and forms good barriers for gas separation.

2.3.1   Extrusion

For both the tubular and planar design, extrusion has been found to be a sound method to produce uniform substrate materials. Extrusion is a process where a material flows and plastically deforms to achieve a desired geometrical cross section [28]. The main advantage of this technique is that long lengths of material can be created with a
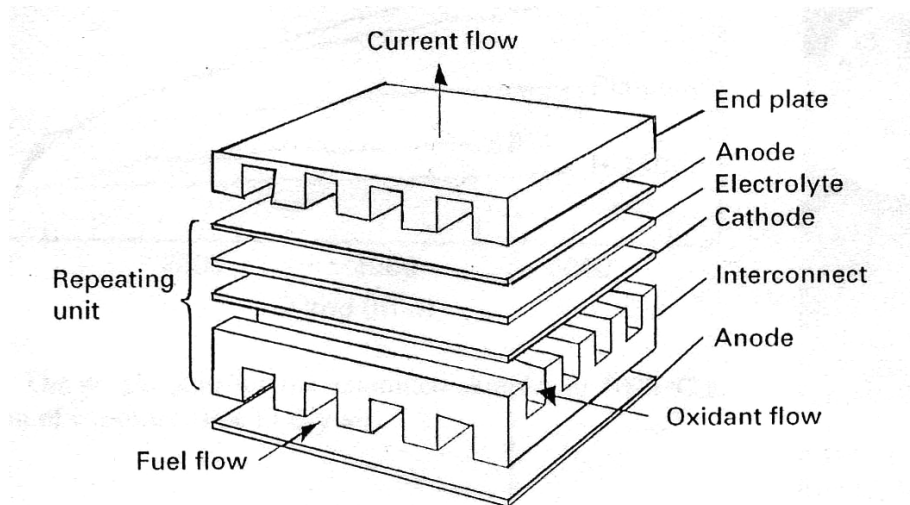
Figure 2.5 Planar solid oxide fuel cell configuration [29].
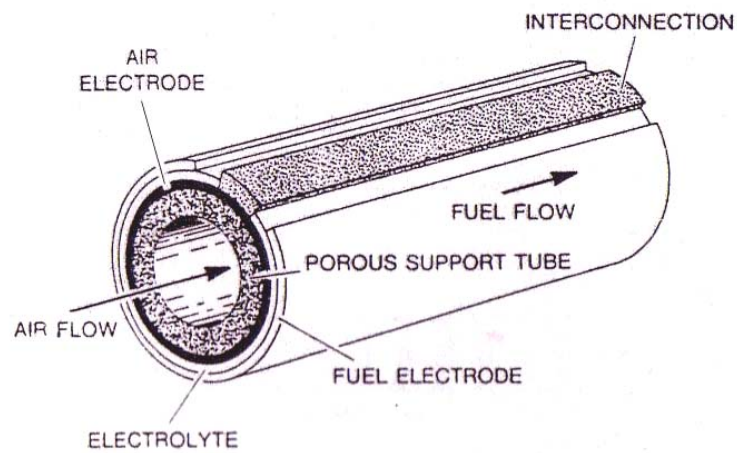
Figure 2.6 Tubular solid oxide fuel cell configuration [3]. In this example, fuel cell components are sequentially deposited on a separate, porous support tube.

reproducible, constant cross section. The cross section can consist of simple square and circular geometries or can be comprised of complex honeycomb (cellular) arrays.

For ceramic processing, particulate powder(s) are combined with a binder, lubricant and liquid to form a plastic, cohesive paste. The paste is driven across a die where it conforms to a particular cross section as outlined by a die. The extruded cross sections are then carefully cut, dried and fired to remove the processing additives and sinter the green piece. Further details of ceramic paste extrusion are covered by Benbow and Bridgwater [28]. The quality of paste extrusion is governed by the design of the die and the rheological properties of the paste. Concerns with the die are mainly geometrical-reduction/expansion in cross sectional area of flow, dimensions of the channels, surface area, etc. [30] Rheology describes how the paste itself will flow and deform and is influenced by a variety of parameters.

The two parameters that characterize the rheology of a paste are its bulk yield shear stress (σ_o) and wall shear stress (τ_o), both of which are highly influenced by the ratio of solid and liquid phase, or the volumetric solids loading of the paste [31]. The bulk yield shear stress is the amount of stress necessary for the paste to shear against itself as flow contracts from larger to smaller cross sectional areas. The wall shear stress accounts for the amount of pressure necessary to overcome the drag imposed by the surface area of the walls within the die land. (The drag imposed by the walls of the barrel is usually considered negligible.) Typical ranges for σ_o and τ_o are 50-1500 kPa and 0-150 kPa respectively [30, 31]. Hurysz [31] has suggested that pastes with yield stresses in the range of ~300-600 kPa are optimal for extrusion. These characteristic parameters are determined by capillary rheometry [32]. A capillary rheometer is a simple ram extruder

with interchangeable dies. Extrusion pressure is recorded as a function of the load crosshead velocity and die geometry. The yield shear stress and wall shear stress can then be derived from the Benbow and Bridgwater equation [28]:

$$P = 2(\sigma_o + \alpha V)\ln\left(\frac{D_o}{D}\right) + 4(\tau_o + \beta V)\left(\frac{L}{D}\right)$$

(2.3.1)

Where P is the extrusion pressure, V is the velocity of the crosshead, α and β are velocity related parameters, D_o and D are the diameters of the barrel and die land respectively, and L is the length of the die land. (Figure 2.7)
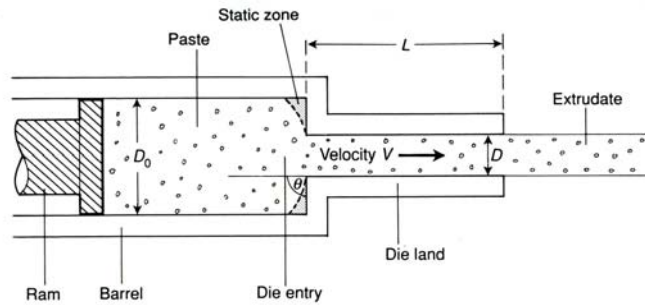
Figure 2.7 Schematic of die barrel and land parameters used in the calculation of Benbow and Bridgwater equation [28].

2.3.2 Co-Extrusion

The previous discussion of extrusion has dealt with pastes of a single composition. Hybrid, or co-extrusion produces a layered body comprised of two or more pastes of different compositions. To achieve this, individual pastes are either fed into separate barrels [33, 34] with the two bodies joining at a point within the die or they are placed together in the same barrel with a particular configuration (i.e. pre-layered) and extruded as such [35].

18

Several researchers have demonstrated the viability of the process for the fabrication of solid oxide fuel cells. Liang and Blackburn demonstrated co-extrusion of bilayered [34] and trilayered [36] ceramic tubes of sequential fuel cell materials. Rauch *et al*. [33] and Cochran *et al.* [37] review a process developed at Georgia Tech that utilizes a hybrid honeycomb geometry where alternating square cellular layers of an interconnect precursor oxide(s) and electrolyte paste are simultaneously extruded and thermally processed. The precursor oxides are reduced in hydrogen to form a metallic interconnect, and the final structure is a linear, cellular fuel cell support that can be easily stacked. (Figure 2.8) The cell walls provide a support for electrode deposition and serve as chambers for fuel and air flow. The thin walls of the cells also reduce the impedance of the electrolyte and allow for lower temperature operation of the fuel cell. This fuel cell construction is the basis for this study.
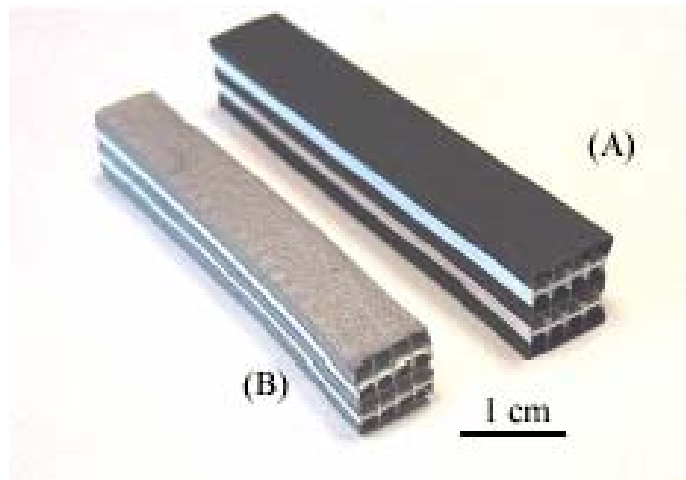
Figure 2.8 A.) Green and B.) Fired hybrid 4x4 honeycomb SOFC structure (YSZ electrolyte, FeNiCr interconnect alloy).

2.3.3   Oxide Reduction

To obtain the final metal interconnect, any green oxides comprising this layer must be reduced. An oxide's propensity towards reduction is determined by its thermodynamic stability against the temperature and pressure surrounding it. These are summarized in Ellingham diagrams, which outline oxide stability (free energy) as a function of temperature and pressure. As previously implied, reduction of iron, nickel and chromium oxides are of significant interest for fuel cell applications.

The reduction of iron oxides is an industrially important process and is well documented [38-40]. Reduction of hematite to iron occurs as follows:

$$Fe_2O_3 \rightarrow Fe_3O_4 \rightarrow FeO \rightarrow Fe \qquad\qquad (2.3.2)$$

Dilatometry work by Nadler [41] showed that reduction of hematite (Fe_2O_3) to magnetite (Fe_3O_4) occurs with an overall expansion. (Figure 2.9) For a co-extruded structure, this results in catastrophic cracking and so the use of hematite becomes prohibited [1]. Cores *et al.* [39] examined the reduction of magnetite/nickel oxide mixtures under non-isothermal conditions (Figure 2.10) (ramp rates of 10 K/minute) under both H_2 and CO atmospheres. Under hydrogen, reduction of magnetite was found to initiate at ~350°C and finish at ~675°C. Nickel oxide reduced in the range 225°C to 350°C. For compacts containing both oxides, reduction was found to occur in two stages corresponding to the reduction of the two oxides. It was observed that the initial reduction temperature increased with increasing amounts of magnetite and the temperature at which reduction
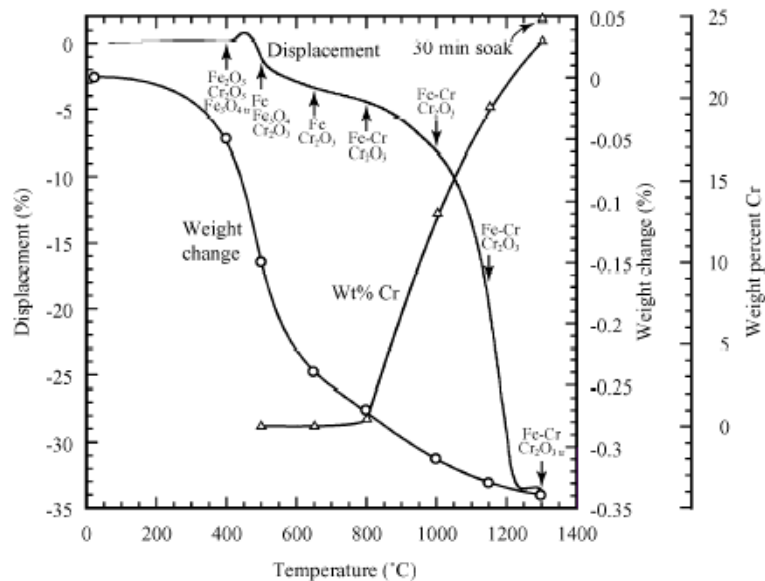
Figure 2.9 Dilatometer trace of Fe-Cr oxide honeycomb illustrating expansion associated with the Fe$_2$O$_3$ to Fe$_3$O$_4$ reduction transformation [41].

1 100%Fe$_3$O$_4$; 2 25%NiO–75%Fe$_3$O$_4$; 3 50%NiO–50%Fe$_3$O$_4$;
4 75%NiO–25%Fe$_3$O$_4$; 5 100%NiO
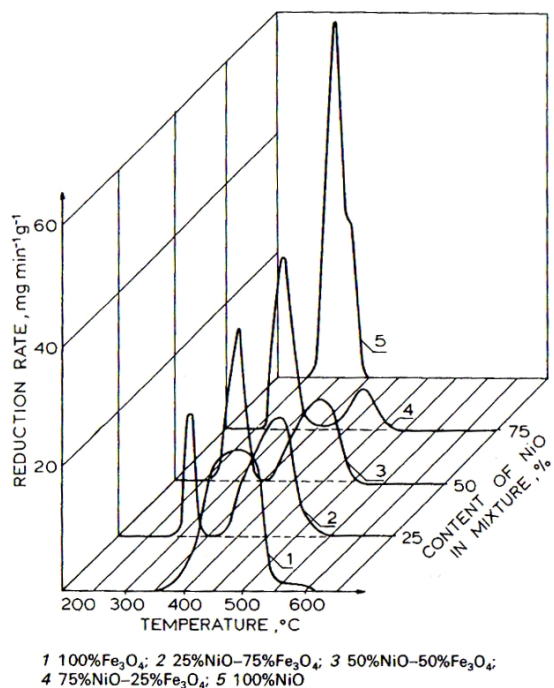
Figure 2.10 Reduction rate profile for various Fe$_3$O$_4$/NiO powder compacts. (10K/minute ramp rate.) Mixtures of the two powders result in a bimodal reduction profile with the onset and completion of reduction changing as a function of composition [39].

ended decreased with increasing amounts of nickel oxide. The delay of reduction was attributed to the formation of a reaction between the two oxides:

$$NiO + Fe_3O_4 \rightarrow NiFe_2O_4 + FeO \qquad (2.3.3)$$

The first curve then corresponds to the reduction of nickel oxide and this nickel ferrite phase. Reduction concludes at lower temperatures because of the catalytic effect of reduced nickel on the dissociation of hydrogen.

Iron and nickel both possess a cubic crystal structure. The crystal structures of Fe_3O_4 and NiO are spinel and rock salt respectively. Schematics of both lattices are illustrated in Figure 2.11 and Figure 2.12. As the oxide is reduced to metal, changes in both chemistry and structure result in a decrease of sample dimension.

Recently, several researchers have studied the feasibility of producing metal and alloy compositions from the reduction of extruded oxides. Each of these authors examined thin walled honeycomb structures. Nadler [41] studied the Fe-Cr binary system and concluded that Cr_2O_3 is at the threshold of reducibility. The presence of iron was found to foster Cr_2O_3 reduction by alloying reduced chromium. The process was limited to producing samples of ~500-600 μm in thickness and compositions up to 25 wt% chromium. Clark [42] examined two Fe-Ni based alloys (Super Invar and Maraging Steel) for energetic material capsules. Both materials were found to have mechanical properties similar to those expected for these alloys and contribute a large amount of energy to initiate and propagate chemical reactions during high strain rate loading.
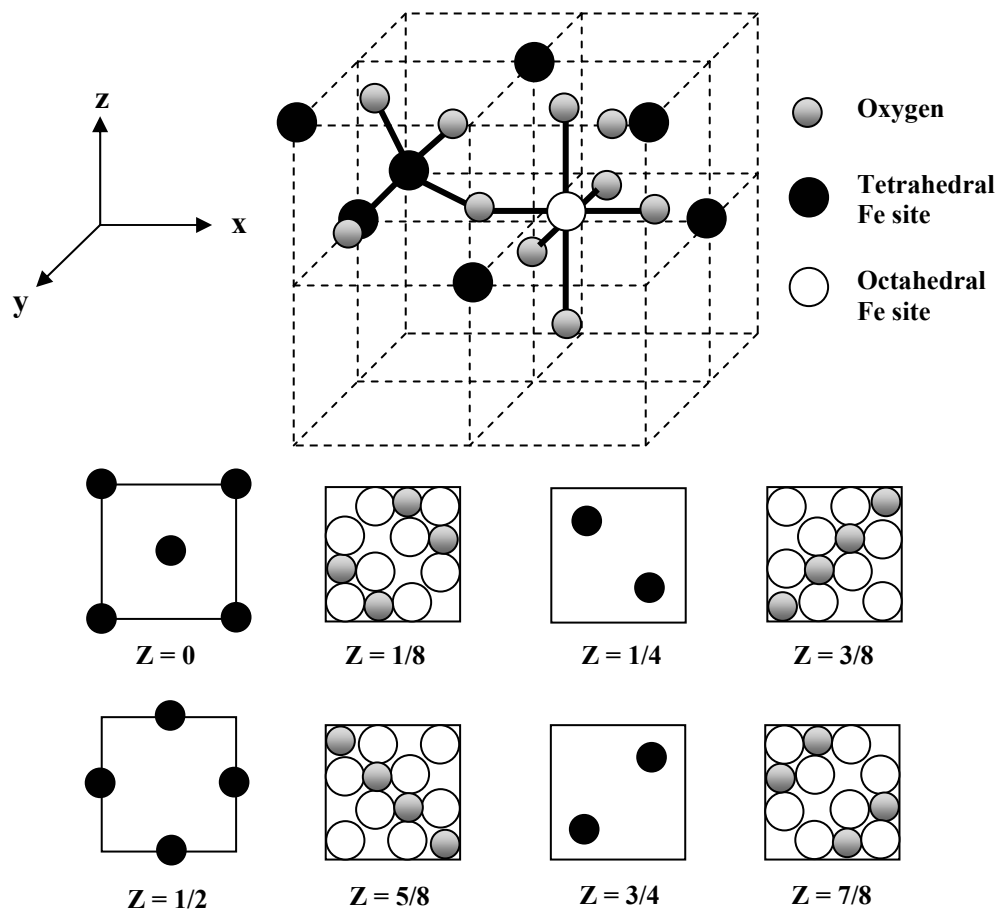
Figure 2.11 Spinel crystal structure of Fe$_3$O$_4$. Layer sequences provide additional clarification of atomic arrangement, after [43].
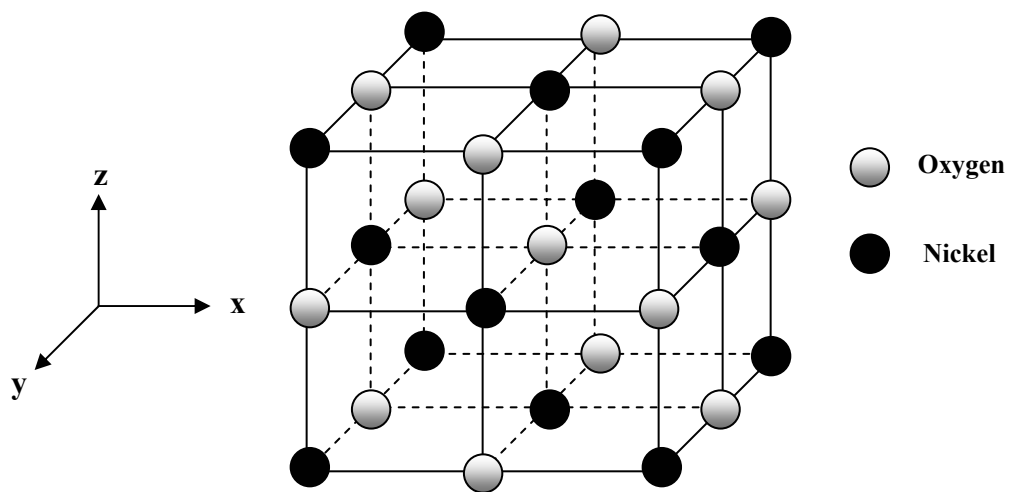
Figure 2.12 Rock salt crystal structure of NiO, after [43].

Church [14] reproduced a large number of alloys in the Fe-Ni-Cr system to study the thermal expansion and oxidation resistance properties. Compositional control of the oxide reduction process was validated through XRD lattice parameter measurements. Nadler and Church also corroborated expected compositional values through observations of expected phase transitions during dilatometeric measurements.

2.4 Co-Sintering

Green particulate compacts are weak because only an organic binder matrix and/or superficial contact forces hold the piece together. Sintering is the step where a porous network of individual particles becomes a monolithic, dense structure. The driving force behind sintering is the reduction of surface energy. This can be accomplished through an increase in average particle size, where certain particles grow at the expense of others (coarsening) or through the elimination of the particle/atmosphere interface with the corresponding creation of particle/particle interfaces or grain boundaries (densification).

The local driving force for sintering arises as a result of differences in curvature. The Gibbs-Thomson equation [44, 45] shows that the chemical potential difference for atoms under a curved surface versus those under a flat surface is given by:

$$\Delta\mu = \mu_{curved} - \mu_{flat} = \frac{2\gamma_{SV}\Omega_{MX}}{r} \tag{2.4.1}$$

where γ_{SV} is the surface/vapor interfacial energy, Ω_{MX} is the atomic volume of the MX compound and 'r' is the radius of curvature.

This equation has two implications for the sintering driving force. The first involves the partial pressure above a curved surface and the second deals with the dependence of vacancy concentration on curvature. At equilibrium, the partial pressure difference above the curved surface can be given as:

$$\Delta\mu = kT \ln\left(\frac{P_{curved}}{P_{flat}}\right) = \frac{2\gamma_{SV}\Omega_{MX}}{r} \qquad (2.4.2)$$

where 'T' is the temperature and 'k' is Boltzmann's constant. This can be rewritten to give:

$$P_{curved} = P_{flat} \exp\left(\frac{2\Omega_{MX}\gamma_{SV}}{rkT}\right) \qquad (2.4.3)$$

By convention, the radius of curvature for a concave surface is negative and positive for a convex surface, so Equation 2.4.3 shows that the partial pressure over a convex surface will be greater than that of a flat surface, which in turn is greater than that of a concave surface. This pressure gradient that arises between the two surfaces thus provides the first driving force.

The equilibrium concentration of vacancies under a flat, stress free surface follows an Arrhenius equation:

$$C_o = A\exp\left(\frac{-Q}{kT}\right) \qquad (2.4.4)$$

where 'A' is a pre-exponential constant and 'Q' is the enthalpy of formation of a vacancy. For a curved surface, the chemical potential of the atoms changes following Equation 2.4.1, which also alters the value for Q:

$$C_{curved} = A \exp\left(\frac{-Q + \Delta\mu}{kT} \right) = C_o \exp\left(\frac{2\Omega_{MX}\gamma_{SV}}{rkT} \right) \qquad (2.4.5)$$

Following a similar rational as with the partial pressure, it can be shown that the vacancy concentration is greater under concave surfaces compared to convex surfaces. The pressure and vacancy gradients are thus seen to be the local driving force for mass transport of material from regions of higher curvature (surfaces) to that of areas of lower curvature (necks).

Whether a material densifies or coarsens is dependent on the dominant mass transfer mechanism(s). The mechanisms responsible for atomic transfer in particle compacts are:

- *Evaporation-condensation*
- *Surface Diffusion*
- *Volume/Bulk Diffusion*
- *Grain boundary diffusion*
- *Plastic Flow/Creep*

Only those mechanisms that promote the particle centers drawing closer together will shrink and densify the material [44]. These are those mechanisms where mass is transferred from the grain boundary to the particle necks (grain boundary and volume/bulk diffusion). All others result in coarsening.

2.4.1 Sintering Stress

Differences in sintering rates between various materials can occur for a variety of reasons. This can occur due to inhomogeneous particle packing (different pore morphologies) [46-48], inclusion of non-sintering particles [49], or constraint from a substrate or secondary material [50-52]. Figure 2.13 illustrates how variations between shrinkage rates of two materials can give rise to strain (and a corresponding stress) within the system. The material that develops a tensile stress grows in jeopardy since the sintering materials are still porous and weak at this point and especially susceptible to damage. The two approaches to minimize the deleterious effects of this differential constrained sintering problem are to match the sintering rates for each material or examine if any stress relaxation mechanisms exist in either material.
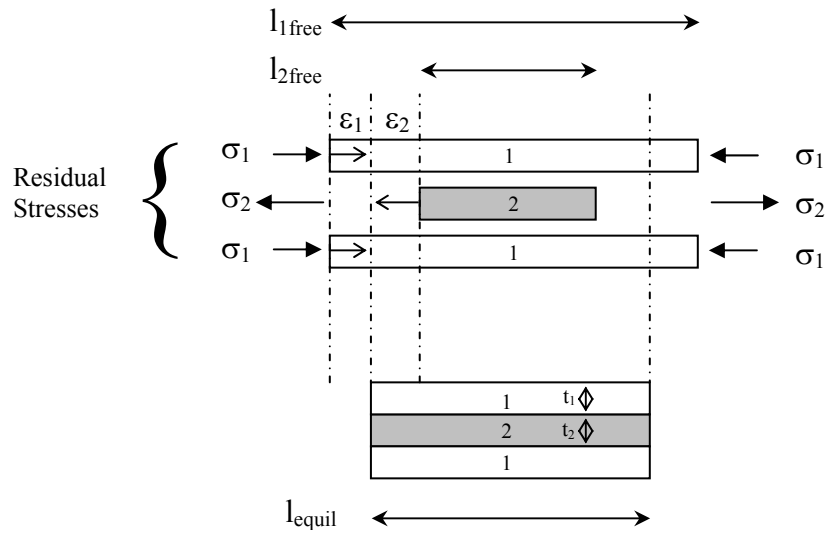
Figure 2.13 Shrinkage differences create stress in joined material layers. $l_{1,free}$ and $l_{2,free}$ are the free shrinkage values. The mutual constraints give rise to residual stresses that strain each layer (ε_1, ε_2) to the equilibrium values (l_{equil}). The material with the higher shrinkage (layer 2) develops a tensile stress while layer 1 experiences a compressive stress.

2.4.2   Constrained Sintering

The primary defect that arises from a constrained sintering condition is seen to be an increased quantity of porosity due to retardation of densification. Bordia and Raj [51] were among the first to investigate the constrained sintering problem and examined a sintering film constrained on a semi-infinite substrate. Assuming the film has the higher sintering rate, a tensile stress evolves during the early stages of sintering. The sintering pressure in the constrained system is then given by:

$$P = \frac{2\gamma_{SV}}{r} - \frac{2}{3}\sigma \qquad\qquad (2.4.6)$$

where the first term is the hydrostatic sintering pressure and σ is the tensile stress created by the constraint. As the tensile stress rises, the tendency towards densification diminishes and is eventually eliminated. If the stress continues to increase, and there exist no mechanisms to relax the stress, sintering damage results. Bordia and Raj suggested that sintering damage is manifested as a congregation of pores since their analysis concluded that tensile stresses established by constraint are not large enough to initiate and propagate cracks.

Cai *et al*. [53] reported various processing defects in a constrained alumina/zirconia laminate system. The authors point out that much of the constrained sintering damage manifests itself in the form of cracks that are blunt and cavity-like in appearance. These types of cracks have large crack opening displacements and appear to form through the linkage of low-density, highly porous regions consistent with Bordia and Raj's [51] claims. It was suggested that since these regions are the weakest in the

layer, these would be most susceptible to residual stresses during cooling and would serve as sites for nucleation of thermal expansion mismatch cracking.

Cheng and Raj [54] investigated the damage in co-sintered films of ceramic/metal/ceramic and glass/metal/glass. They report that in the case of a net tensile stress developing in the metallic layer, the stress can be relieved through plastic deformation of the metal. This manifests as a growth of voids within the metal. It was also experimentally shown that if a layer possesses a mechanism for high shear relaxation, such as viscous flow in the glass layer, tensile stresses could be alleviated and damage avoided.

2.4.3 Constrained Sintering and Reduction

If thermodynamics and processing conditions are favorable, a transition metal oxide can be reduced to its base metal. As with sintering, reduction will occur as the material is heated and can also influence the rate of shrinkage. Reduction shrinkage results from the loss of oxygen as well as changes in the crystal structure. This additional shrinkage will also contribute to the differences that cause the constrained sintering condition.

The kinetics of reduction are dependent on the diffusion of reducing gas and reduction products to and away from the interface, and interfacial reactions. Since sintering closes off networks of pores, it is important that any reduction steps be complete before the percolation limit is reached and the diffusion pathways for gas are closed. El-Geassy and Nasr [38] established a dependence of hematite reduction time on the pore structure developed by various initial sintering conditions of the compact. They demonstrated an increase of reduction activation energy with decreasing pore surface area implying that reduction grows increasingly difficult with less porosity. Nadler [41]

reported that for Fe_2O_3/Cr_2O_3 honeycombs and compacts, the quantity of Cr_2O_3 reducible is limited because the thermodynamics determine that Cr_2O_3 reduction occurs at such high temperatures where both Fe and Cr sinter readily, closing off diffusion paths for reducing gas and reduction products.

Champion *et al.* [55] studied the reduction and sintering of spherical, nanosized copper particles with a thin layer of cupric oxide on the outside. They observed a decrease in reduction temperature compared with micron sized copper particles and suggested a particle size dependence on reduction gas reactivity. With decreasing particle size, the presence of surface defects increases, mainly due to the high curvature of smaller particles. The greater defect density serves as nucleation sites for the dissociation reaction ($H_2 \rightarrow 2H^+$) that lead to reduction. The oxide layer on the outside was also found to be beneficial since its presence inhibited surface diffusion mechanisms that lead to particle fusion without densification. By the time the oxide layer was removed via reduction, the particles were at a temperature regime where diffusion processes favoring densification were in control.

2.5   Residual Stress

Residual stresses are those stresses that persist in the absence of an external force. Thermal stresses develop in joined materials because of constraints ensuing from shrinkage differences. These can arise during heating because of differences in sintering rates but it is generally assumed that at the high temperatures required for sintering, various mechanisms exist to relax any developing stresses. During cooling however,

these thermally activated stress relieving mechanisms cease and strains develop because of differences in material thermal expansion.

2.5.1   Thermal Stresses Due to Expansion Mismatch

Volumetric expansion/contraction occurs when equilibrium interatomic bond distances change. The primary cause of this is the change in atomic vibrational energy with temperature. Expansion/contraction can also arise due to phase transformations and magnetic transformations. Macroscopically, expansion is characterized by a parameter called the coefficient of thermal expansion (α), which is defined as:

$$\alpha = \left(\frac{dl}{dT}\right)\left(\frac{1}{l_o}\right) \tag{2.5.1}$$

Since thermal expansion is primarily a function of interatomic distance, it is only dependent on chemical composition and crystal structure [56]. Control of either or both of these parameters would allow for management of thermal expansion behavior.

Various literature sources have reported thermal expansion behavior of a variety of metallic interconnect candidates. These are summarized in Table 2.1 and compared with a common electrolyte, YSZ. James [57] maintains that some caution must be exercised when considering expansion values. These are average values that can change depending on how they are calculated.   Equation 2.5.1 can be calculated as an instantaneous thermal expansion value or an average expansion value depending on how the dl/dT term is evaluated.

Table 2.1 Thermal expansion values for various interconnect alloy compositions compared with YSZ electrolyte

Material	Thermal Expansion (10^{-6} / °C)	Temperature Range (°C)	Source
YSZ	10.0-12.0	100-1300	[3, 17, 29]
Doped LaCrO$_3$	9.5	-	[17]
Cr5Fe1Y$_2$O$_3$ (Plansee)	11.8	100-1000	[29]
Ferritic Stainless Steels	11.5-14.0	RT-800	[13, 15]
Austentic Stainless Steels	18.0-20.0	RT-800	[13, 15]
Ni-based Superalloys	14.0-19.0	RT-800	[13, 15]
Fe-based Superalloys	15.0-20.0	RT-800	[13, 15]

2.5.2   Residual Thermal Stress in Laminate Materials

In laminate (layered) materials, various stresses in the layer arise due to thermal expansion differences. Virkar *et al.* [58] and Chartier *et al.* [59] outline a model for stresses in laminar materials. Assuming that the only strains are from thermal expansion and that these are linearly elastic and uniform, the expected strain can be expressed as:

$$\varepsilon_x = \int_{T_{Z.S.}}^{T} \alpha_x dT \qquad (2.5.2)$$

where α_x is the respective thermal expansion coefficient for material "x", $T_{Z.S.}$ is the "zero stress temperature" at which thermal stresses begin to build, and 'T' is the final temperature. The corresponding stress relationship is:

$$\varepsilon_{11} = \frac{1}{E}\left(\sigma_{11} - \nu\sigma_{22}\right) \qquad (2.5.3)$$

Since the thermal expansion is uniform in all directions of the layer, the loading will also be symmetrical within the 1 and 2 directions for an infinite laminate, ($\sigma_{11} = \sigma_{22}$) and Equation 2.5.3 reduces to $\varepsilon_{11} = ((1-\nu)/E_{11})\sigma_{11}$. A balance of forces of a symmetrical composite ($2n + 1$ layers) such as the one in Figure 2.13 would require that:

$$\sum_{i=0}^{2n+1} \sigma_i^t t_i = 0 \tag{2.5.4}$$

This gives an expression for the residual stress in layer 1:

$$\sigma_1 = \frac{\Delta\varepsilon}{\left(\dfrac{1}{E_1'} + \dfrac{t_1}{t_2 E_2'}\right)} \tag{2.5.5}$$

where $E'_x = E_x/(1-\nu_x)$ (E is Young's modulus and ν is Poisson's ratio), $\Delta\varepsilon$ is the difference in thermal expansion of the layers and t_x is the thickness of layer 'x'. The stress that arises in the other layer is related to this value as:

$$\sigma_2 = -\sigma_1 \frac{t_1}{t_2} = -\frac{\Delta\varepsilon}{\left(\dfrac{t_2}{t_1 E_1'} + \dfrac{1}{E_2'}\right)} \tag{2.5.6}$$

where the variables are the same as listed before. It is seen that due to self-equilibrium, the stress within the layers are equal and opposite in sign. For the layer in a tensile state, this stress can cause any preexisting flaws to propagate or extend.

2.5.3   Residual Stress Distribution

The key assumption in deriving the stress values in the prior section was that the stress within the layers is uniform. This is true for a case where the layers are unbonded and constrained at the ends, however for the system of interest, the interface is bonded and a strain distribution across the layer is thus expected.

Bao *et al*. [60] model this distribution in tri-layer laminate composites. Their analysis examines the geometry outlined in Figure 2.14. Residual stress within the layers results from interfacial shear stresses, which develop due to thermal expansion differences. These stresses are quantified as:

$$\tau = \tau_o \xi^n, (0 \leq \xi \leq 1, \xi = x/L) \tag{2.5.7}$$

where τ_o and n are material constants and ξ is the relative length from the middle of the layer ($\xi = 0$) to the end of the layer ($\xi = 1$) and L is one half of the sample length. The
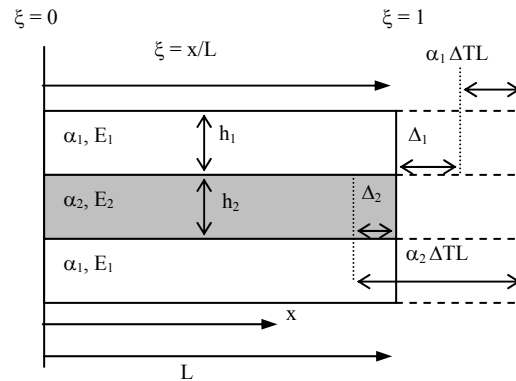
Figure 2.14 Geometry of a trilayer laminate used for residual stress distribution analysis [60]. The length of the laminate is 2L, the width is B, and α_x, E_x, v_x, and h_x are the CTE, elastic modulus, Poisson's ratio and thickness of layer "x".

shear stresses are thus expected to be greatest at the ends of the layer and minimal in the middle. The resultant residual stress as a function of location was then found through stress equilibrium:

$$\sigma_1(\xi) = -\frac{\tau_o L}{(n+1)h_1}(1-\xi^{n+1})$$ (2.5.8)

which indicates that the residual stress should be greatest at the middle and taper off towards the end of the bar. (Figure 2.15) Equation 2.5.8 also indicates that all other considerations being equal, layers of greater length will be subject to larger residual stresses. The shear stress in a layer also results in a bending moment, which is also a function of location:

$$M_1(\xi) = \frac{BLh_1\tau_o}{2(n+1)}(1-\xi^{n+1})$$ (2.5.9)

Since there is no curvature or deflection of the laminate, the moment in any section is zero. For this to occur, an interfacial normal stress must exist to counteract the bending moment. Based on the mechanics of materials, the normal force would have a distribution such as:

$$q(x) = Cx^{n-1}, (0 \leq x \leq L)$$ (2.5.10)

where C is a constant and the normal stress distribution would have the form:

$$\sigma_{\text{interface}} = D(x^{n-1} - x_o^{n-1}) \qquad\qquad (2.5.11)$$

where D is a constant and x_o is the point along the layer where the normal stress distribution changes from tensile to compressive. (Figure 2.15C)

$$x_o = \left(\frac{1}{n}\right)^{\frac{1}{n-1}} L \qquad\qquad (2.5.12)$$

The residual stress would thus be expected to vary not only along the length of the layer, but also along the thickness of the layer.

Equations 2.5.10-2.5.12 indicate that normal stresses towards the outside edges of the laminates not only differ in magnitude from the bulk stresses but also are of the opposite sign. Sergo *et al.* [61] examined edge stresses in alumina/zirconia laminates using fluorescence piezospectroscopy and compared their results to an analytical force-superposition model. Assuming a homogeneously infinite body, the stress field at a point (x,z) resulting from a load/stress applied over a thickness "t" can be given by:

$$\sigma_{ii} = \frac{\sigma_{bulk}}{\pi} 2(1+\nu) \left[\sin^{-1}\left(\frac{x}{\sqrt{x^2+z^2}}\right) - \tan^{-1}\left(\frac{x-t}{z}\right) \right] \qquad (2.5.13)$$

where σ_{bulk} is the bulk biaxial stress in the laminate and ν is Poisson's ratio. Figure 2.16 is the results of the three-dimensional normal stress distribution model based on their experimental data. It is seen that at the edges of the laminate structure that the sign of the stresses changes from the bulk to the edge of the laminates. The implication of this is that the layer under compression according to Figure 2.13 is under tension at the edge.

Although the layer is under compression in the direction parallel to the layers, in the perpendicular direction, the layer is under tension and a crack can propagate parallel to the layer due to this tensile stress. Munz and Yang [62] modeled edge stresses in ceramic/metal joints for several ceramic/metal systems. They emphasize that differences in the thermal expansion and effective Young's modulus will alter the state of the edge stresses in the layers. These are summarized in Table 2.2

Table 2.2 Sign of the edge stress in the ceramic layer of a ceramic/metal laminate system after cooling [62]. α is the coefficient of thermal expansion and E^* is the effective modulus ($E/(\nu[1+\nu])$).

Thermal Expansion	Effective Modulus Comparison	Resultant Stresses
$\alpha_{ceramic} > \alpha_{metal}$	$E^*_{ceramic} > E^*_{metal}$	Compressive
$\alpha_{ceramic} > \alpha_{metal}$	$E^*_{ceramic} < E^*_{metal}$	Tensile (changes to compressive along the free edge)
$\alpha_{ceramic} < \alpha_{metal}$	$E^*_{ceramic} > E^*_{metal}$	Tensile
$\alpha_{ceramic} < \alpha_{metal}$	$E^*_{ceramic} < E^*_{metal}$	Compressive (changes to tensile along the free edge)

a.)

b.

c.)

σ_m

0

L

x_0
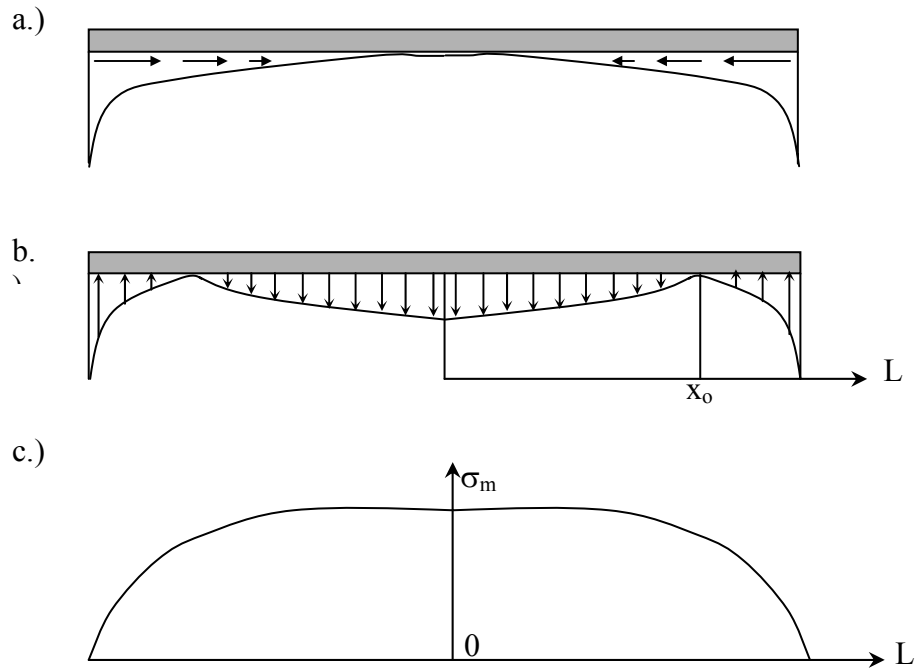
Figure 2.15 Schematic of a.) interfacial shear stress giving rise to residual stresses in the laminate, b.) normal stress at the interface and c.) residual stress distribution in a single layer of a multi-ply laminate, after [60].

A   AZ   A

Stress (MPa)

Distance along Surface (μm)

Distance into Laminate (μm)
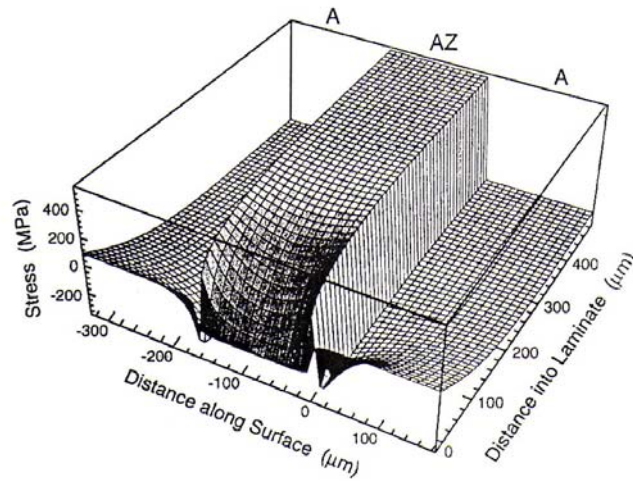
Figure 2.16 Three dimensional mean normal stress distribution near the free edge region of an alumina/(alumina/zirconia)/alumina laminate calculated from measured residual stress values [61].

2.5.4   Minimizing Residual Stress

The choice of fuel cell electrolyte (along with its corresponding properties) is often fixed, so minimizing residual thermal stresses is best tackled through altering the properties of the interconnect. This can be approached by altering the thermal expansion behavior of the alloy or by manipulating other mechanical properties. Equation 2.5.3 shows that for a given system, the residual stress is proportional to the thickness of the laminae and their mechanical properties. Thus, changing the elastic modulus will also alter the residual stress. Church [14] has recently investigated thermal expansion and oxidation properties of a large number of interconnect alloy candidates in the Fe-Ni-Cr system. It was shown that slight changes in composition (as little as 2-5 wt%) could produce significant differences in thermal expansion curves. It was concluded that binary alloys around the Fe50Ni and Fe20Cr compositions provided the best expansion matches with YSZ. It should be noted that the expansion mismatch values in these figures are calculated from room temperature. Eisele [63] and Church both discuss the notion of a "zero stress temperature" below which stresses begin to build. Depending on the value of this temperature, the appearance of expansion curve mismatch can change considerably. Eisele modeled the stresses and strains found in a co-extruded electrolyte/alloy interconnect stack over the course of processing. The variables that influence stress relaxation include temperature, hold time, material density and cooling rate. At sufficient temperatures, bulk viscous flow of the ceramic electrolyte is sufficient to relieve stresses. It was suggested from high temperature mechanical tests that a Fe-Ni-Cr interconnect could serve to relax stresses through creep mechanisms at temperatures as low as 600°C. Hehn *et al*. [64] tried reducing residual stresses in a laminated alumina/nickel system by

annealing to temperatures of 700, 900 and 1000°C. They observed no effect of annealing on the measured stress state. However, considering Eisele's analysis, it is likely that the hold time was too low (one hour), and the cooling rates (5°C/min to 450°C, furnace cooling to RT) and density (laminates were formed from pre-made metal and ceramic) were too high to effectively reduce stresses.

Another approach to relax stresses is through plastic deformation of the metal. Shieu and Sass [65] examined dislocation mechanisms for the relaxation of mismatch stresses in a metal/ceramic (Pt/NiO) interface. The climb and glide of dislocations to or away from the interface alters the spacing of misfit dislocations and allows for accommodation of thermal stresses. Dislocation flow in the metal is dependent on which material has larger thermal expansion. If the thermal stress is larger than the metal's yield stress, a large number of dislocations can be generated and the metal can plastically deform to reduce stress.

Density becomes a factor in residual stress formation because of the dependence of mechanical properties on porosity. As a general rule, materials properties diminish with increasing porosity. Porosity is a processing parameter that can easily be controlled during sintering or through the introduction of additional impurities. Ramakrishnan and Arunachalam [66] developed an expression for the effective elastic moduli of porous materials using a statistical continuum mechanics approach. The effective Young's modulus is given by:

$$E^{*} = E(1-\rho)^{2} /(1+b_{\rho}\rho)$$

(2.5.14)

where E is the modulus of the dense material, ρ is the fraction of porosity, and b_ρ is a function of the dense Poisson's ratio and equals $2-3\nu$. Other researchers have also proposed expressions for the correlation between elastic moduli and porosity. Bocchini [67] studied the influence of porosity on a number of properties for sintering materials. His expression for the effect of porosity on modulus is:

$$E^* = E(1-\rho)^{3.4}$$
(2.5.15)

Boccaccini [68] also recognized the potential for porosity to control residual thermal stresses and related porosity to elastic moduli as:

$$E^* = E(1-\rho^{2/3})^S$$
(2.5.16)

In both of these expressions, ρ is the fraction of porosity and E is the dense elastic modulus. Boccaccini's analysis tried not only to incorporate the total amount of porosity, but the shape and morphology of it as well. 'S' is an expression accounting for shape and orientation of the pores, assuming an elementary cell with a single spheroidal pore cavity. The effect of both porosity and layer thickness (volume fraction) on residual stress (strain) is illustrated in Figure 2.17 and Figure 2.18 for an alumina/zirconia composite laminate.
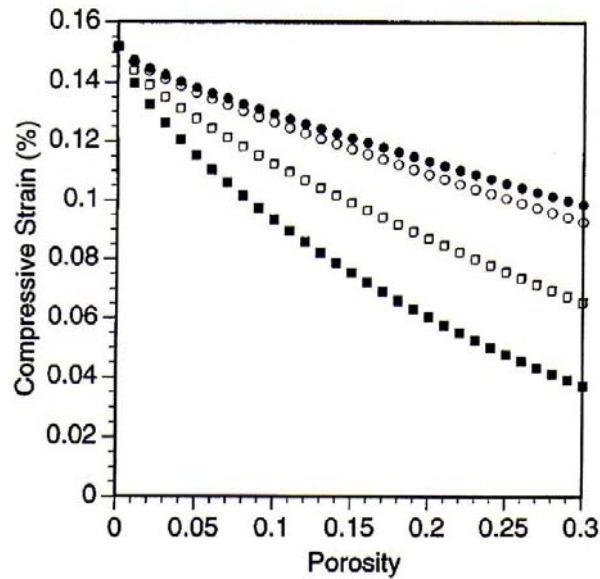
Figure 2.17 Residual strain present in the alumina layers of an alumina/zirconia composite laminate as a function of porosity. ΔT = 1430°C and the relevant data applied in the model is provided in Boccaccini [68]. (●) – spherical porosity, randomly oriented, (□) – spheroidal porosity, (z/x = 10), (○) – spheroidal porosity, (z/x = 0.5), (■) – spheroidal porosity, (z/x = 0.1).
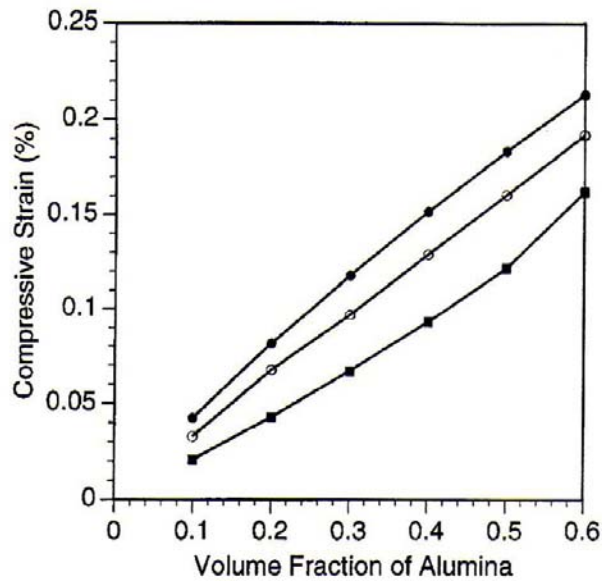
Figure 2.18 Residual strain present in the alumina layers of an alumina/zirconia composite laminate as a function of the volume fraction of alumina and pore shape. ΔT = 1430°C and the relevant data applied in the model is provided in Boccaccini [68]. (●) – pore free layers, (○) – 10% spherical porosity, (■) – 10% oblate porosity, (z/x = 0.1).

2.5.5 Residual Stress Characterization

A variety of techniques exist to characterize residual stresses. Chiu [69] discusses the use of curvature measurements to determine the residual stress from thin films placed on strips. Kese and Rowcliffe [70] and Atar *et al.* [71] utilize indentation techniques to obtain residual stress values in ceramic materials by comparing indentation parameters in stressed and unstressed regions. Both of these methods however are destructive. Plus, the former can only handle certain specimen geometries and the latter cannot examine residual stresses in metals effectively. X-ray diffraction (XRD) is an attractive, non-destructive technique that has been used considerably to measure residual stresses in both metals and ceramic laminate layers.

Recently, Adachi *et al.* [72] used XRD to measure residual stresses in co-sintered laminates of alumina and yttria stabilized zirconia. A third powder, SiC was blended with the zirconia to form a mixture with a better CTE match with the alumina. They demonstrated a resultant modification of the residual stress values. Hehn *et al.* [64] measured residual stresses in tape cast, laminated alumina/Ni composites with XRD. Comparisons with stress values obtained from indentation measurements validated their results. Pintschovius *et al.* [73] combined neutron and x-ray diffraction to observe residual stress distributions in brazed metal/ceramic systems. Their results were found to correlate well with finite element calculations. They also found experimental evidence of plastic deformation of the metal layers.

For crystalline materials, diffraction of waves with a particular wavelength λ is only possible when the crystal planes are oriented in a manner that fulfills the Bragg condition [74]:

$$n\lambda = 2d \sin \theta \qquad (2.5.17)$$

where θ is the diffraction angle and 'd' is the crystal lattice spacing that fulfills the diffraction conditions. The intensity, number and location of peaks are material dependent, so an intensity versus 2θ spectrum provides a "fingerprint" of the material along with a wealth of additional information.

Noyan and Cohen [75] provide an excellent overview of using XRD for residual stress applications. X-ray diffraction does not measure stress and strain directly, but the induced change in crystallographic lattice spacing. When a material is elastically strained, the distance between crystallographic planes (d) will either expand or contract. The Bragg equation dictates that the diffraction angle θ will change proportionally and the peak will shift. It should be noted that the change in lattice spacing is a function of orientation; in the extreme case, those planes that are oriented perpendicular to the direction of an applied stress will experience the greatest amount of strain, while those planes parallel to the stress will remain unaltered. Thus, multiple measurements at various orientations must be made to obtain the true stress values (Figure 2.19).

Generally speaking, strains and stresses are rarely uniaxial, so analysis is performed considering biaxial or triaxial conditions. For a sample under a biaxial stress state, the strain measured from XRD is given by:

$$(d_{\phi\psi} - d_o) \big/ d_o = (1+\nu) \big/ E \{\sigma_\phi \sin^2 \psi - \nu \big/ E (\sigma_{11} + \sigma_{22})\} \qquad (2.5.18)$$

where E and ν are the Young's modulus and Poisson's ratio of the material, $d_{\phi\psi}$ is the strained lattice spacing, d_o is the unstrained lattice spacing, σ_{11} and σ_{22} are the principal stresses, σ_ϕ is the applied/residual stress comprised of the principal stress tensors and ϕ and ψ are angles that relate the orientation of the sample (S) with that of the diffractometer (L) coordinate systems (Figure 2.20). The expressions (-ν/E) and (1+ν)/E are also known as x-ray elastic constants and are replaced by the terms s_1 and $\frac{1}{2}s_2$ respectively. The residual stress can be found through extrapolating a number of $d_{\phi\psi}$ measurements made at multiple values of $\sin^2\psi$.
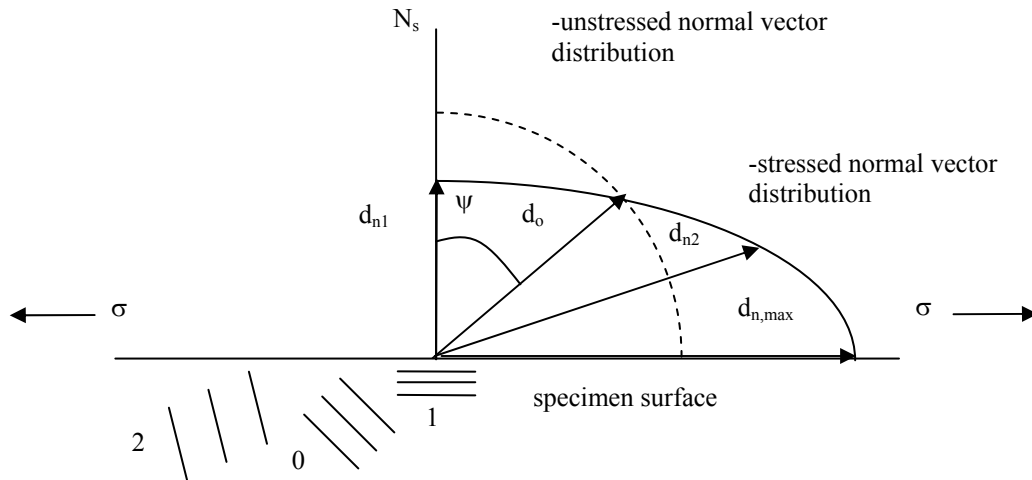
Figure 2.19 Illustration of the effects of applied stress on crystallographic lattice spacing (d) of a hypothetical crystalline material. The lattice spacing has a monodisperse distribution of lattice spacings in an unstressed state (d_o). When stressed, the interplanar distances increase as the normal vectors of the planes align with the direction of applied stress and decrease as the vectors align with the surface normal ($d_{n,max} > d_{n2} > d_o > d_{n1}$) after, [74].
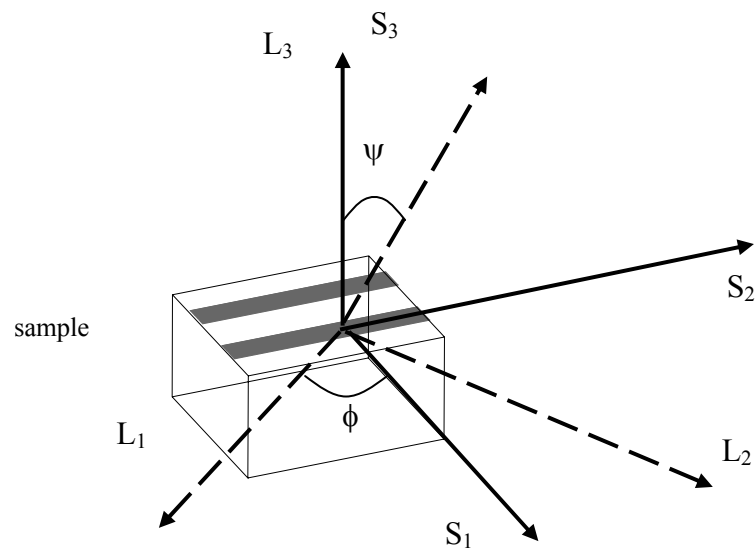
Figure 2.20 Schematic drawing of the fuel cell platform sample (S) and laboratory (L) coordinate systems. The gray bands represent the YSZ layers, where the stress was analyzed.

3 Experimental

This work examines issues surrounding an extruded multi-layer fuel cell platform. Three aspects related to the processing were considered: 1.) Particle and paste characterization were performed to optimize paste extrusion. 2.) Sintering studies were conducted to establish their behavior in a co-sintering situation. 3.) Residual stresses were measured and modeled to provide insight into how to avoid residual stresses in the platform.

Systems based on a Fe-Ni/YSZ interconnect/electrolyte combination were chosen for fuel cell platform production and subsequent studies on sintering defects and residual stress characterization. Fuel cell platforms of Fe45Ni/YSZ, Fe47.5Ni/YSZ, and Fe50Ni/YSZ were processed and studied. Prior studies [14] have indicated that these combinations result in minimal thermal expansion mismatch and are thus good candidates for residual stress studies.

This study examined the properties of the starting powders to manipulate not only the properties of the paste but the sintering conditions as well. Paste rheology was characterized by capillary rheometry. Sintering curves were characterized using a non-contact and pushrod dilatometer. Sintering damage (porosity) in sintered hybrid samples was characterized by microscopy (to determine porosity distribution) and Archimedes method (to obtain the total porosity). X-ray diffraction was used to measure the residual stresses in the fired platforms and measurements were compared to values predicted by finite element calculations. Various parameters for the model were collected experimentally and from the literature.

3.1   Powder Characterization

The primary powders examined in this study are outlined in Table 3.1. Micrographs of the individual powders were taken in a Hitachi S800 scanning electron microscope at excitation voltages of 5-10 kV to minimize charging of the oxides. Studies to match the overall shrinkage of the ceramic and metallic components of the platform were performed. The precursor powders for the interconnect were blended with additional powders to manipulate shrinkage. Various ratios of nickel oxide/nickel metal were mixed to modify shrinkage related to reduction. Iron metal powder was not used because of its propensity towards oxidation. Instead, various amounts of fine (0.1-0.3μm) hematite powder (Ceramic Color and Chemical Co., New Brighton, PA) were added to manipulate shrinkage through improved particle packing. The various powder blends were extruded and dried and measured using a micrometer before and after reduction to calculate the dimensional changes.

Table 3.1 Powders used for the fabrication of the Fe-Ni/YSZ solid oxide fuel cell platform.

Powder	Source	Notes
8 mol% YSZ	Daiichi Kigenso Co., dist. by Zirconia Sales (America) Marietta, GA	0.3 μm average particle size
Fe_3O_4	Pea Ridge Iron Ore, Sullivan, MO	1.8 μm average particle size
NiO	Ceramic Color and Chemical Co., New Brighton, PA	
Ni metal	Atlantic Equipment Engineers, Bergenfield, NJ	4-8 μm particle size

3.2   Paste Formulation

For co-extrusion, separate pastes for the electrolyte and interconnect were formulated according to a batch spreadsheet as outlined by Hurysz [31]. Iron and nickel based powders for the interconnect are mixed in such ratios that they form the final desired metallic ratio. The batch spreadsheet incorporated parameters of each powder and processing aid (Table 3.2) and calculated the necessary proportions for each paste component. A typical green composition is given in Table 3.3. Each paste consisted of the material powder(s) and a liquid phase consisting of a common methylcellulose binder (Methocel A4M), water and a lubricant.

The electrolyte consisted of an 8 mol% Y_2O_3 stabilized ZrO_2 powder (Daiichi Kigenso Co). Deagglomeration of the powder was achieved by ball milling in acetone along with a blown Menhaden fish oil dispersant (Tape Casting Warehouse) for a period of 24 hours. The methocellulose binder was then added along with butyl stearate

Table 3.2 Processing aids for the pastes.

Processing Aids	Source	Notes
Methylcellulose	Dow Chemical Co., Midland, MI	binder
Butyl Stearate	Fisher Scientific	lubricant
Blown Menhaden Fish Oil	Tape Casting Warehouse, Morrisville, PA	dispersant
Pegosperse 100S	Lonza, Fair Lawn, NJ	lubricant

(lubricant) and milled for an additional hour. The powder was dried and dry ball milled, and the remainder of the liquid phase (water) was added to granulate the powder. The granulated powder was mixed in a reciprocating single screw kneader (Buss). The

kneader subjected the mixture to a high shear compounding step to obtain a final, homogeneous paste.

The interconnect precursor paste followed a similar procedure. The paste was comprised of a blend of powers-magnetite (Pea Ridge Iron Ore) and nickel oxide (Ceramic Color and Chemical) or nickel metal (Atlantic Equipment Engineers). Powders were weighed out to correspond to the final metallic ratios, ball milled in acetone and Menhaden fish oil for 24 hours and dried. The powders were then dry mixed with the binder in a commercial food processor for several minutes, granulated with an aqueous solution of a polyethylene glycol ester (Pegosperse 100S-Lonza) lubricant and compounded.

Table 3.3 Typical batch composition that after reduction would yield a Fe45Ni alloy with a solids loading of ~48.5 volume percent. The water to binder weight ratio is constant at 3:1 and the binder to lubricant ratio is set at 15:1.

Component	Quantity (grams)	Solids Volume Fraction
Fe_3O_4 powder	314.06	35.97%
Ni metal powder	185.94	12.38%
Water	69.00	40.94%
Methylcellulose Binder	23.00	9.89%
Pegosperse Lubricant	1.53	0.83%

3.3 Extrusion and Firing

The individual pastes were fed into alternating barrels of the co-extruder and extruded to form a 4x4 square cell structure consisting of alternating layers of interconnect (three layers total) and electrolyte (two layers total). A schematic of the barrel and die used in the co-extrusion is shown in Figure 3.1. A variable load cell (SATEC IUD500 Universal testing machine) was used to drive the ram extruder at a constant velocity. The extrusions were cut and dried overnight enveloped in a low-density, open cell foam

sponge to ensure even drying. The green samples were fired in a vacuum furnace purged
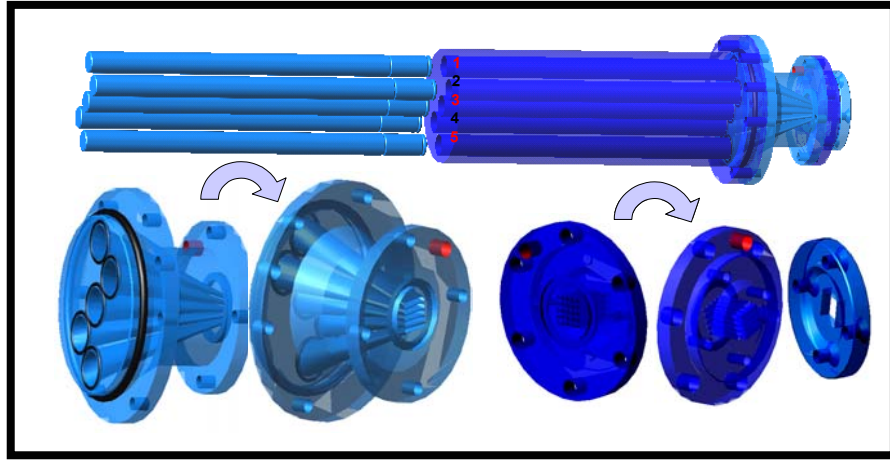
Figure 3.1 Schematic of the ram extruder and die used for hybrid SOFC co-extrusion. Pastes are fed into alternating channels in the barrel and meet in the die land to form the alternating layers.

and backfilled three times with the reducing gas. The firing temperature profile is given

in Table 3.4. The individual components (both alloys and individual powders) of the

hybrid co-extrusion were also extruded for dilatometry tests and fired according to the

same schedule.

Table 3.4 Temperature profile(s) for firing of hybrid co-extrusions in vacuum furnace. *Certain runs were brought from 1000°C to room temperature at 2°C/min.

Furnace Profile Stage	Temperature	Ramp Rate	Hold Time
1	RT - 1250°C	2°C/min	6-8 hours
2	1250 - 1000°C	1°C/min	0
3	1000 – 750°C*	2°C/min	0
4	750°C - 600°C	1°C/min	30-60 minutes
5	600-RT	1°C/min	0

3.4   Rheological Characterization

Paste properties were characterized by capillary rheometry. An illustration of the rheometer is given in Figure 3.3. The barrel housing, ram and dies are custom stainless steel. The ram is fitted with grooves to house an o-ring, preventing paste from seeping back up the barrel. The rheometer was driven by a SATEC universal testing machine with a 2,000 lb load cell. Pastes were loaded in a one-inch diameter barrel and extruded through dies of varying die land length/diameter ratios (L/D). These ratios were 12:1, 8:1, 4:1 and 1:1 with a constant die diameter of 1/8". For each die, extrusion speeds were varied (54.80, 21.92, 10.96 and 2.19 mm/s) and the maximum loading force was recorded as a function of velocity and die geometry.

These values were converted to extrusion pressure and plotted against L/D ratio. A sample plot is given in Figure 3.2:

Extrusion Pressure vs. L/D

$y = 0.4039x + 4.0422$
$R^2 = 0.9984$

$y = 0.2719x + 3.4876$
$R^2 = 0.9718$

$y = 0.2537x + 3.1798$
$R^2 = 0.9826$

$y = 0.209x + 2.9818$
$R^2 = 0.9805$
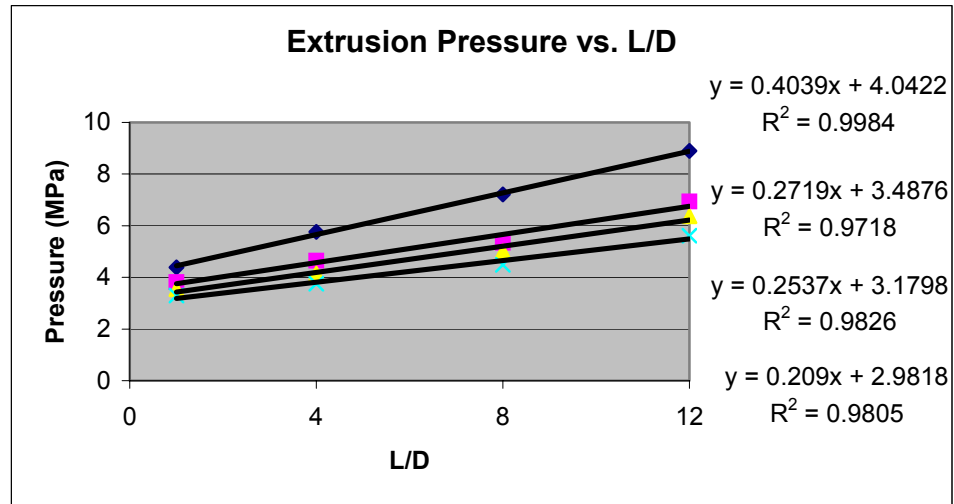
Figure 3.2 Capillary rheometry plot used for the extrapolation of paste characterization parameters: α, β, σ_o, and τ_o.
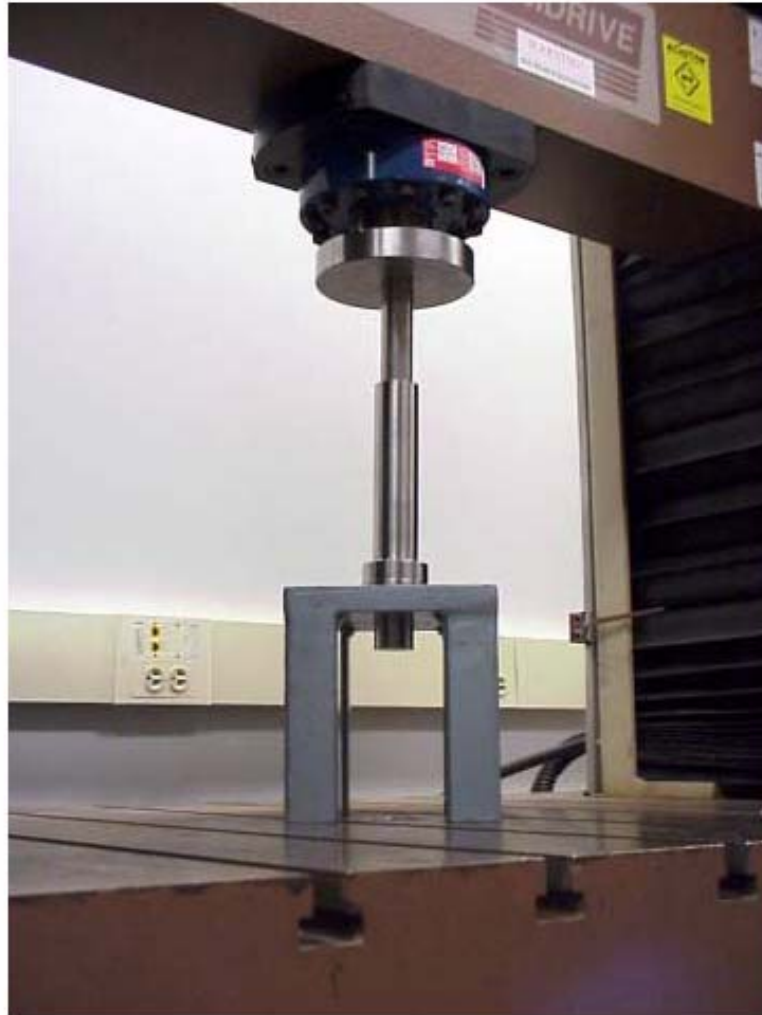
Figure 3.3 Photograph of capillary rheometer. [31]

The yield shear stress and wall shear stress values can then be derived from the four parameter Benbow and Bridgwater equation (Equation 2.3.1) The slopes of each curve are then equal to:

$$m = 4(\tau_o + \beta V_x)$$

(3.5.1)

and the intercepts are equal to:

$$b = 2(\sigma_o + \alpha V_x)\ln\left(D_o\!\!\Big/\!_D\right)$$

(3.5.2)

where V_x corresponds to the various extrusion velocities. D_o/D is constant, and with multiple extrusion velocities known, the four rheological parameters (σ_o, τ_o, α, and β) can be obtained algebraically.

3.5   Dilatometry

3.5.1   Sintering Curves

Sintering studies were conducted using both a pushrod dilatometer as well as a non-contact dilatometer (NCD). The layout of the non-contact dilatometer is illustrated in Figure 3.4. Samples are placed inside a susceptor cylinder housed in a custom quartz tube. Gas lines and thermocouples are inserted through the quartz end caps. Gases can be mixed through a variable flowmeter and the final gas flow is managed by a mass flow controller. The susceptor tube is inductively heated by a solid state power source

(NovaStar2 IP, Ameritherm Inc.) and monitored by a programmable controller. (Honeywell DCP 200)

To measure dimensional changes within the sample, an optical micrometer (Keyence, LS-7500 Series) is placed around the transparent end caps, capturing the dimensions of the shadow cast by the specimen. The micrometer has an accuracy of ± 0.15μm. The primary advantage of this set up is that the sample is not subject to additional forces from a pushrod, and a non-stressed, free sintering curve can be obtained.
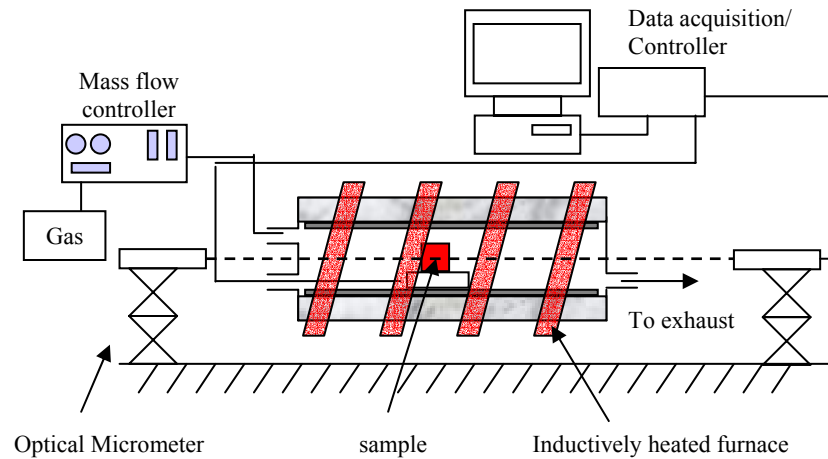
Figure 3.4 Schematic of non-contact dilatometer.

Green samples of 4x4 square cell honeycomb were cut and ground into 1x4 wedges. The wedge geometry ensured that any specimen tilt would not result in the trailing edge of the sample casting a shadow and cloaking measurements. Samples were held in place with a small amount of vacuum grease on an alumina plate and inserted into the dilatometer. The samples were purged under an 18% H_2/Ar atmosphere flowing at a

Profile Stage	Temperature	Ramp Rate	Hold Time
1	RT - 280°C	4°C/min	0 min
2	280 - 350°C	2°C/min	0 min
3	350 - 1250°C	4°C/min	30 min
4	1250 - RT	Furnace cool	0 min
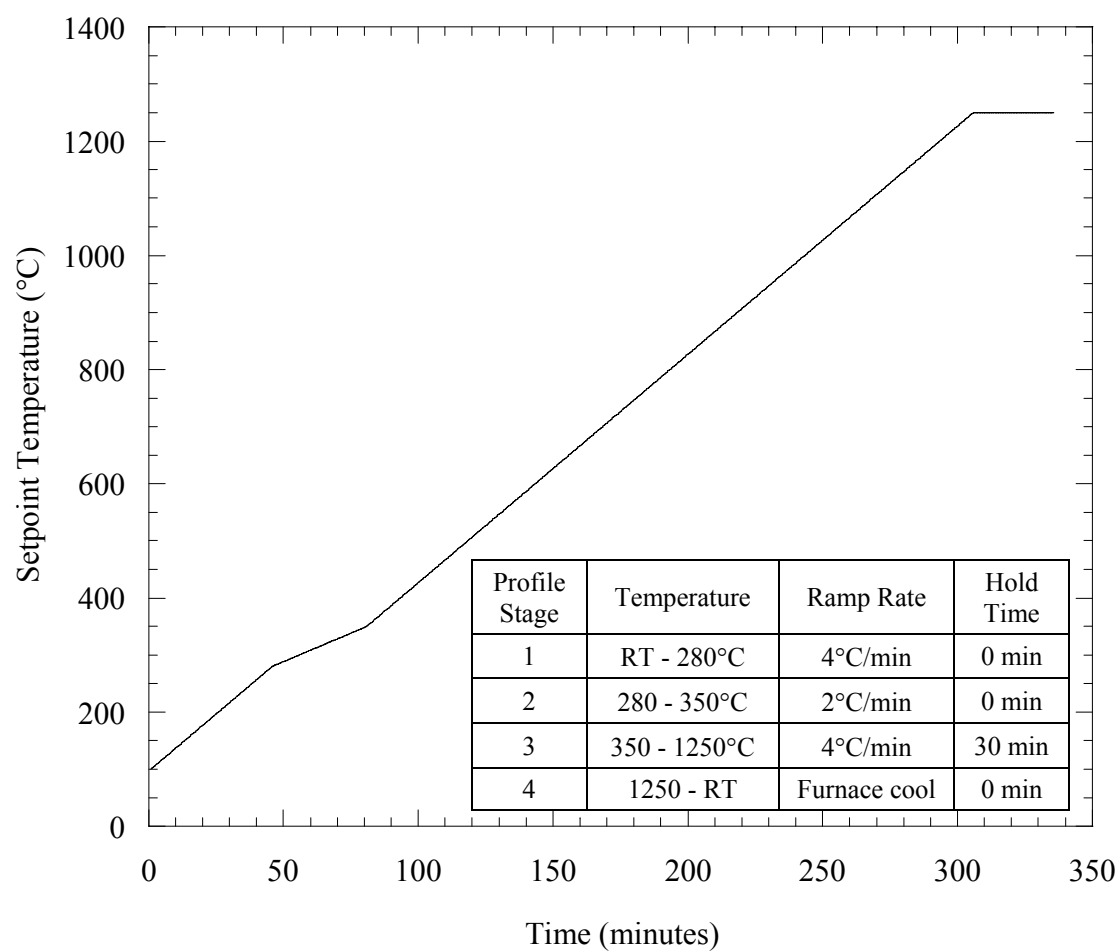
Figure 3.5 Temperature profile used for dilatometer sintering curves.

rate of 380 cc/min for thirty minutes. The samples were then fired under this atmosphere according to the profile outlined in Figure 3.5. The slow ramp rate through the 280-350°C is necessary to minimize obscuring of the micrometer's measurements due to binder burnout.

Sintering studies were also examined using a pushrod dilatometer for the sake of comparison. (Figure 3.6) Samples were cut and ground to the appropriate dimensions and measured against an alumina standard. Two thermocouples were used-one adjacent to the sample and standard to record the specimen temperature and another outside the encapsulating tube for furnace control The furnace atmosphere was purged and backfilled with argon gas three times and then adjusted to the same atmospheric conditions used in the NCD. The same NCD heating schedule outlined in Figure 3.5 was also followed.
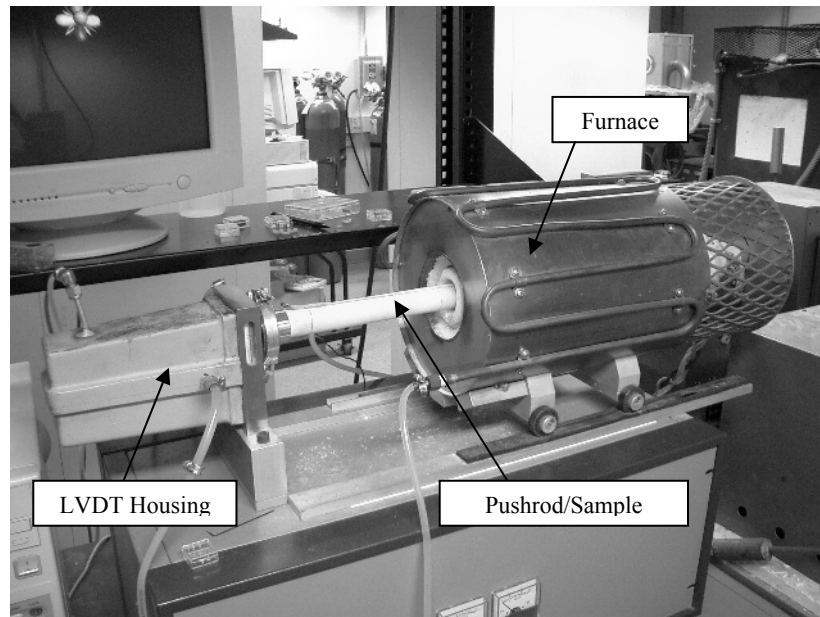
Figure 3.6 Photograph of dual pushrod dilatometer used for thermal property measurements.

The primary issue concerning the NCD is interference and noise that arise in the sintering curves. The sources of these included outside vibrations, clouding of the micrometer due to binder burnout and electromagnetic radiation from the induction coils surrounding the sample housing. All of these factors contributed to curves that required smoothing.

Unlike the NCD however, pushrods exert a finite amount of force. To minimize the effects of pushrod force, the rods were adjusted so that they would in essence be near the end of their stroke, and exert minimal pressure on specimens. Green samples were cut and ground from extruded strip to such a length where the pushrod travel would still be adequate enough to measure the expected shrinkage of ~20-40%. The sample lengths varied between ~0.40-0.65 mm with a corresponding pushrod travel of ~0.25-0.40 mm.
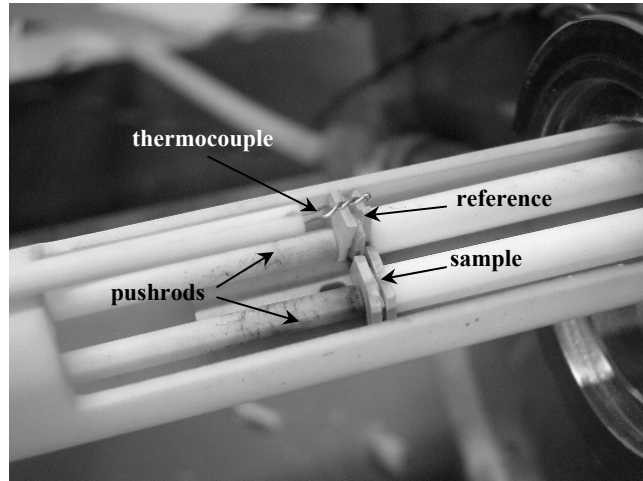
Figure 3.7 Exposed sample housing showing the dual pushrods, reference, and sample.

3.6   Constrained Sintering Characterization

3.6.1   Microscopy

Porosity distribution within the microstructure of an extruded, co-sintered hybrid structure was characterized by optical microscopy. Hybrid honeycombs fired according to the profile outlined in Section 3.2 were mounted in a transparent epoxy (Epofix, Struers). Conventional ratios of resin and hardener were mixed and poured over the samples, which were then placed in a vacuum desiccator for twenty minutes to impregnate cell channels and pores. Samples were then allowed to finish curing overnight in a 60°C oven. Mounted samples were prepared for microscopy using standard metallurgical techniques-grinding and sanding with various grades of SiC paper and polishing with a 0.1μm alumina suspension. Micrographs were obtained using a Leica PM IRM inverted optical microscope with a digital camera to capture images. Micrographs were converted to the grayscale and pore distribution was quantified by utilizing the microscope software to adjust the contrast threshold to differentiate pores from the matrix. The software calculated porosity as an area fraction of the microstructure. Individual micrographs were overlapped to form a macroscopic montage.

3.7   Interconnect Phase/Microstructure Evolution

To compliment the sintering curve data, analysis of a number of the as-reduced samples was conducted using SEM and x-ray diffraction. Secondary electron images of the surface were taken from a Hitachi S-800 field emission scanning electron microscope at magnifications of 2500x and 5000x. Bulk x-ray diffraction measurements were

conducted using a Phillips 1800PW powder diffractometer using CuK$_\alpha$ radiation. Measurements were scanned over a 2θ range of 25-150° at a step size of 0.02° with a dwell time of 1.25 seconds over each step. Peak positions were established from a least squares Gaussian fit using the XRD software and analyzed against various powder diffraction files. Additionally, sample weights was were measured both before and after firing to various temperatures to determine the associated weight loss at each temperature.

3.8 X-Ray Diffraction Residual Stress Measurements

Residual stresses were measured in a Philips MRD X-Ray diffractometer using a CuKα point source. (Figure 3.8) In order to minimize alignment errors the measurements were performed using parallel beam diffraction geometry [76]. The incident beam optics included a variable mask and divergence slit allowing for a variety of beam sizes. Diffracting beam optics included a parallel plate collimator (0.27"), a 0.04 radian Soller slit and a graphite monochromator to reduce fluorescence associated with iron-based samples. Reduced and fired samples were mounted in the diffractometer so with a sample orientation such that the extrusion direction aligned parallel with the y-axis. Sample dimensions were ~1 cm x 1 cm cross section and ~1.5 cm in length. Measurements were also taken on longer samples (~4.0 cm) to ascertain the stress distribution across the sample. The machine was calibrated to account for any offsets in the 2θ measurements and were also aligned in the z-direction to establish the location of the sample surface to minimize beam spread during stress measurements. A microscope attachment was used to orient samples to ensure proper placement of the beam. The

beam size was varied using the mask and divergence slits. Beams with widths of 0.3-0.5 mm and lengths 3-5 mm were found to be a good compromise between sufficient peak intensity and shorter measurement times. Beam location was verified using fluorescent paper, which revealed the x-ray beam.
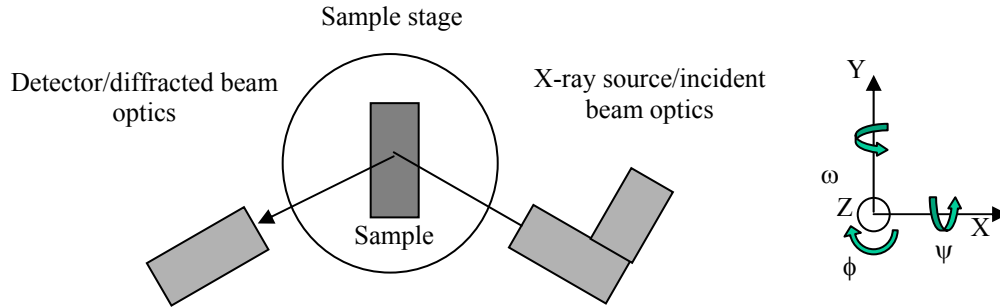
Figure 3.8 Schematic of x-ray diffractometer setup for residual stress measurements. The adjacent axis establishes the orientation of the diffractometer and the associated angles of rotation.

Stress free lattice parameters were interpolated from plots of d-spacing versus $\sin^2\psi$. Stress measurements were conducted in both layers of the fuel cell platform in directions perpendicular ($\Phi = 0°$, ψ, varied within a range of -30 and 30°) and parallel ($\Phi = 90°$, ψ, varied within a range of -30 and 30°) with the layers to evaluate the biaxial stress state. For the YSZ, the (620) peak ($2\theta \sim 143°$) was tracked and for the metal, the (420) peak ($2\theta \sim 147.6°$) was followed. Higher index peaks are preferred for stress measurements as the K_α and K_β peaks being to separate out and grow into distinct peaks. The residual stress analyses of the fuel cell platforms were evaluated assuming a biaxial stress state [75]. Stress values were calculated using the aforementioned $\sin^2\psi$ method.

3.9 Residual Stress Modeling

3.9.1 Zero Stress Temperature

In order to fully model the residual stress, it is not enough to simply know the thermal expansion curves. The zero stress temperature must also be known. The "zero stress temperature" is defined as the temperature at which any mechanisms to relax stresses in a system of layered materials cease to exist. For a metallic/ceramic-layered system, it is expected that phenomena such as plastic deformation, creep, and recrystallization of the metal phase would contribute to relaxing stresses. Similar phenomena are also expected to occur within the ceramic layer, however these would take place at much higher temperatures. A temperature range of 400-750°C would thus be a good estimate for the zero stress temperature as this is the range in which these phenomena occur.

Using a simple analytical model for thermal strains and stresses in a laminate system, a plot of room temperature residual stress as a function of possible zero stress temperature was generated using experimental dilatometry data. Assuming a particular zero stress temperature, the expansion curves of the two materials are arranged to coincide at that temperature (Figure 3.9). The difference between the two curves is the thermal strain resulting from thermal expansion mismatch. Thermal strain can then be calculated as a function of temperature during cooling. The corresponding stress is found from: [58, 59]
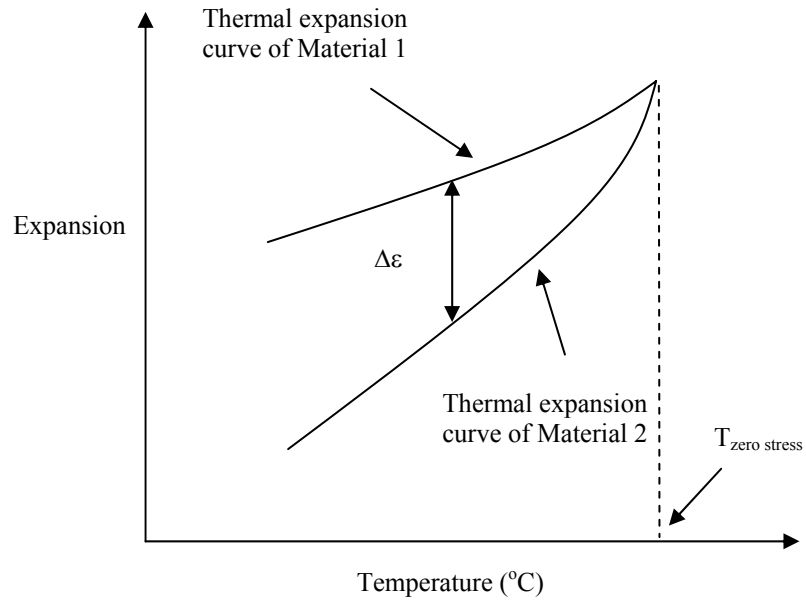
Figure 3.9 Methodology of determining thermal expansion mismatch strain from the "zero stress temperature" and dilatometeric thermal expansion data.
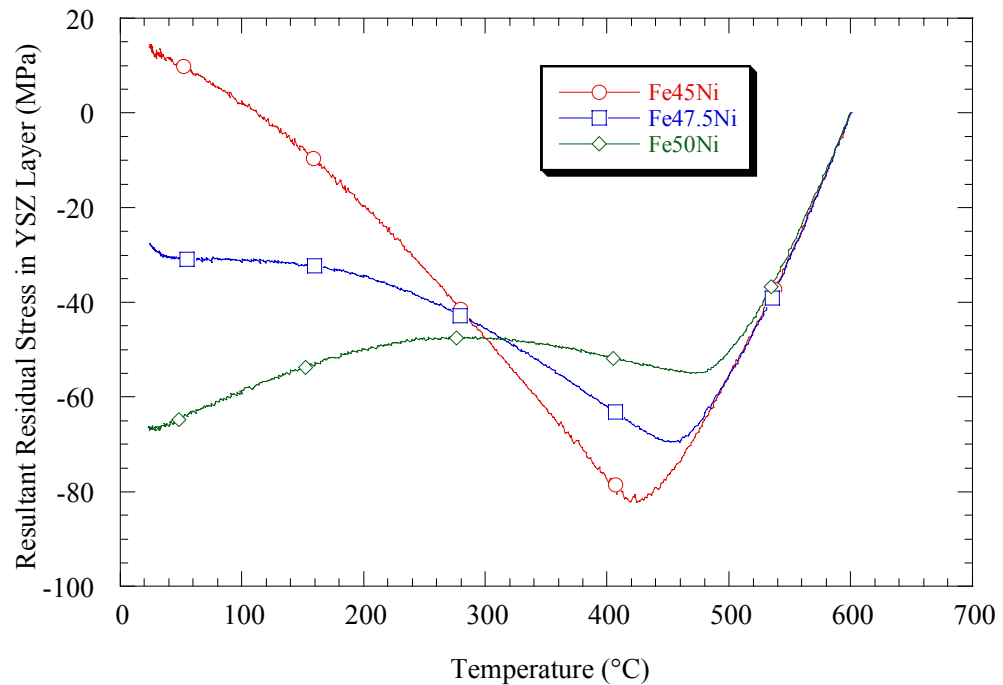
Figure 3.10 Residual stress evolution within the YSZ layer as a function of temperature. Assumes a zero stress temperature of 600°C. Symbols are only to differentiate curves and do not represent actual data.

$$\sigma_1 = \frac{\Delta\varepsilon(T)}{(1/E_1' + t_1/t_2 E_2')} \qquad\qquad (3.9.1)$$

where $E'_x = E_x/(1 - \nu_x)$ (E is Young's modulus and ν is Poisson's ratio) and t_x is the thickness of layer 'x'.

Variation of the zero stress temperature realigns thermal expansion curves and the evolution of residual stress will vary as a function of zero stress temperature. (Figure 3.10) Values for the room temperature stress can be extracted from such curves and another graph charting room temperature residual stress as a function of zero stress temperature can be calculated. By comparing these values to those measured experimentally would allow for extrapolating the value of the actual zero stress temperature.

3.9.2 Additional Model Parameters

3.9.2.1 Density

Specimen densities were measured using Archimedes method. Samples were dried in a 60°C oven for several hours. Dry weights (W_D) were recorded and samples were then submerged under water and placed under vacuum for several minutes to saturate any open pores. Measurements were made with samples suspended under distilled water (W_{ss}) and after dabbing with a wet towel to remove excess surface moisture. (W_s) These

three values allow for the calculation of several material parameters. The bulk and apparent densities are given by:

$$\rho_{bulk} = \frac{W_D}{W_S - W_{SS}}$$ 3.9.2

$$\rho_{apparent} = \frac{W_D}{W_D - W_{SS}}$$ 3.9.3

Open porosity (ε_o) – the porosity open to the surface, and closed porosity (ε_C) are given by:

$$\varepsilon_O = \frac{W_S - W_D}{W_S - W_{SS}}$$ 3.9.4

$$\varepsilon_C = 1 - \left[\frac{1}{\rho_{th}} \left(\frac{W_D}{W_D - W_{SS}} \right) \right]$$ 3.9.5

where ρ_{th} is the theoretical density of the material. The total porosity is simply the sum of Equations 3.9.4 and 3.9.5.

3.9.2.2   Mechanical Properties

Mechanical properties for the ceramic were obtained from literature data. Properties for the alloys were measured using ultrasound wave speed measurements from an NCD-1000 Ultrasonic Analyzer. Transducer probes (one for shear and one for longitudinal wave

speed measurements) pressed against the sample and intimate contact is established through an applied coupling agent. The probes emit and receive an ultrasonic pulse. The analyzer determines the time of flight through the sample and provided the thickness and density of the sample is known, Young's modulus and other mechanical properties can be ascertained from the following equations:

$$C_1 = \left(\frac{\lambda + 2\mu}{\rho} \right)^{1/2} \tag{3.9.6}$$

and

$$C_s = \left(\frac{\mu}{\rho} \right)^{1/2} \tag{3.9.7}$$

where C_1 is the longitudinal wave speed, C_s is the shear wave speed and ρ is the material density. μ and λ are Lame's constants from which all relevant mechanical parameters can be determined.

3.9.3   SOFC Platform Residual Stress

Residual stresses were modeled using a modified FORTRAN program developed by LeMasters. [1] The code was originally written to examine stress development in the fuel cell platforms during operation. The program was modified such that it simulates the cooling subsequent to reduction and sintering. The input parameters of the program were the geometry and dimensions of the co-extruded sample. Based on these parameters the code established a discretized set of nodes and elements and subdivided the fuel cell

platform into layers corresponding to the different materials. The results are written in a specific format to correspond to an ABAQUS input file.

Material properties are defined for the metal and ceramic based on experimental and literature data and these were assigned to the respective layers. These parameters were added to the resultant ABAQUS input file and the stress analysis was performed within ABAQUS. The only load in the system results from the thermal strain that evolves due to thermal expansion mismatch of the ceramic and metallic parts. The thermal gradient is established by setting up an initial condition of the system at the zero stress temperature and a final condition of room temperature. The system is also initially assumed to exist in a stress/strain free state. The strains and resultant material behavior are determined from the material parameters. The thermal load is applied over a single time step. These conditions approximate the cooling of the platform during processing.

4 Results and Discussion

The results of this study can be divided into three general areas. The first briefly presents findings related to successful co-extrusion. These include characterization of both the starting powders and the resultant pastes in addition to studies to match the overall shrinkage of the two pastes. The second section regards the thermal processing of the platform. Sintering curves found from dilatometry as well as discussions surrounding the evolution of the metallic interconnect are presented. The final portion discusses the formation of residual stresses in the platform and examines both experimental and theoretical results.

4.1 Powder Characterization

SEM micrographs of the powders used in this study are shown in Figure 4.1. The YSZ powder was reported by the vendor to have an average particle size of 0.3 microns. From the micrograph Figure 4.1A), it is seen that the powder is on the threshold of the microscope's resolution. It is apparent however that the loose powder is agglomerated. Because of the nanosized particles and high agglomeration, we would expect that the maximum solids loading of this powder would be quite low. The magnetite powder (Figure 4.1B) has an average particle size of ~2 μm and is also observed to be agglomerated as well. The particle size distribution appears to be quite wide and the particles themselves appear acicular which is consistent with the crushing process used to
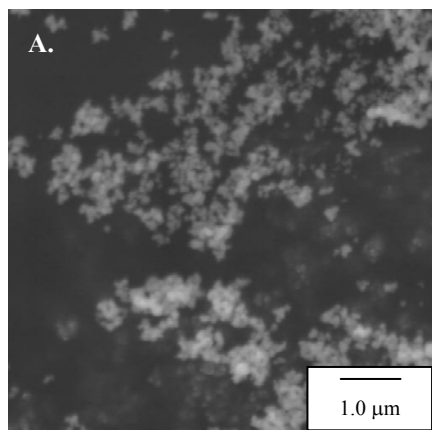
A.

1.0 μm

8mol% YSZ (Daiichi Kigenso Co., dist. by Zirconia Sales (America) Marietta, GA 0.3 μm average particle size.

B.

5.0 μm

Fe_3O_4 (Pea Ridge Iron Ore, Sullivan, MO) 1.8 μm average particle size.

C.

10.0 μm
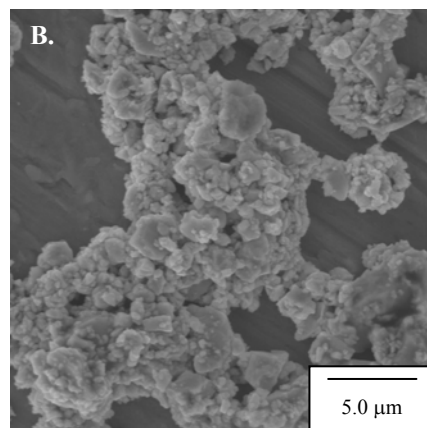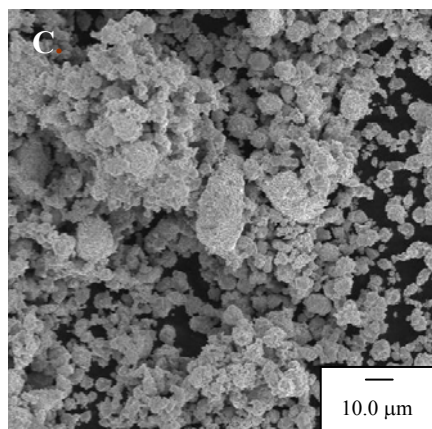
NiO (Ceramic Color and Chemical, New Brighton, PA), 5-40 μm particle size range.

D.

10.0 μm
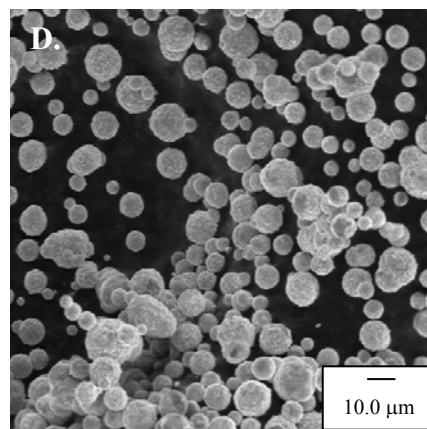
Ni metal (Atlantic Equipment Engineers, Bergenfield, NJ) spherical, 4-10 μm particle size range.

Figure 4.1 SEM Micrographs of the powders used in this study. A) 8mol% YSZ, B.) Fe_3O_4, C.) NiO, D.) Ni metal.

produce this powder. The NiO powder (Figure 4.1C) has an average particle size range of ~5-10 μm) and a rather rough surface but mostly spherical particle morphology. The nickel metal powder (Figure 4.1D) on the other hand has a similar particle size range as the NiO however the spray drying used to produce the powder leaves it with a smoother surface and noticeably spherical morphology.

4.2 Paste Characterization

4.2.1 Shrinkage Studies

Interconnect pastes formed entirely from oxides were found to have a shrinkage much greater than YSZ (~29-30% compared to 22-24%). A preliminary study was conducted to attempt to match the total shrinkage of the interconnect with the electrolyte. This was accomplished for a candidate alloy system of Fe47.5Ni5Cr by adjusting the precursor powders of the metal.

Two adjustments to the initial powder were made. Fine metal powders were incorporated as a substitute for oxide powder in the initial blend to reduce the shrinkage associated with reduction. The packing fraction for the interconnect pastes were also adjusted by altering the ratio of fine/coarse powders. A combination of magnetite (~2-10 μm), NiO (~5-40 μm), Ni (~4-10 μm) and Cr metal (~20-75 μm) served as the coarse, base powder and fine hematite (~0.2-0.5 μm) was incorporated as the fine powder. With an average particle size an order of magnitude lower than the other powders, this powder
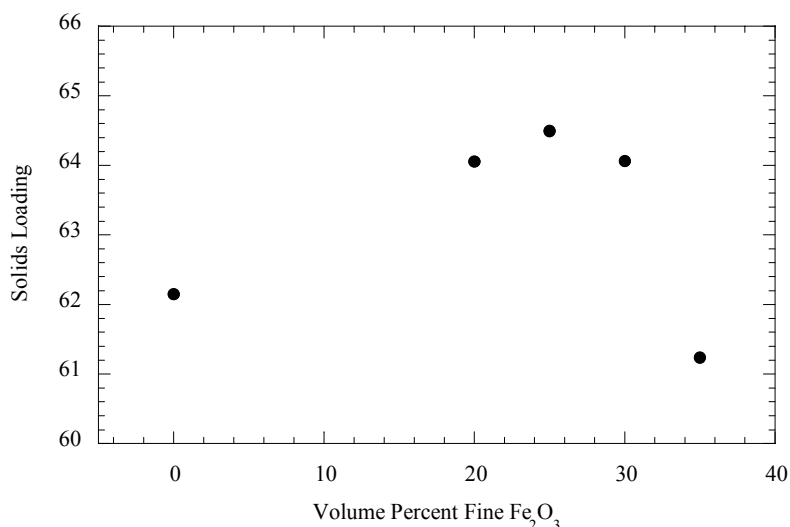
Figure 4.2 Packing fraction of Fe47.5Ni5Cr sample as a function of fine hematite powder volume. (Coarse powders from magnetite, Ni and Cr metal)

is capable of interstitial packing. It was established in Figure 4.2 that modifying the distribution of coarse to fine powders could change the packing volume for a powder compact. As the fine Fe_2O_3/coarse powder ratio increases, solids loading initially increases as the hematite fills the interstitial spaces of the coarse powders, but drops off as the fine hematite powder begins to dictate the overall packing behavior. Maximum solids packing is expected to occur between ~25-30% fines. This was found to be the case. Increased packing efficiency only changed solids loading ~2.5%, but this did not translate to a significant shrinkage reduction as will be further discussed.

Pastes from six different variations were extruded and examined, and the final shrinkage results are summarized in Table 4.1. The trends outlined in the table demonstrate that incorporation of a mixture of fine/coarse powders and Ni metal both tend to reduce the overall shrinkage. It is apparent that substitution of metal for oxide has a more drastic effect than simply adjusting packing fractions of the powder. Compositions with complete nickel metal substitution had the lowest overall shrinkage

and were amongst the best candidates for overall shrinkage match with YSZ. For this reason, over the rest of the study, Ni metal was used as a substitute for NiO.

Table 4.1 Reduction and sintering shrinkage of Fe47.5Ni5Cr alloy as a function of powder composition. It was seen that metal substitute reduced shrinkage greater than increasing amounts of fine powder.

Wt% Metal Composition Derived From:							% Shrinkage
Fine Fe_2O_3	Fe_3O_4	Ni metal	NiO	Cr metal	Fines ratio	Ni metal /NiO ratio	
0	47.5	0	47.5	5	0	0	**29.28**
22.0	25.5	23.75	23.75	5	25	50	**25.57**
0	47.5	35.6	11.9	5	0	75	**26.23**
21.4	25.1	35.6	11.9	5	25	75	**24.29**
0	47.5	47.5	0	5	0	100	**22.86**
20.9	26.6	47.5	0	5	25	100	**22.81**
						YSZ	**22-24**

4.2.2   Paste Rheometry

Rheometry values are outlined in Table 4.2. The Fe-Ni pastes are fabricated from Fe_3O_4 and Ni metal powders. The solids loadings associated with each paste are ~80% of the experimentally derived ϕ_{max} values (maximum possible solids loading). The yield shear stress values for all pastes were found to lie within the ideal 300-600 kPa range where extrusion is optimal. [31] The shear stress values for the Fe-Ni and YSZ pastes were close enough that it would be expected they would co-extrude well. This was found to be the case. There is little difference in yield shear stress and wall shear stress values amongst the three Fe-Ni compositions indicating that the compositional variation is not significant enough to alter rheology between the pastes.

Table 4.2 Paste rheometry data for SOFC components.

Sample	σ_o (kPa)	τ_o (kPa)	Solids loading
Fe50Ni	463.40	42.74	48 v/o
Fe47.5Ni	407.53	55.05	48 v/o
Fe45Ni	459.35	52.42	48 v/o
YSZ	338.01	39.38	34 v/o

4.3   Sintering Curves

Sintering curves for individual and combined compositions of fuel cell components supplies a large array of information regarding densification of the SOFC platform. Individual curves provide a small picture of mechanisms and other phenomena regarding sintering and shrinkage. Comparisons of various curves allow predictions of how multiple material systems will behave and how to manipulate curves to achieve desired results.

This section presents a variety of graphs outlined as follows: Sintering curves of individual components of the SOFC platform are presented to establish how each material behaves. Sintering graphs of the Fe-Ni alloys are then given to discuss how the various powders interact with one another during sintering. Finally, comparisons are made between the electrolyte and interconnect(s) sintering curves to prompt discussion of sintering mismatch between the two materials and possible measures to minimize this occurrence. All curves follow the temperature/time profile outlined in Figure 3.5.

Figure 4.3 to Figure 4.8 are sintering curves related to the individual components (YSZ, Fe_3O_4, Ni, NiO) of the SOFC materials plotted as relative shrinkage versus

temperature. Temperature derivatives of each curve are plotted on a secondary axis to accentuate any particular shrinkage trends along the sintering curves. Figure 4.9 to Figure 4.11 are sintering curves for the Fe-Ni samples and Figure 4.12 to Figure 4.18 summarize the individual sintering curves to highlight the various nuances between plots.

4.3.1   Nickel Sintering Curves

Two possible sources of nickel metal were investigated. Figure 4.3 shows the pushrod dilatometer sintering curve for Ni metal powder and Figure 4.4 exhibits the sintering trends for NiO powder examined in both the pushrod and non-contact dilatometer. Figure 4.5 compares the Ni metal/NiO sintering curves and Figure 4.6 gives additional insight and detail by comparing the derivatives of the two curves. Nickel does not undergo any temperature dependent phase transformations so any features on its sintering curve are expected to strictly be due to diffusional and/or microstructural related phenomena.

The nickel metal does not exhibit any significant shrinkage until ~550°C at which point it reduces ~3%. This is attributed to the initial stages of sintering where necks begin to form between particulates and it is observed to be the portion of the curve with the quickest sintering rates. Densification proceeds at a constant rate until about 1050°C where there is believed to be a transition from intermediary to final stage sintering.

The NiO curve exhibits an additional displacement beginning at ~350°C which is attributed to the reduction of the oxide. This peak is not observed for the Ni metal. Both the kinetics and the overall shrinkage are seen to be greater for the NiO sample recorded

74
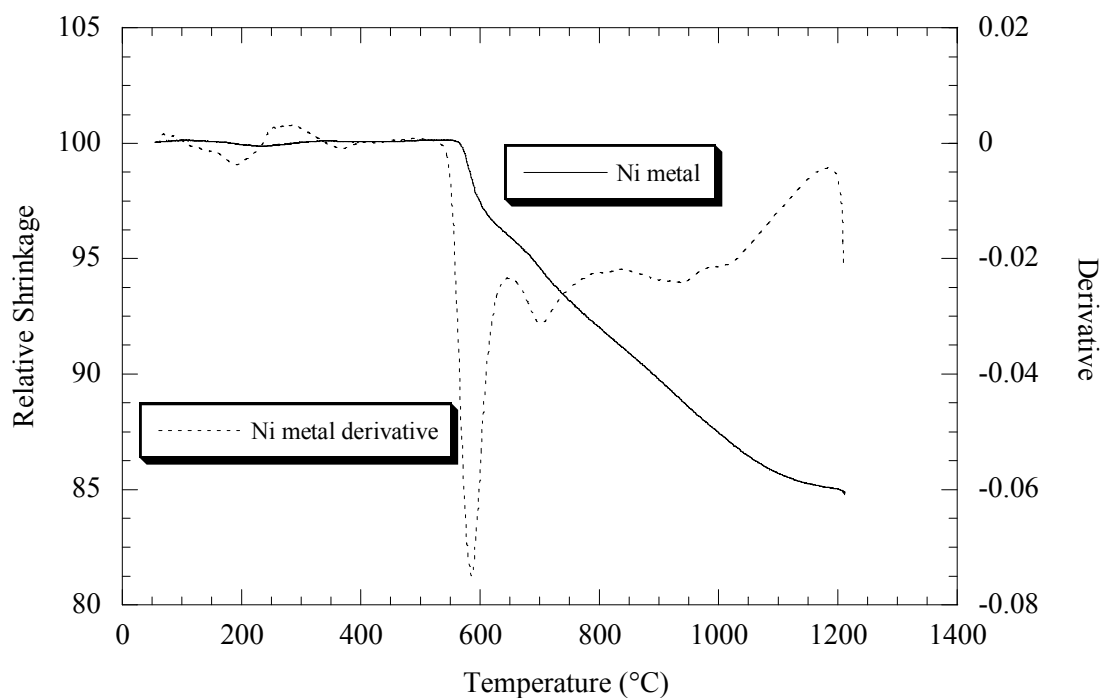
Figure 4.3 Ni Metal curve and derivative as measured by the pushrod dilatometer.
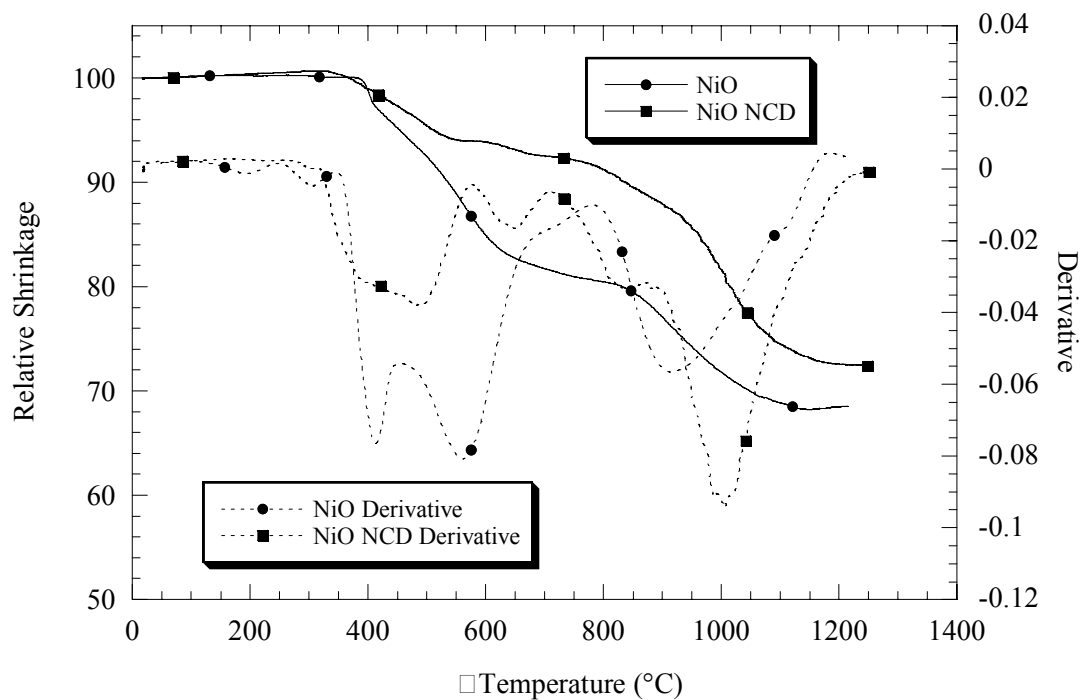
Figure 4.4 NiO curves and derivatives as measured and determined by ● - pushrod dilatometer, ■ - non-contact dilatometer.

in the pushrod dilatometer compared to the NCD. This indicates that there is likely still some additional pressure exerted upon the sample in the pushrod dilatometer. Despite this fact, much valuable insight is provided from this data and both were used to characterize sintering.

After the onset of reduction, the NiO compact initially begins to densify at ~350-375°C. The NiO sample is seen to shrink ~6-8% from ~350-500°C. Sintering rates increase from this point and diminishes in both instruments around ~700-750°C and increases once more at ~850-900 °C until the set point temperature is approached. At this point, shrinkage begins to taper off and conclude.

Shrinkage of the compact begins earlier in NiO due to reduction. Eisele [63] showed that compacts of Fe_3O_4 and NiO shrink ~5-8% during reduction. At ~550°C, sintering continues as in the case of Ni metal and the pushrod NiO shrinks ~20% while the NCD NiO shrinks ~10% up to ~750, 800°C. At this point densification slows. This is most likely attributed to the disappearance of free surfaces (eliminating that diffusional mechanism) and the reduction of driving force as the network of interparticle necks transforms into interconnected pores and subsequently isolated pores. The resurgence of sintering at ~800°C is believed to be due to a transition towards grain boundary and volume diffusion as the compacts grow dense enough to form grains. As Figure 4.5 and Figure 4.6 demonstrate, this sequence does not occur for the Ni metal. This could possibly be due to the high spherodicity of the Ni or perhaps other morphological aspects of the green or reduced NiO.
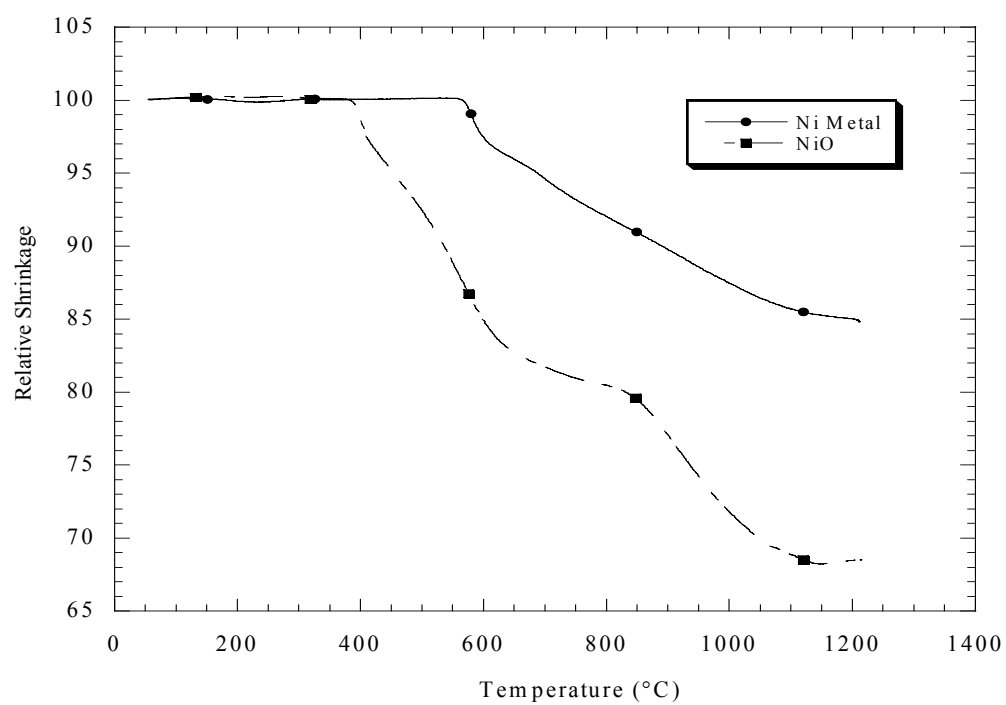
Figure 4.5 Ni/NiO sintering curve comparison.
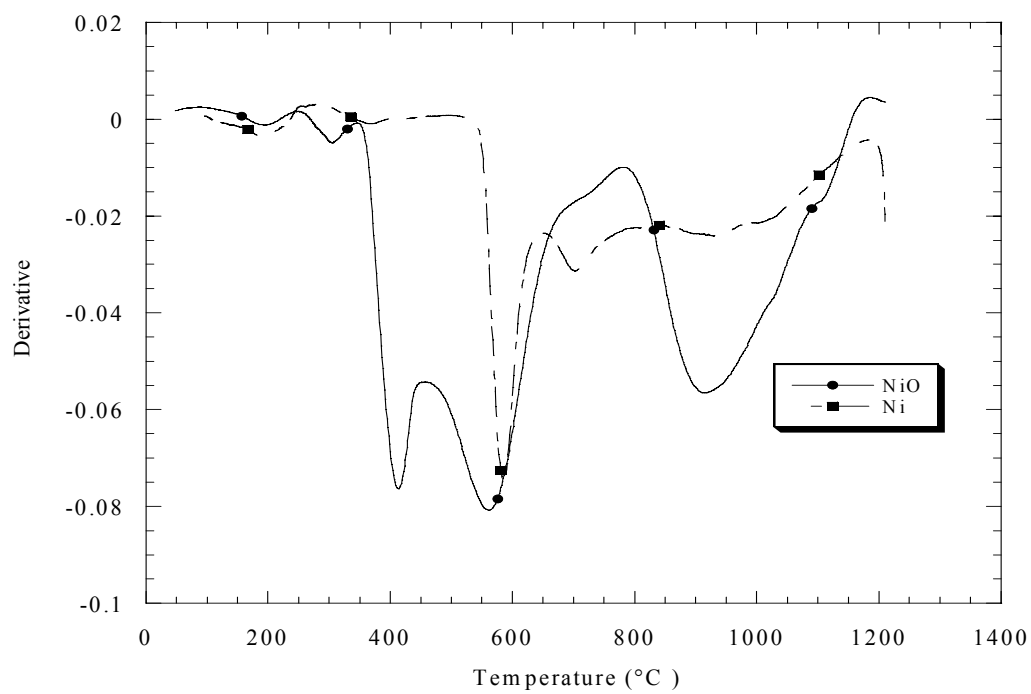
Figure 4.6 Ni/NiO sintering curve derivative comparison.

4.3.2   Iron Sintering Curves

The sintering curve and associated derivative for the Fe_3O_4 samples are illustrated in Figure 4.7. Unlike nickel, there are a number of phase transformations that occur over the sintering temperature range. Binder burnout occurs at ~280°C. Reduction and shrinkage of the green sample begins at ~350°C in the pushrod dilatometer and occurs at an increasingly higher rate until ~600°C. Densification then slows at progressively slower rates (as evidenced by the waves/peaks) until ~915°C. At this point the sample shrinks ~5% at an extremely high rate after which sintering essentially ceases and the compact in fact appears to exhibit a slight expansion.

As observed in the nickel, shrinkage initiates and proceeds at a slower rate in the NCD, with the maximum rate reached at ~800°C. Densification then slows and ceases at ~920°C and as with the pushrod dilatometer, a slight expansion is initially observed in the sample.

The initial reduction in sintering rates is probably due to the formation of iron. Diffusion of iron is dependent on the formation and migration of vacancies. Due to the magnetic ordering of iron, the free energy of vacancy formation and migration increases and atomic diffusion correspondingly diminishes. [77] The Curie temperature for α-iron is 770°C. Since diffusion is a thermally activated process, the diffusion coefficient should increase logarithmically per the Arrhenius equation. However above the Curie temperature, this coefficient increase is seen to flatten out [78] implying that sintering rates should also level out above this point. The magnetic ordering effects not only serve to inhibit diffusion but also to minimize thermal expansion. Once these effects disappear,

diffusion should be allowed to proceed normally, however the onset of the paramagnetic state also introduces a transition in thermal expansion and the increased thermal motion of the atoms impedes diffusion within the lattice.

The sudden arrest in sintering at ~910°C coincides with the ferrite (α) $\rightarrow$ austenite (γ) transformation in iron. This phase change encompasses a crystallographic transformation from a body centered cubic (BCC) structure to a face centered cubic (FCC) structure. The packing fractions for each of these phases are 68% and 74% respectively and so the abrupt change in dimension at ~910°C is attributed to the crystallographic phase transformation. Since diffusion occurs more readily in the lower density BCC structure, it is expected that the sintering rates will diminish above this once the transition to FCC has occurred.

The expansion observed after the ferrite to austenite transformation can be attributed to two possible phenomena: metallic thermal expansion or the occurrence of closed pores and the associated high gas pressure which serves to inhibit volume reduction of the pores. In light of the sudden shrinkage and reduced capacity for diffusion in the sample, any residual porosity would most likely be closed with little chance of further reduction. Therefore the cause of expansion is most likely the latter of the two occurrences. Ivensen [79] reported similar observations in sintered nickel and copper powders noting that densification diminished with increasing green density (higher amounts of closed porosity). Ivensen also cited additional work where the compaction of copper powder under vacuum was demonstrated to sharply reduce the expansion effects during sintering, even at higher green densities. It is expected however
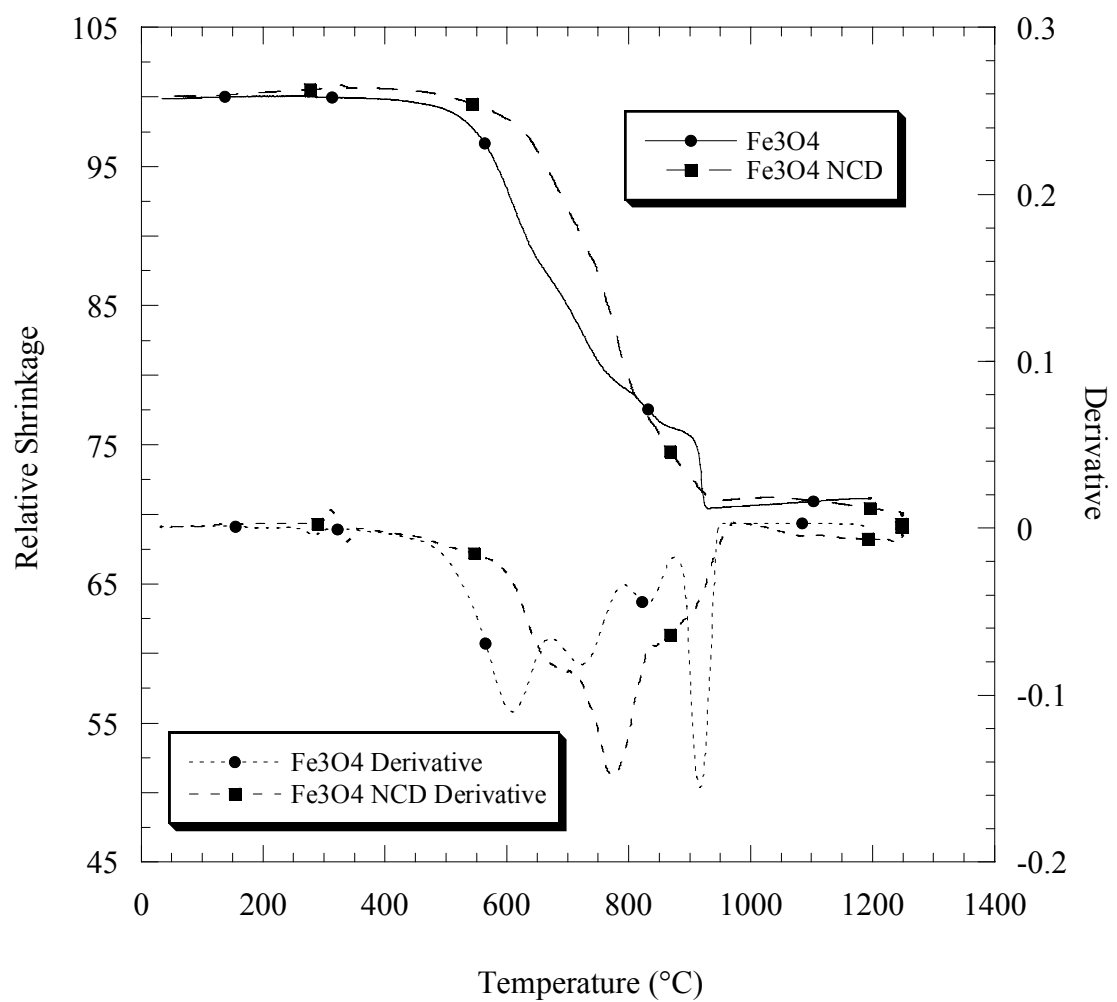
Figure 4.7 Fe₃O₄ curves and derivatives as determined by ● - pushrod dilatometer ■.- non-contact dilatometer.

that longer hold times or higher sintering temperatures would allow for sintering to resume.

4.3.3   YSZ Sintering Curve

The sintering curve for YSZ obtained from the pushrod dilatometer is shown in Figure 4.8. The initial shrinkage is caused by binder and lubricant burnout and possibly loss of oxygen under the low oxygen partial pressure atmosphere. The sample expands until ~1000°C at which point the compact possesses enough thermal energy for diffusion and densification to commence.
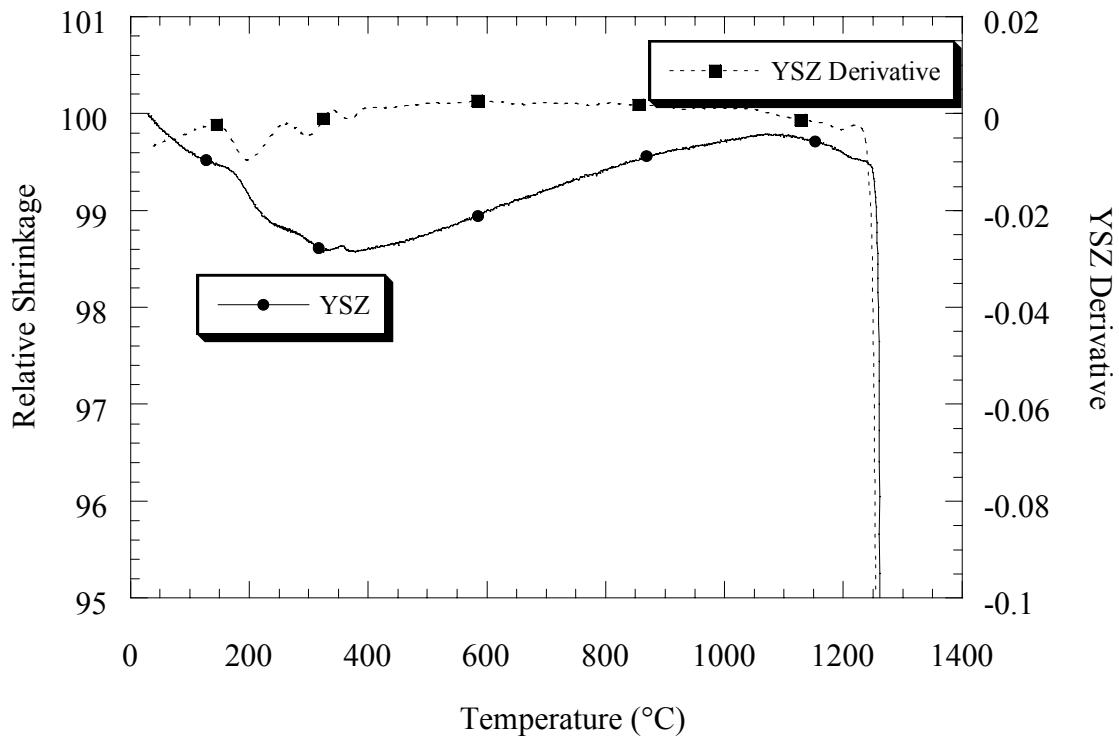
Figure 4.8 YSZ sintering curve and derivative.

4.3.4   Fe-Ni Sintering Curves

Sintering curves for the various Fe-Ni alloys that were co-extruded with the YSZ are shown in Figure 4.9 to Figure 4.11. Curves from both the non-contact and pushrod dilatometers are included. All samples are observed to follow very similar trends. Burnout of the processing aids occurs between 200-350°C. Shrinkage begins at ~450°C for the pushrod samples which arises from reduction of the oxide. For the NCD samples, the onset of reduction shrinkage is delayed to latter temperatures, presumably because of the absence of pushrod forces. Densification slows in both instruments, almost plateauing at ~900°C and resumes up to the setpoint temperature.

Figure 4.12 plots all of the pushrod dilatometer curves discussed to this point. It is interesting to note that the Fe-Ni samples have shrinkages in between that of the nickel and Fe_3O_4 base components. The traces also appear to follow densification paths intermediate between the two primary powders. None of the Fe-Ni compositions match well with the YSZ plot suggesting that a substantial degree of constrained sintering should arise within this system.

Figure 4.13 graphs the pushrod dilatometer temperature derivatives for the Fe-Ni samples as well as the original Fe_3O_4 and nickel powders. Reduction of all the Fe-Ni samples is noticed to occur faster than that of the lone magnetite compact. The catalytic properties of Ni are well known and it is believed that the nickel metal's role in dissociating gaseous hydrogen leads to increased reduction kinetics. It is interesting to
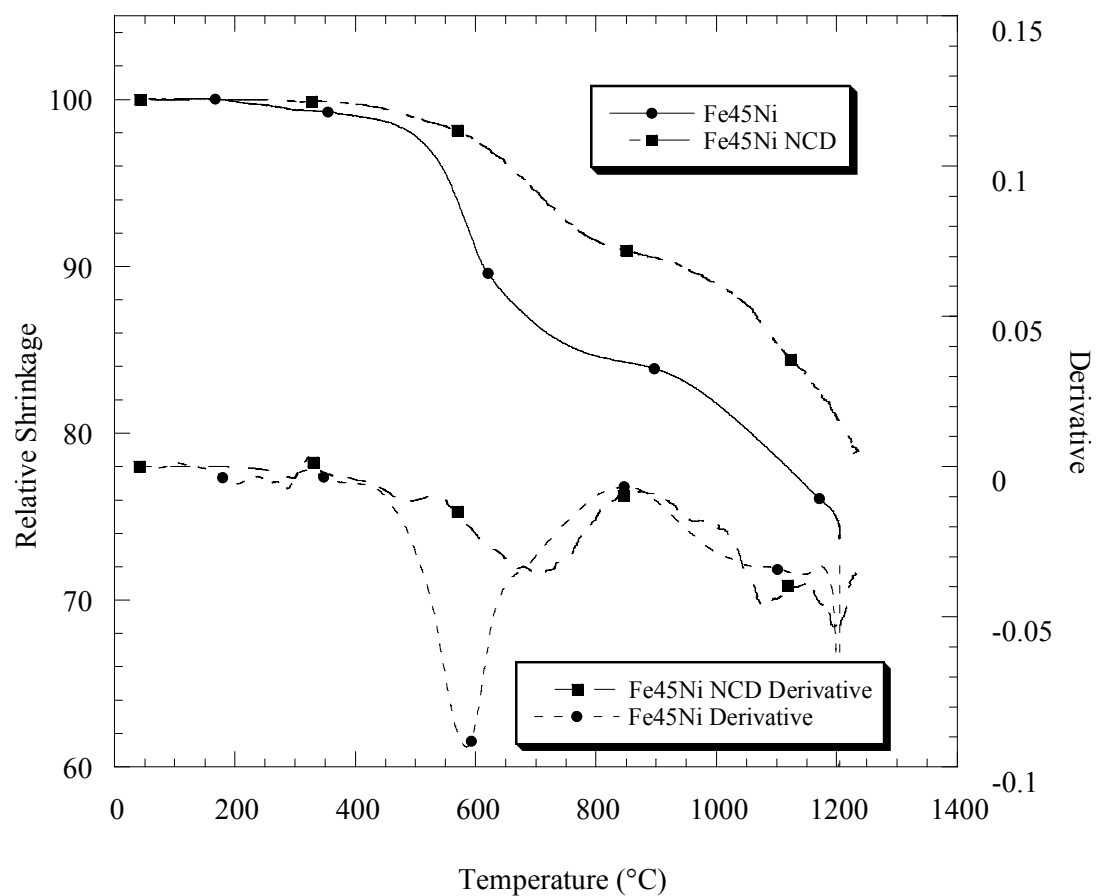
Figure 4.9 Fe45Ni curve and derivative as determined by ● - pushrod dilatometer, ■ - non-contact dilatometer.
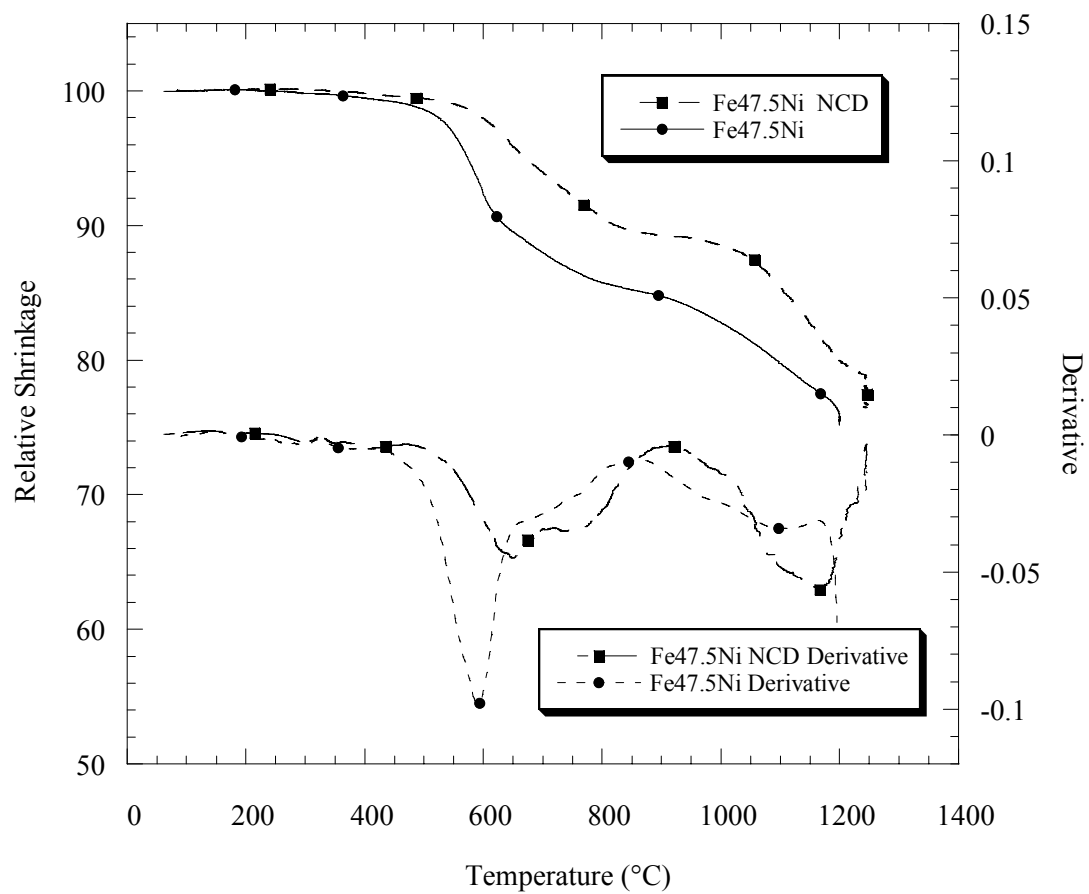
Figure 4.10 Fe47.5Ni curve and derivative as determined by ● - pushrod dilatometer, ■ - non-contact dilatometer.
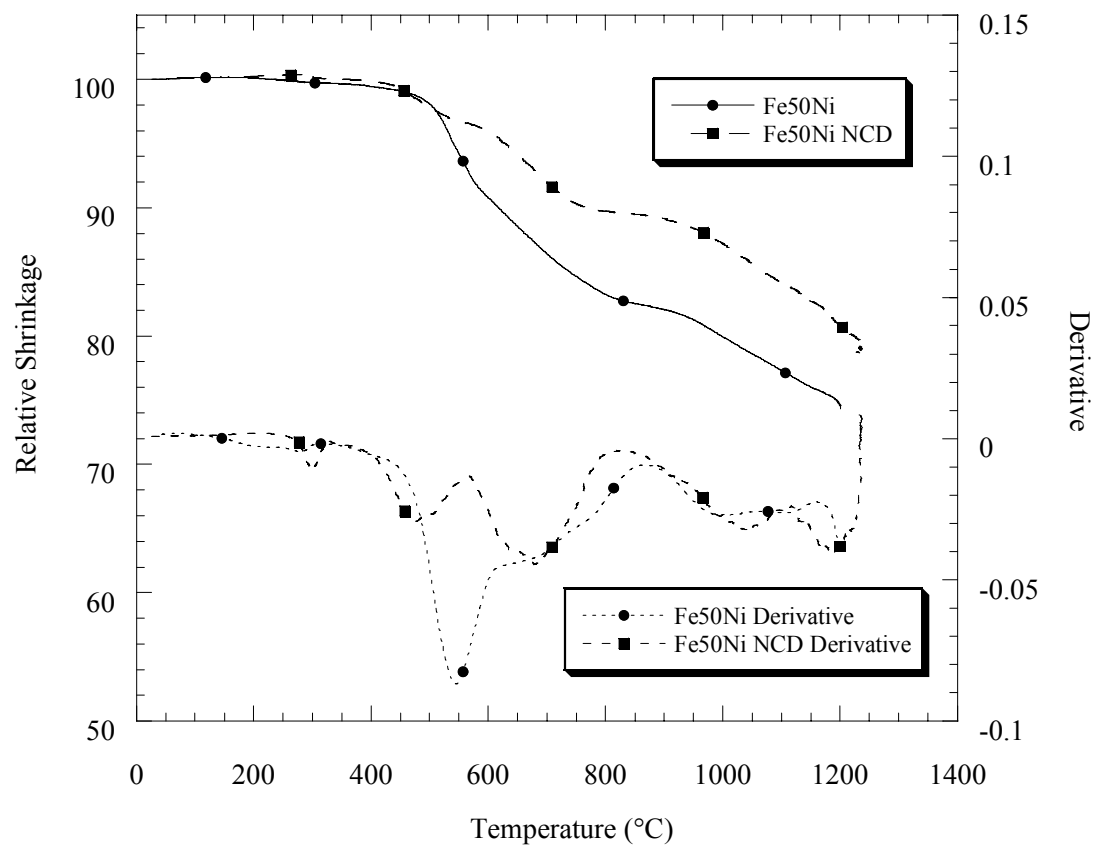
Figure 4.11 Fe50Ni curve and derivative as determined by ● - pushrod dilatometer, ■ - non-contact dilatometer.
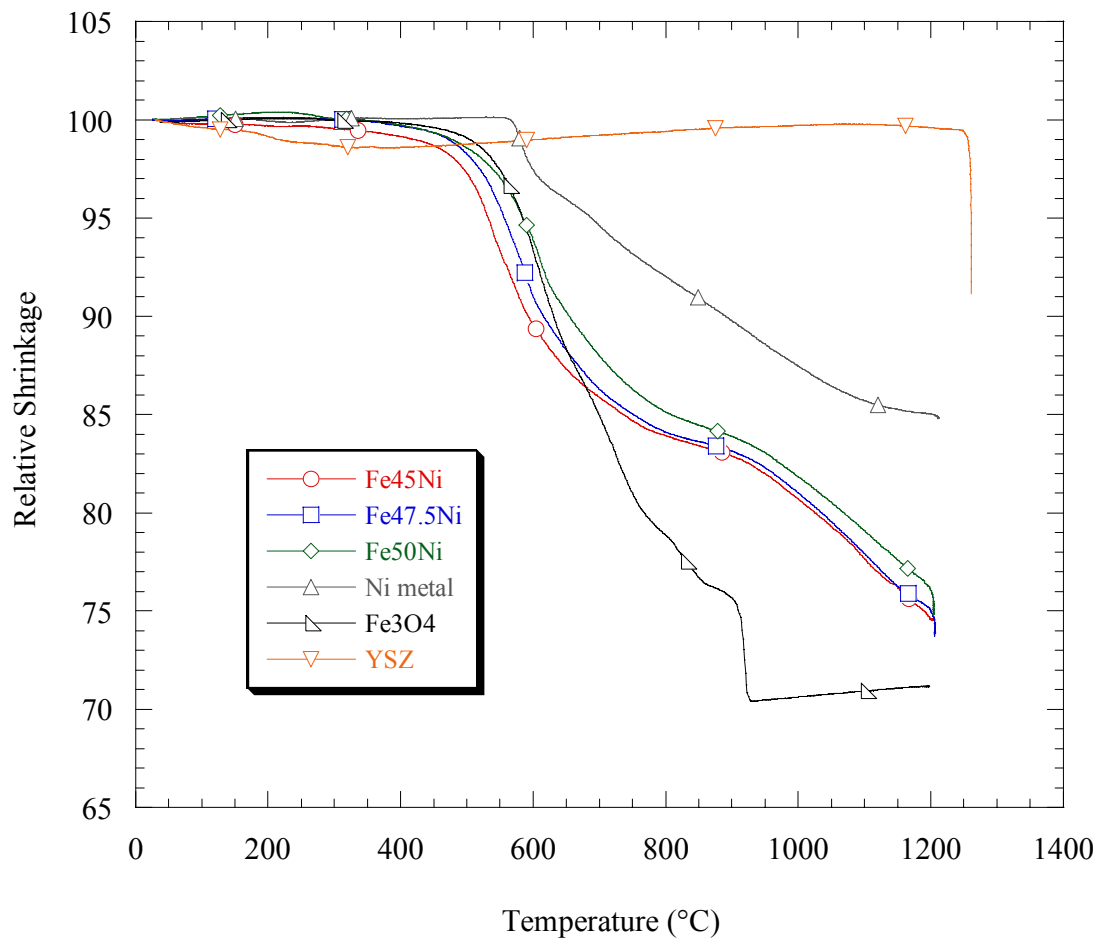
Figure 4.12 Summary of the sintering curves obtained from pushrod dilatometry.
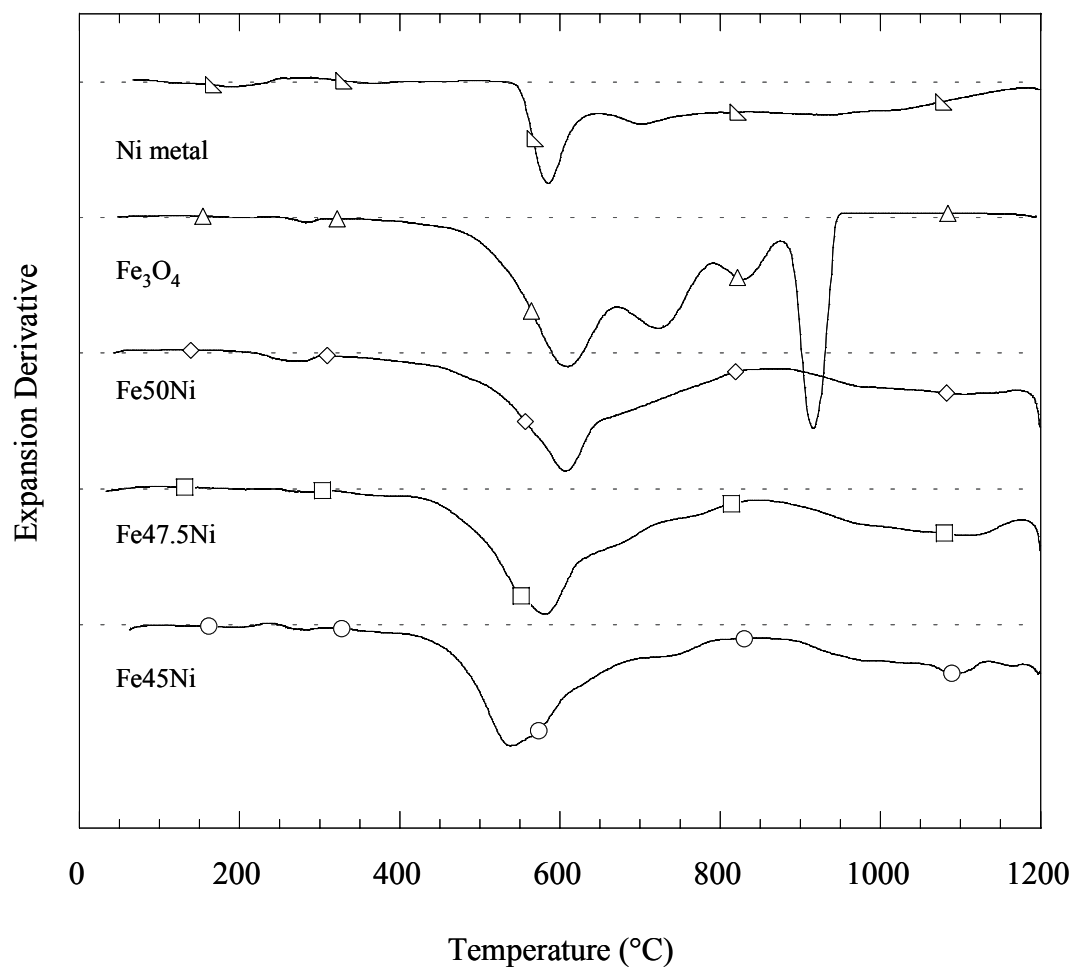
Figure 4.13 Temperature derivatives of shrinkage curves of Fe$_3$O$_4$, Ni, and Fe-Ni compositions. Curves are separated for clarity and dashed lines represent the zero axes for each plot. Symbols only serve to differentiate curves and do not represent actual data points. Curves are plotted on a scale of arbitrary units and offset for visual clarity.

note that an increase of nickel does not quicken the completion of reduction. The Fe45Ni rather than the Fe50Ni sample is observed to reduce the most rapidly. This signifies that there should be an optimal magnetite/nickel ratio. It also suggests that the presence of a reduced, porous network of iron, amenable to gaseous flow, is more important than the presence of the catalytic nickel metal.

Figure 4.14 plots the Fe-Ni sintering curves obtained from the non-contact dilatometer. From the traces, it is seen that reduction shrinkage concludes around 700-750°C and further sintering occurs between 1000-1250°C. Figure 4.15 compares the temperature derivatives of both the pushrod and NCD curves. It is readily apparent once again that despite the experimental efforts, the pushrods still exert forces upon the sample. The reduction and initial sintering curves for these plots are sharper and larger compared to the non-contact dilatometer curves and their onset begins at a lower temperature. The implication of these observations is that the compact is weakest and most porous after burnout of the organics and oxide reduction. Since only particle contact forces exist at this point, even the minimal force of the pushrods creates an artificial shrinkage. While data from the individual instruments may give cause for concern, the information together allows deduction of a more accurate picture of the sintering events.
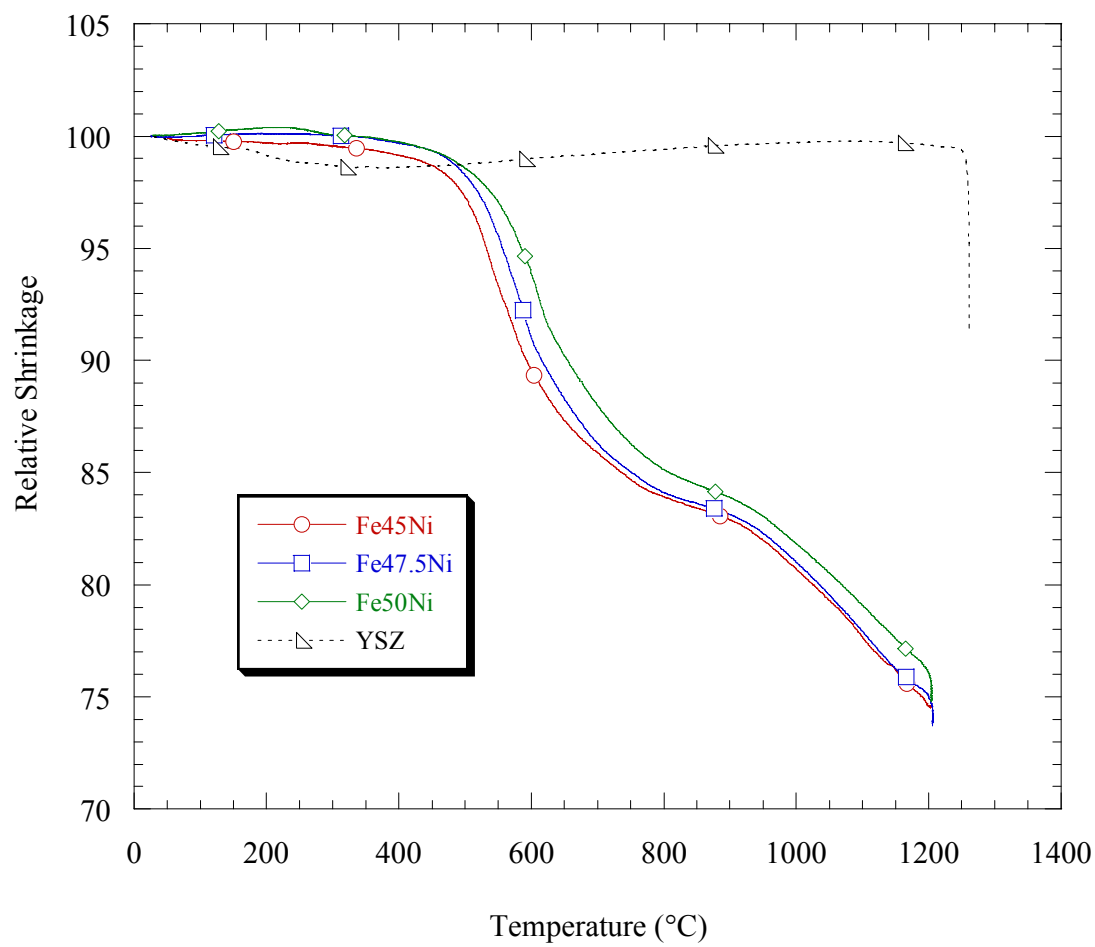
Figure 4.14 Non contact dilatometer traces of Fe-Ni samples.
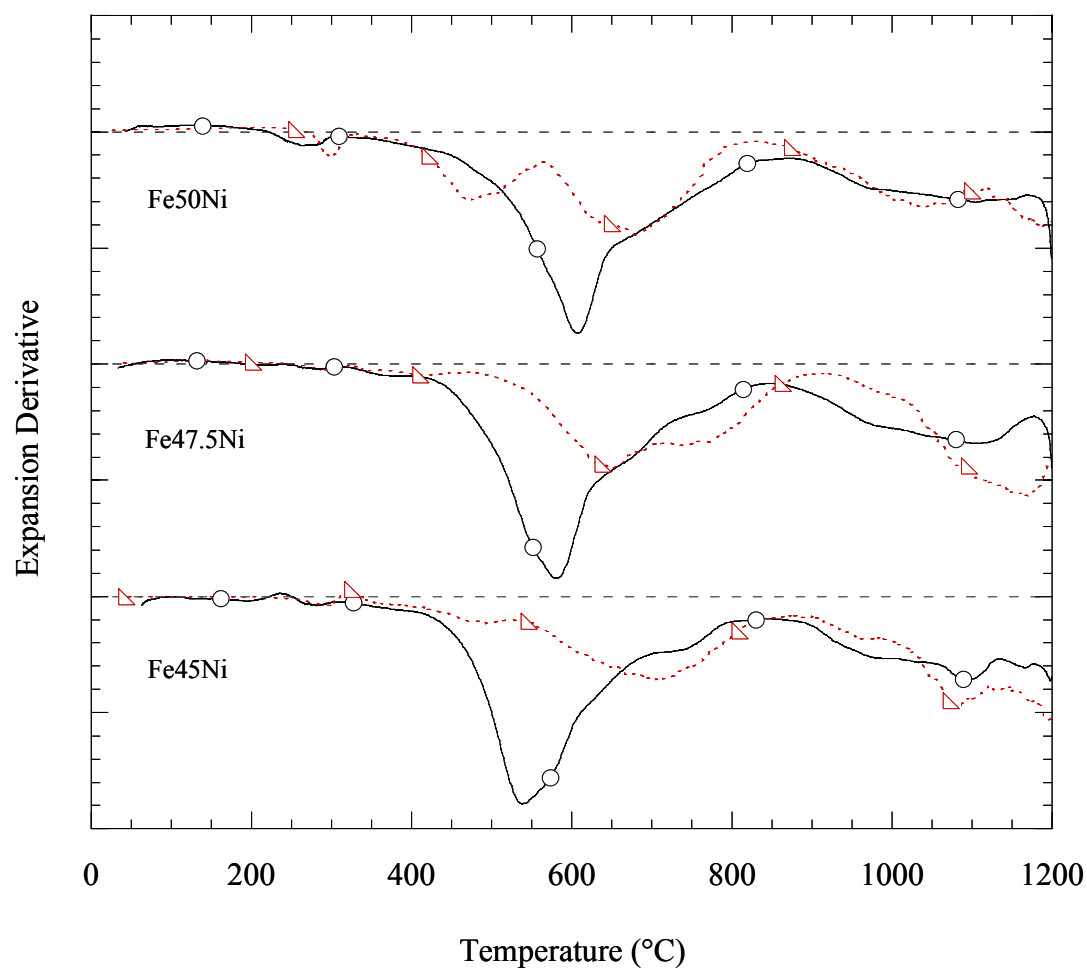
Figure 4.15 Temperature derivative curves for both pushrod (–, solid black lines) and non-contact dilatometer (▲, dashed red lines) curves for Fe-Ni samples. Curves are plotted in arbitrary units and offset for visual clarity.

4.3.5   Influence of Sintering Atmosphere

Figure 4.16 illustrates the effect of atmosphere on sintering for a Fe50Ni sample. In the absence of hydrogen gas, reduction does not occur and sintering of the magnetite/nickel compact does not commence until ~850°C. Total densification of the compact reaches ~15%. Figure 4.17 shows that the introduction of hydrogen at latter stages of the firing schedule has an immediate impact and reduction begins instantly. The sample densifies ~5% and sintering continues the remainder of the schedule. However, the total shrinkage is observed to be several percent lower than that obtained from the normal firing schedule. This is presumed to be due to the pinching off of an open network of pores as reduction and sintering occur more rapidly at the higher temperatures. However, since the onset of densification for YSZ does not occur until 1000°C, there will still be an appreciable amount of mismatch regardless of manipulation of the atmosphere.

4.4   Sintering Stress

Figure 4.18 shows the Fe-Ni and YSZ densification curves in direct comparison. The differences between the sintering curves are apparent. A rough estimate of the sintering stress can be found from the differences between these curves. Figure 4.19 charts these values showing the evolution of the sintering mismatch. It is seen that within this compositional range, there is little difference between the sintering mismatch. Since the interconnect portion of the platform will densify earlier, a constrained sintering
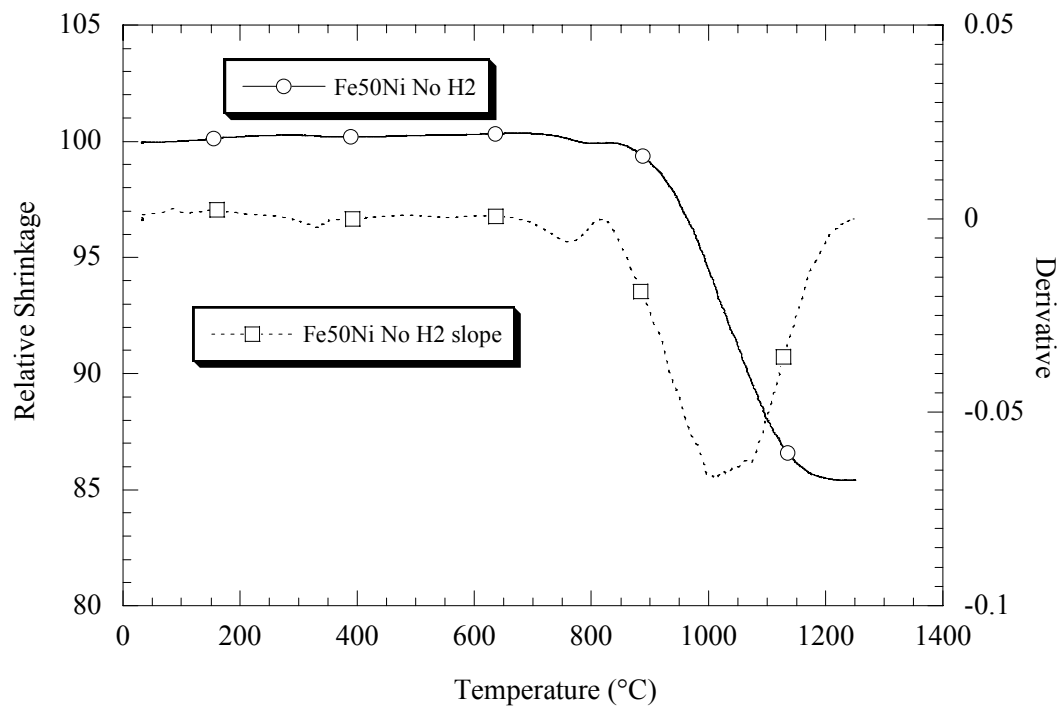
Figure 4.16 Sintering curve and temperature derivative of Fe50Ni fired in the absence of hydrogen. Experiment was conducted in the non-contact dilatometer.
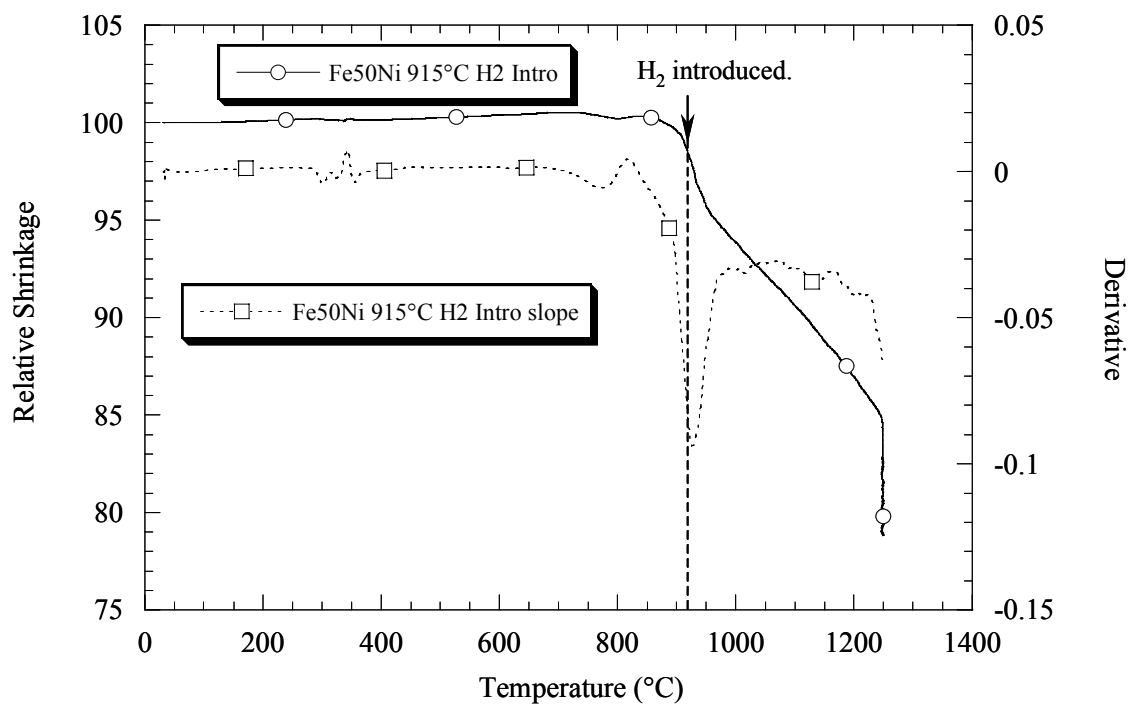
Figure 4.17 Sintering curve and temperature derivative of Fe50Ni sample initially fired in an inert atmosphere, and introducing hydrogen at ~915°C. Experiment was conducted in the non-contact dilatometer.
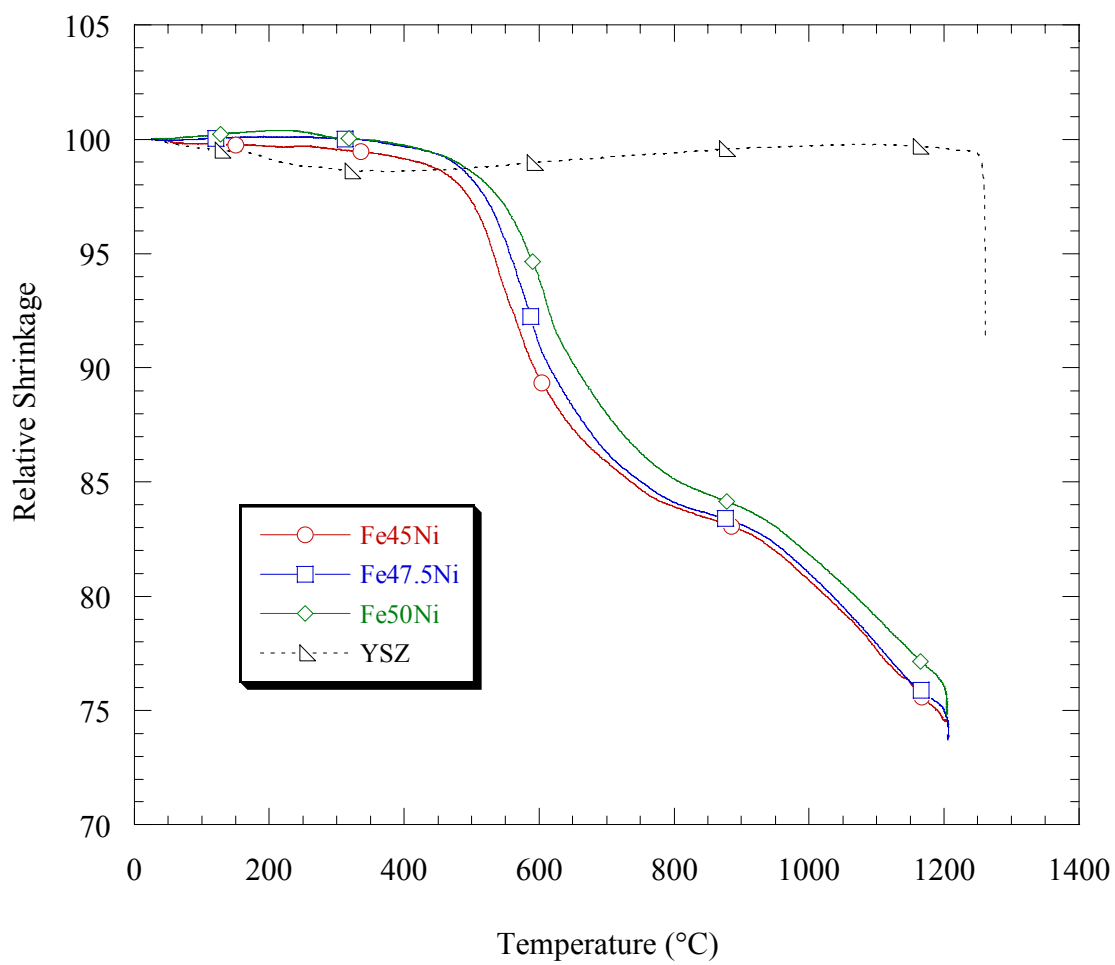
Figure 4.18 Pushrod dilatometer sintering curves for the Fe-Ni interconnect compositions and YSZ.
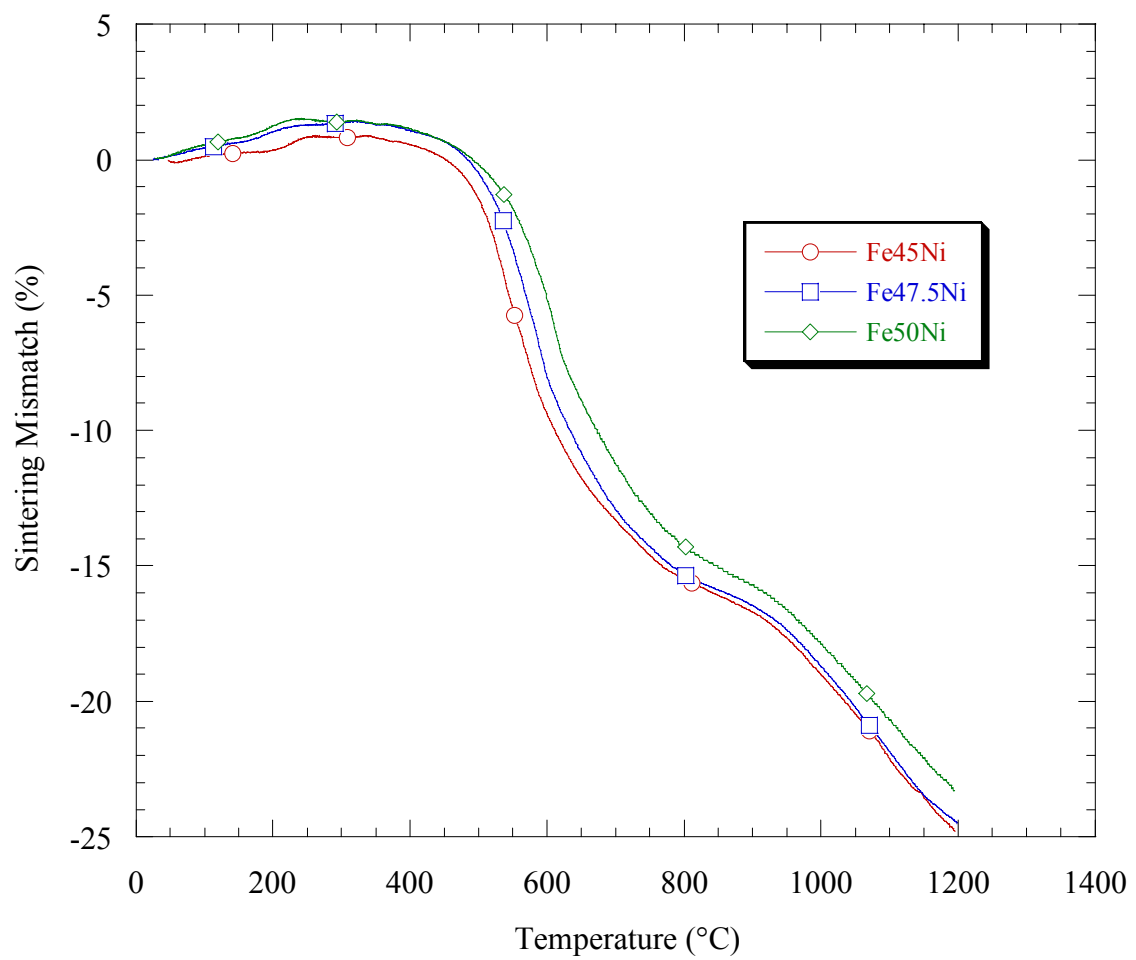
Figure 4.19 Sintering mismatch curves between the YSZ electrolyte and Fe-Ni interconnects.

situation arises and the metallic portion will experience a tensile stress and the ceramic a corresponding compressive stress as discussed previously. The tensile stress within the metallic layer serves to decrease the overall sintering rate while the associated compressive stress that arises in the YSZ layer should serve to enhance densification. The interaction between the two layers should lead to lower shrinkage rates for the interconnect and increased rates for that of the electrolyte. The sintering behavior of the joined materials would thus be expected to lie between the two free sintering curves. Cheng and Raj [54] reported similar behavior for ceramic/metallic and ceramic/glass laminates. Because of the resultant tensile forces, a higher quantity of porosity is expected in the interconnect layer as the driving force for densification diminishes. On the other hand, the electrolyte layer should appear denser as its sintering behavior is enhanced. This is confirmed by the microstructure shown in Figure 4.20. The amount of porosity in the metallic layer is significantly higher than that in the ceramic layer.
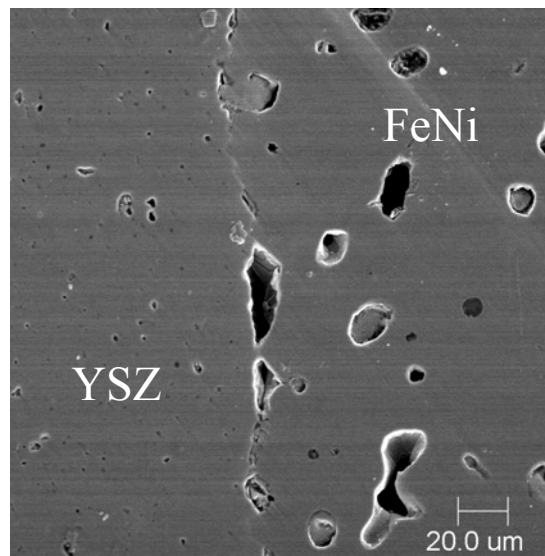
Figure 4.20 Polished cross section of a YSZ/Fe47.5Ni interface.

Figure 4.21 shows a polished cross section of the interconnect for a Fe45Ni/YSZ and Fe47.5Ni/YSZ fuel cell platform. The high amount of porosity is apparent. The average area fraction of porosity in the Fe45Ni sample was found to be ~12.4% and ~6.3% in the Fe47.5Ni sample. This suggests that the Fe45Ni sample has a higher degree of sintering mismatch with the electrolyte, which from Figure 4.19 appears to be the case. While increased quantities of porosity are evident, it should be noted that the porosity remains unconnected so the hermeticity of the metal should not be compromised.

Figure 4.22 illustrates the influence of constraint arising from the vertical walls of the cellular layer. Under the present sintering conditions, the horizontal lengths of the wall are expected to shrink to smaller dimensions than the vertical arms will allow. This manifests itself as an increase in porosity within the horizontal walls. Table 4.3 outlines the open, closed and total porosity values from the three interconnect layers of a Fe47.5Ni/YSZ platform. The center metal layer has a higher quantity of porosity, and it also contains a higher proportion of closed porosity. Both facts lead to the conclusion that a constrained sintering situation in the center metal layer arises from the two surrounding electrolyte layers.

Table 4.3 Archimedes method densities outlining the porosity in the three interconnect layers of a Fe47.5Ni/YSZ platform.

	Outside layer (1)	Center layer	Outside layer (2)
$\phi_{\text{open porosity}}$	12.5%	4.8%	13.2%
$\phi_{\text{closed porosity}}$	5.9%	21.6%	3.1%
$\phi_{\textbf{total}}$	18.4%	26.4%	16.3%
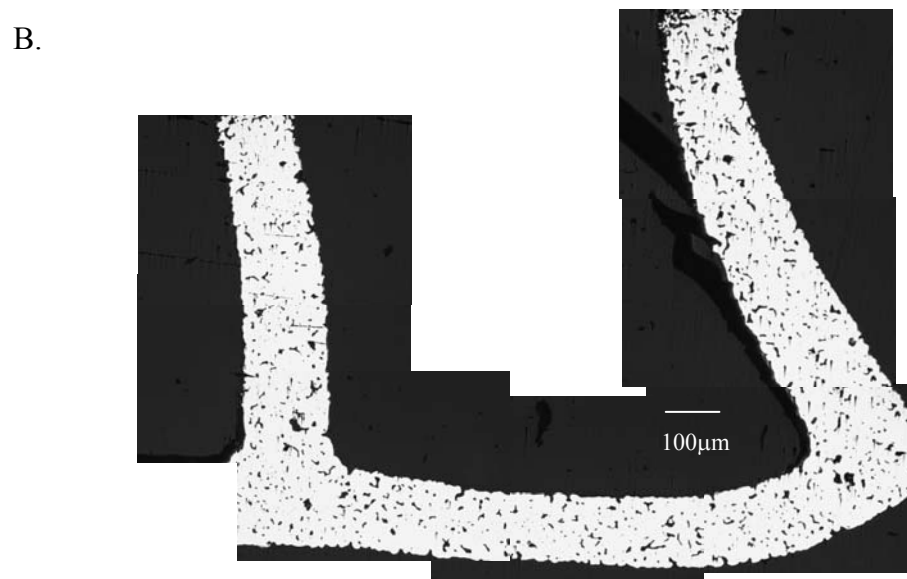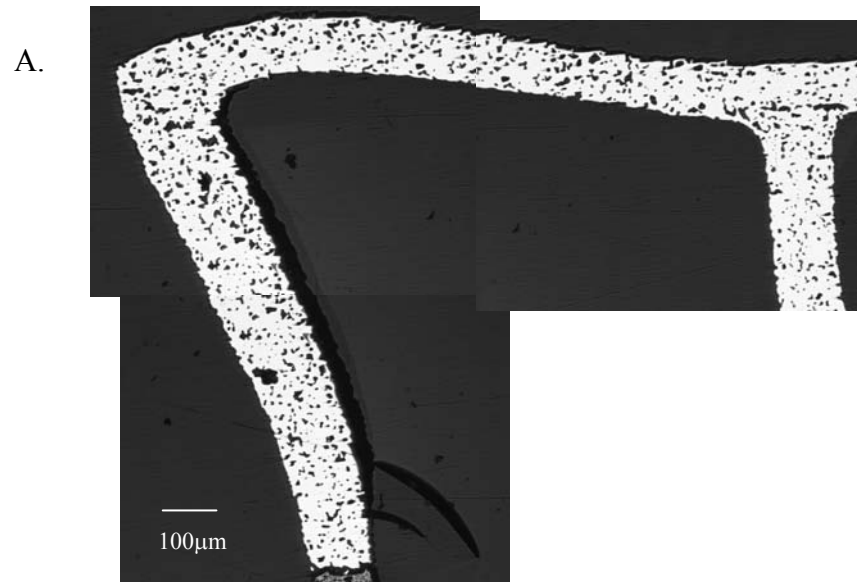
Figure 4.21 Optical micrographs of the polished cross sections for A.) Fe45Ni/YSZ and B.) Fe47.5Ni/YSZ fuel cell platforms highlighting the increased porosity resultant from sintering stresses.

100 μm
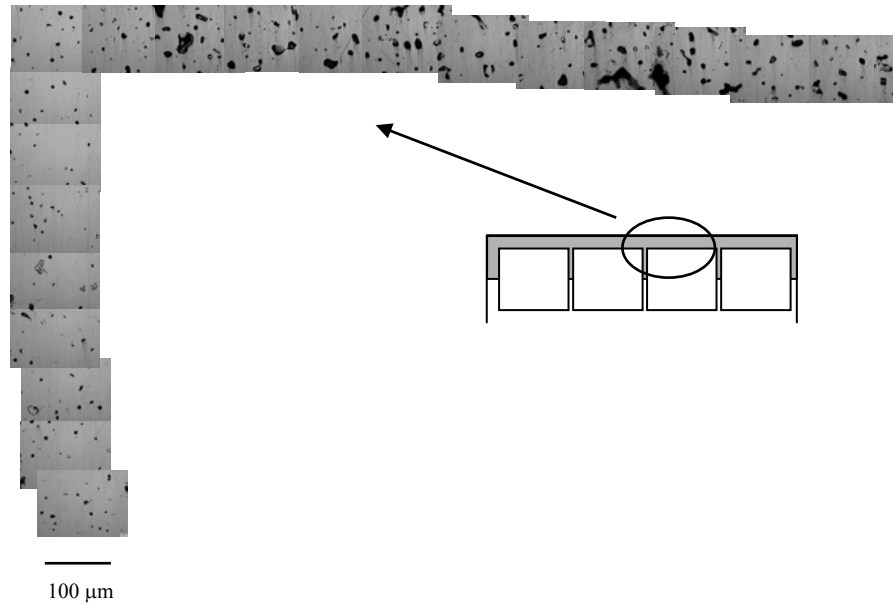
Figure 4.22 Cross section of a polished Fe47.5Ni/YSZ sample illustrating the effects of wall constraints on the microstructure of the interconnect.

As discussed previously, porosity influences a number of key properties including modulus, electrical conductivity and gas permeability. However, the presence of porosity is not necessarily unfortunate. The knockdown effects of porosity upon the mechanical properties could allow for a decreased magnitude in residual stresses through distortion of the interconnect.

4.5 Fe-Ni Phase Evolution

Figure 4.23 shows the characteristic diffraction peaks for green, as extruded Fe50Ni, Fe_3O_4 and Ni samples. Because of chemical similarities, there is some peak overlap, especially at larger angles, but each phase is distinct enough to characterize. For this binary system, possible phases expected over the course of firing include Fe_3O_4, FeO, Ni, Fe, $NiFe_2O_4$ spinel, and γ (Fe, Ni) solid solution. Figure 4.24 tracks the progression of these phases with increasing temperatures.

Fe_3O_4 and Ni are the two phases initially present. These phases persist until 400°C. At 600°C, peaks corresponding to iron metal are found and at 800°C the presence of "sawtooth" like convoluted peaks indicate the formation of the γ (Fe, Ni) solid solution. At this point, there are trace peaks of Fe_3O_4 indicating that reduction is not fully complete. At 1000°C, Fe_3O_4 and nickel have disappeared. Trace peaks of iron are observed at this point implying that iron diffuses into nickel to form the solid solution. This is also consistent with Matsuyama *et. al*'s [80] findings which were established by the basis of self-diffusion and interdiffusion coefficients.

$$D_{Fe} \rightarrow D_{Fe} > D_{Fe} \rightarrow D_{Ni} > D_{Ni} \rightarrow D_{Fe} > D_{Ni} \rightarrow D_{Ni} \qquad (4.4.1)$$

The γ (Fe,Ni) phase is the primary phase at this point and at 1200°C this is the only phase present. The existence of wustite (FeO) is not observed through XRD characterization, which is not surprising as this phase is not thermodynamically stable at room
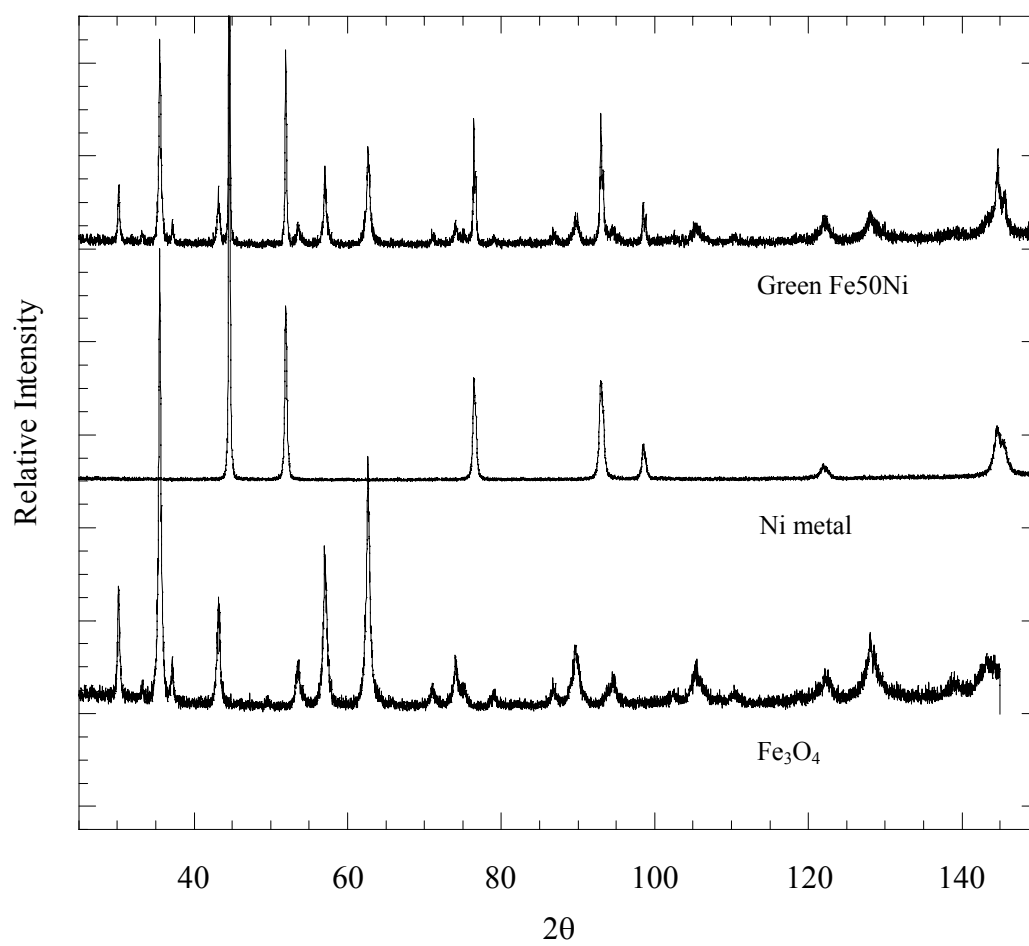
Figure 4.23 XRD peak profiles of Fe$_3$O$_4$, Ni metal, and Green Fe50Ni samples.
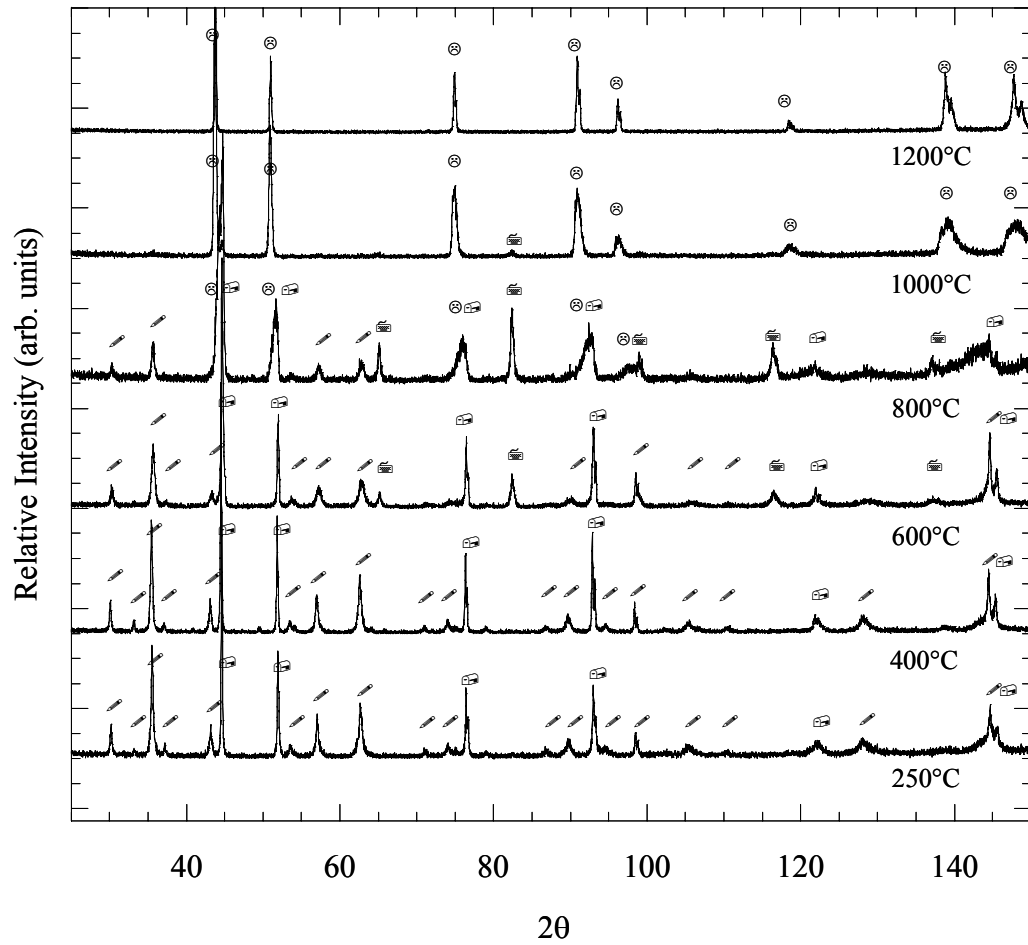
Figure 4.24 XRD peak profiles of Fe50Ni sample as a function of temperature illustrating the evolution of various phases: ! - Fe₃O₄, , - Ni, 7 - Fe, Λ - γ (Fe, Ni). Samples were heated to the indicated temperature and furnace cooled to room temperature for XRD analysis.

temperature as shown by the Fe-O phase diagram in Figure 4.25. The eutectoid temperature for wustite is 570°C. Below this temperature, FeO will decompose into magnetite and iron via the following reaction:

$$4Fe_xO \leftrightarrow Fe_3O_4 + (4x-3)Fe \qquad (4.4.2)$$

This decomposition of wustite on cooling is a possible explanation for detecting magnetite at the higher firing temperatures in Figure 4.24.
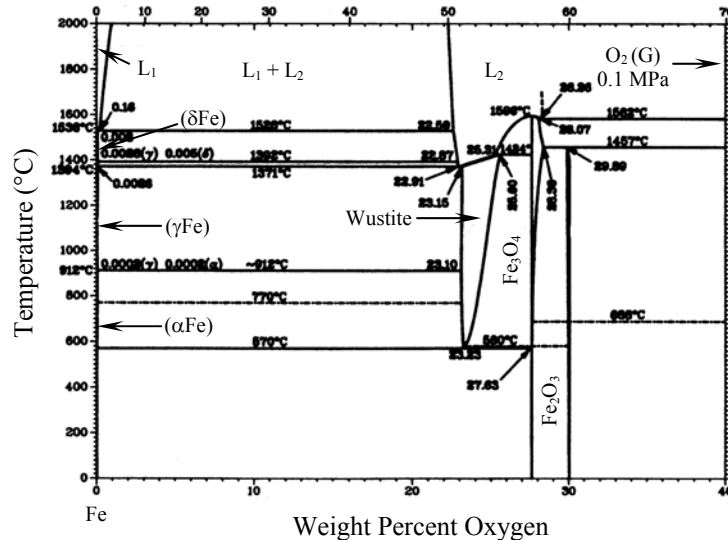
Figure 4.25 Fe-O phase diagram. After [23].

Figure 4.26 tracks the microstructural evolution of the reduction and sintering of a Fe50Ni sample processed and fired as described in previous sections. EDS and its spherical morphology allow for the nickel particles to be distinguished within the first several micrographs. The smaller particles in the 600°C micrograph indicate the
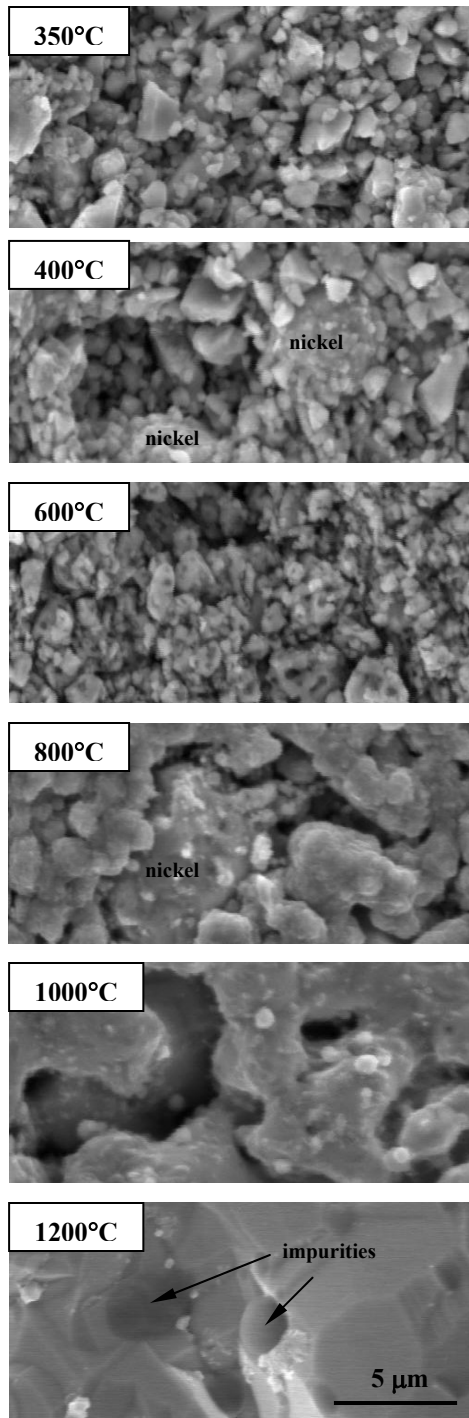
Figure 4.26 Scanning electron microscope photographs of Fe50Ni samples heated to and quenched from the listed temperatures. All micrographs were taken from an as-fired state at a magnification of 5000x. The presence of nickel particles and impurities are labeled.

impending completion of magnetite reduction that is implied by Figure 4.11 and Figure 4.24. Significant grain growth and particle bonding are seen at 800°C although separate nickel and iron particles are still prevalent. Increased bonding and additional coarsening are also evident at 1000°C as a network of interconnected pores is formed. At 1200°C, the remnant porosity is isolated and the presence of Al/Si based impurities (as determined by electron dispersive spectroscopy) are found on the outside of the grains. These impurities are expected to form eutectic compounds with iron and go into solution at higher temperatures. [41]

Figure 4.27 summarizes the reduction and sintering of the Fe_3O_4/Ni compacts. The sintering curve of a Fe50Ni sample is plotted alongside the corresponding weight loss curve as well as a description of phases present from Figure 4.24. A complete picture of the sintering of the Fe-Ni interconnects is now formed. Binder and lubricant burnout results in little shrinkage but a significant amount of weight loss. Reduction of the magnetite results in a substantial shrinkage and weight loss. However at this point (~600°C), there is little strength imparted on the sample due to the lack of inter-particulate bonds. Densification slows as neck formation between particles and coarsening indicate that surface diffusion is the prevalent mechanism for atomic motion. The ridges observed on the surfaces of the grain also support the notion of surface diffusion dominating sintering. [41] As grain boundaries are formed and with the increase of temperature (~1000°C), grain boundary and volume diffusion begin to dominate sintering and densification proceeds. This idea is also supported by the observation that the bulk interdiffusion of iron and nickel to form the γ solid solution phase readily occurs
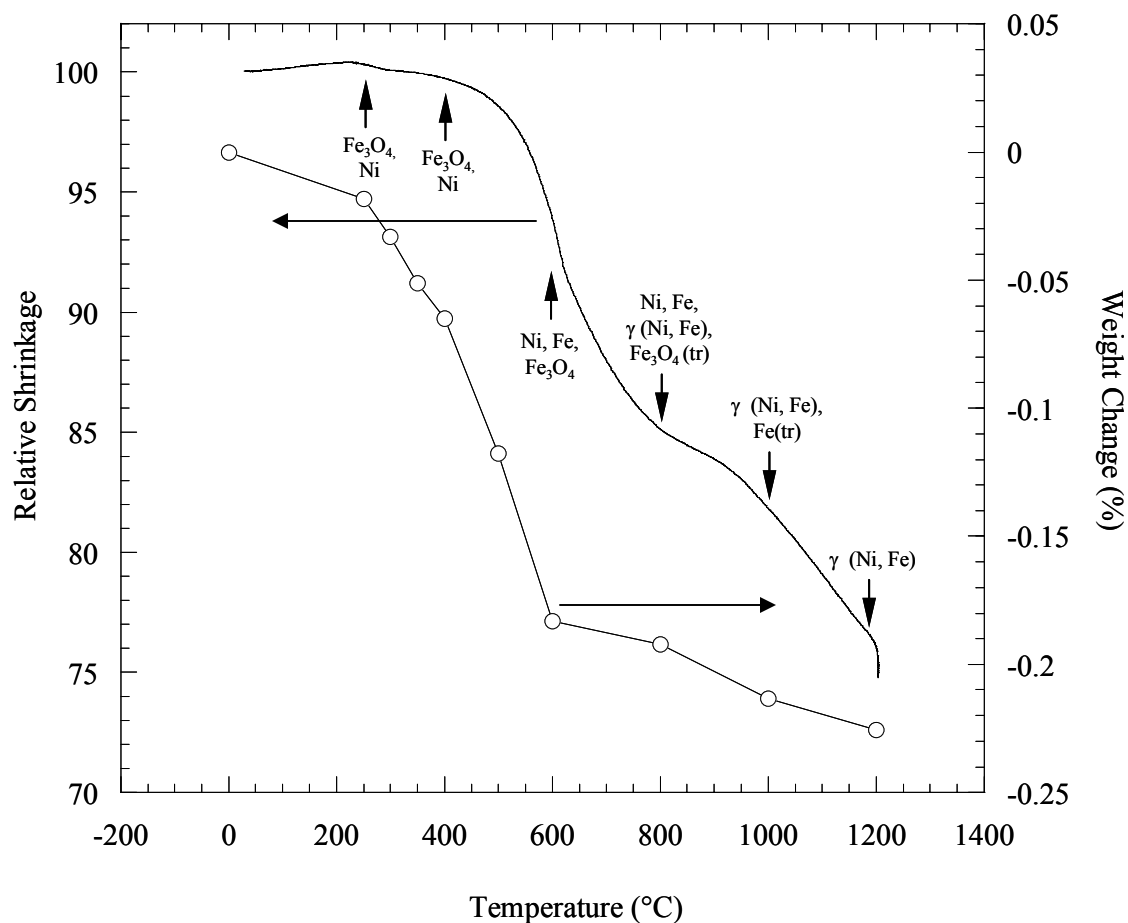
Figure 4.27 Summarization of the reduction and sintering of a Fe50Ni sample. The relative shrinkage, weight loss, and phase evolution are included. The sintering trace was obtained from a pushrod dilatometer while the phases (arrows) and weight loss (o) were obtained from various samples heated to the indicated temperatures and quenching to room temperature. Trace amounts of certain phases are indicated by the (tr) adjacent to that phase.

at these temperatures. There is still a relatively large amount of open porosity at this point as seen in Figure 4.26, which is seen to disappear at the final sintering temperatures with corresponding grain growth in the microstructure.

4.6   X-Ray Diffraction Stress Measurements

Figure 4.28 shows a micrograph of the interconnect potion of the as reduced fuel cell platforms. It is apparent that the interconnect suffers from severe grain growth and is observed to have an average grain size of ~30-60 microns. Given the small XRD beam size, these large grains made it prohibitive for a random orientation of planes to be measured. As such, measurements were focused towards the zirconia side of the platform.
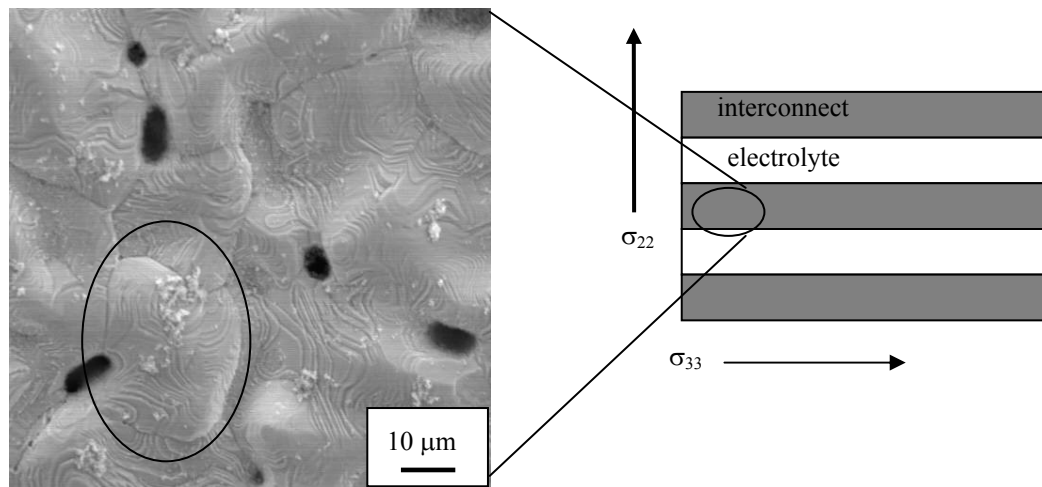
Figure 4.28 Micrographs illustrating the discrepancy in grain size for the interconnect segment of the fuel cell platform.

.
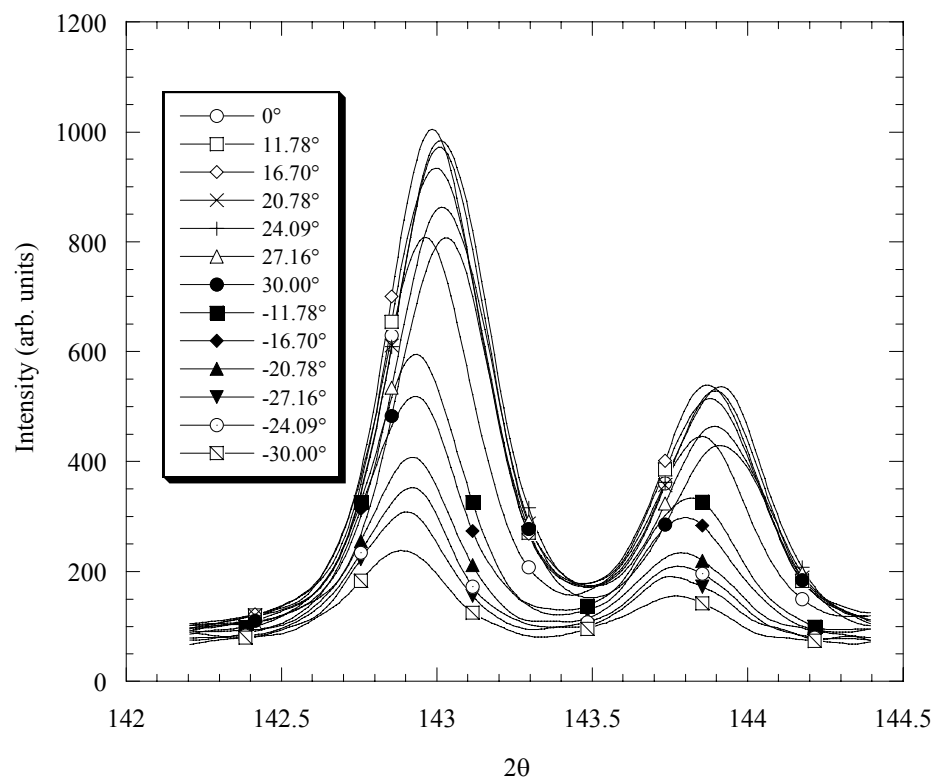
Figure 4.29 XRD peaks (YSZ, (620)) measured as a function of ψ angle in the (σ₂₂) direction on the YSZ/Fe45Ni platform. The peak shifts indicate the presence of residual stresses within the layer.

Residual stresses were thus measured in the zirconia layers in directions perpendicular (σ_{22}) and parallel (σ_{11}) to the layers. (Figure 4.28) Figure 4.29 is a smoothed plot illustrating the peak shifts (620 peak) that result within the ceramic layer of the YSZ/Fe45Ni platform. These peak shifts occur due to the change in lattice spacings brought on by the residual stress. Figure 4.30 shows the peak positions of the curves in Figure 4.29 as a function of the ψ angle orientation. The stress analysis software contains a variety of curve fitting algorithms (Gaussian, Lorentzian, Pearson VII, etc.) to determine the peak position. The majority of curves were fit with the Pearson VII algorithm, although others were also employed if minimal error was achieved. It is seen that the 2θ peak position increases linearly with the ψ angle. This indicates an increase in lattice spacing and implies that a tensile stress is acting in this direction. Conversely a decrease in peak position would denote that a compressive stress is acting in the measurement direction.

Using Bragg's law this data is translated into an accompanying plot of d versus $\sin^2\psi$. The separation of the plot into two individual curves for $\psi > 0$ and $\psi < 0$ is known as "psi-splitting" and indicates that the stress state is not purely biaxial within the layer. [75] The biaxial stress analysis assumes that only two principle stresses (σ_{22} and σ_{33} in Table 4.4) exist; however the psi-splitting shows that some shear stresses do exist, perhaps due to a stress gradient within the layer. A straight line is fitted between the two curves and the residual stress is calculated using Equation 2.5.18. The stress free d-spacing (d_o) used in the formula is interpolated from a corresponding $\sin^2\psi_{stress-free}$ value. There are several methods to obtain this quantity, however the value was simply taken to
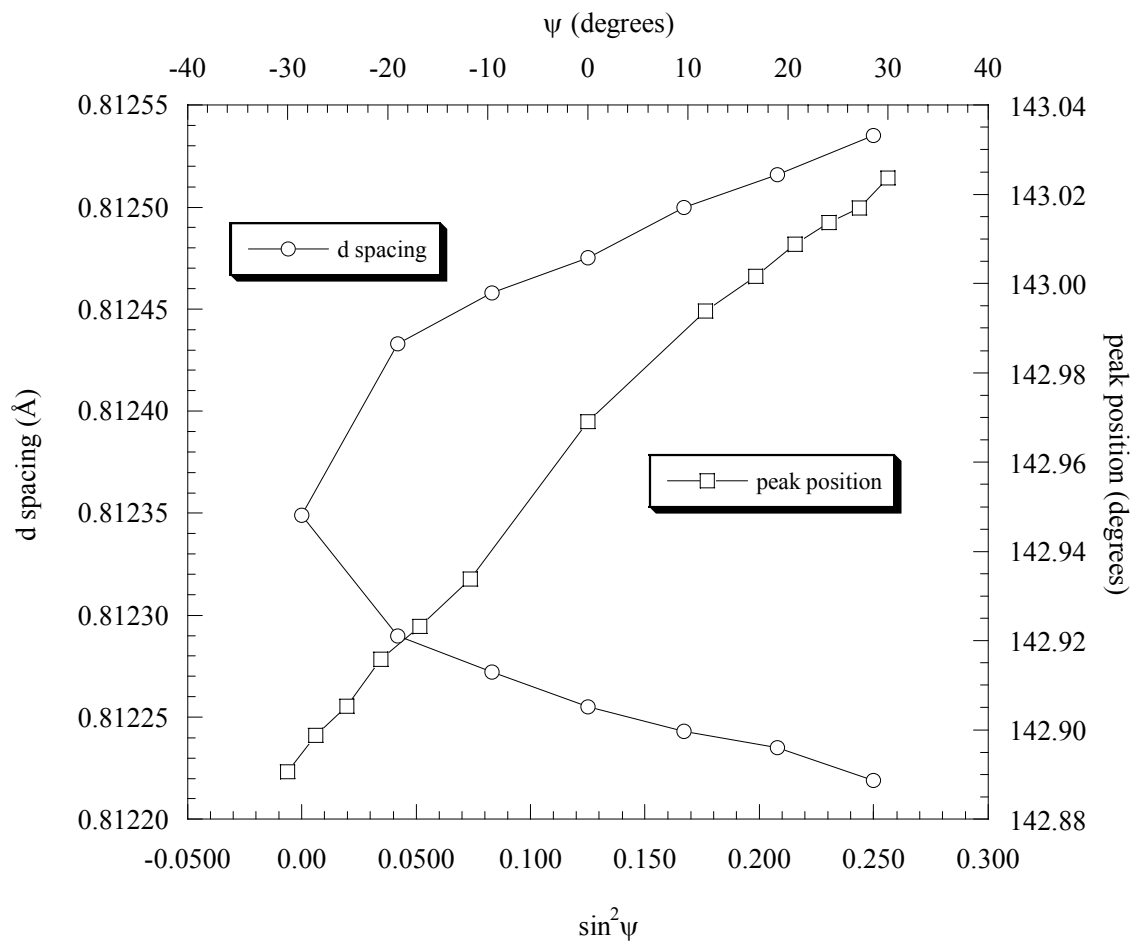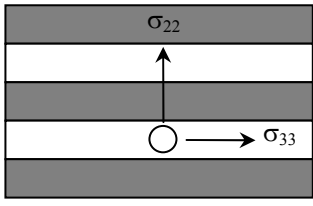
Figure 4.30 Peak position as a function of ψ angle obtained from the curves in Figure 4.29. The data is transformed into a plot of d-spacing against $sin^2\psi$.

be 0.5 (rotationally symmetric, isotropic, $v=0.3$), a method that does not require further

taken from the software database [81] and stresses are obtained through the $\sin^2\psi$

algorithm. The residual stresses found in the center of the YSZ layers are summarized in

Table 4.4:

Table 4.4 Residual stress values found in the YSZ layers of the fuel cell platforms using the $\sin^2\psi$ algorithm.

Sample ID	σ_{22} (MPa)	σ_{33} (MPa)
Fe45Ni	22 ± 5	-41 ± 2
Fe47.5Ni	4 ± 2	-63 ± 3
Fe50Ni	20 ± 4	-87 ± 1
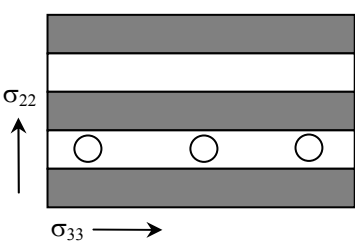
It is seen that the Fe47.5Ni platform yields the lowest σ_{22} stress and the Fe45Ni sample

gives the lowest stress in the σ_{33} direction. The compressive σ_{33} stress grows with

increasing nickel content implying that the expansion mismatch between the alloys and

YSZ is also growing with increased nickel content. Assuming a zero stress temperature

of approximately 600°C, this was found to be the case.

Stresses for a longer Fe47.5Ni sample (4.0 cm) taken at various points along the

length of the YSZ layer are shown in Table 4.5. A stress gradient is seen to exist across

the length of the layer confirming the presence of additional shear stresses, which result

in the psi-splitting in Figure 4.30.

Table 4.5 Residual stress values found in the YSZ layer of a Fe47.5Ni/YSZ fuel cell platform using the $\sin^2\psi$ method.

Relative Distance	σ_{22} [MPa]	σ_{33} [MPa]
0.125	60.6 ± 4.3	-53.6 ± 3.1
0.500	81.6 ± 2.9	-40.8 ± 2.0
0.875	54.1 ± 4.4	-54.9 ± 3.5

4.7 Finite Element Modeling

4.7.1 Modeling Parameters

Materials parameters necessary for finite element modeling are outlined in the following sections. Thermal expansion, various mechanical properties, relative density, and zero stress temperature results obtained both experimentally and from the literature are presented and discussed.

4.7.1.1 Thermal Expansion Behavior

The information from experimental thermal expansion data is paramount to characterizing joined material system. Church has compiled CTE and thermal expansion data for a variety of nickel based alloys and ferritic and austenitic steels considered as metallic interconnects for fuel cells. [14] Data for the individual materials were collected from a pushrod dilatometer. Samples were heated under an inert (argon) atmosphere at a rate of 3°C/minute to a set temperature of 1300°C and furnace cooled. Coefficients of thermal expansion for YSZ and several Fe-Ni binary alloys as determined by Church are plotted as a function of temperature in Figure 4.31.
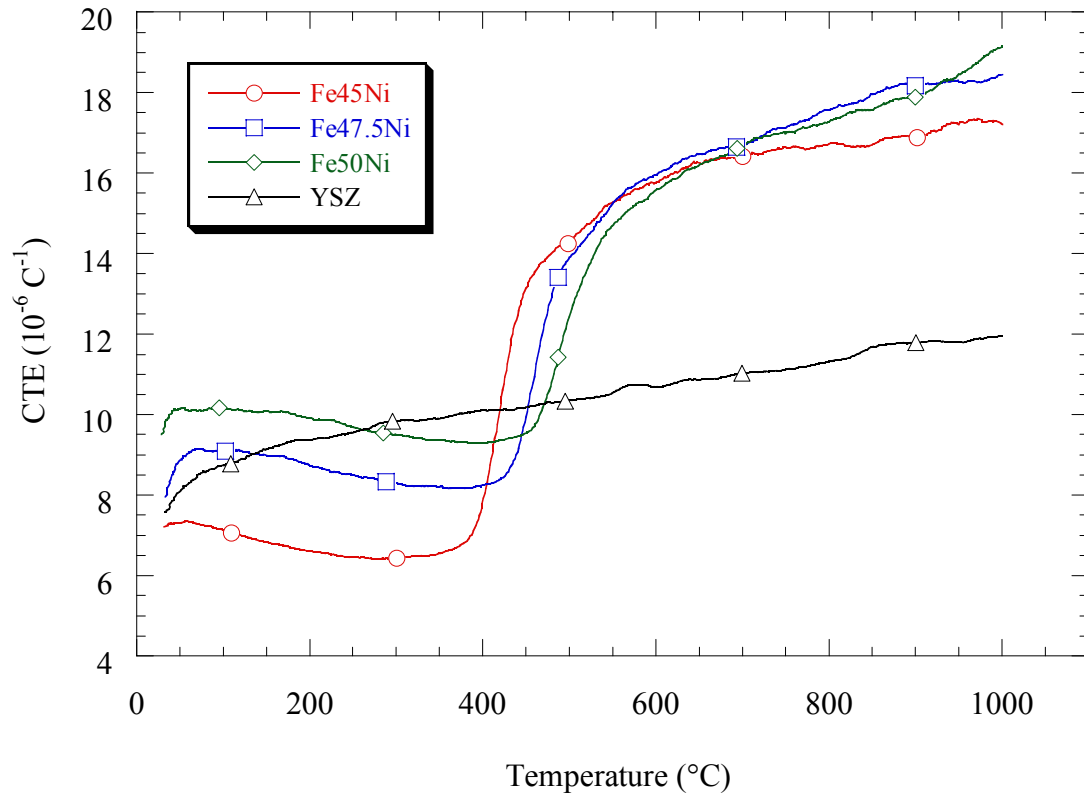
Figure 4.31 CTE for Fe-Ni and YSZ components used in the SOFC platforms. [14]

The average thermal expansion of the YSZ was calculated to be 10.39 x 10^{-6} / K^{-1} from 20 to 1000°C. All three of the iron-nickel compositions (45, 47.5, and 50 Ni) follow similar trends with the CTE initially decreasing until the Curie temperature is reached at which point the CTE increases rapidly. The Curie temperature for the Fe-Ni alloys is also seen to increase with increasing nickel content. The expansion behavior of these binary alloys is thus observed to be composition dependent. While plots of CTE establish and show important trends, residual stresses arise due to differences between linear expansion. Figure 4.32 shows the actual linear expansion curves from which the
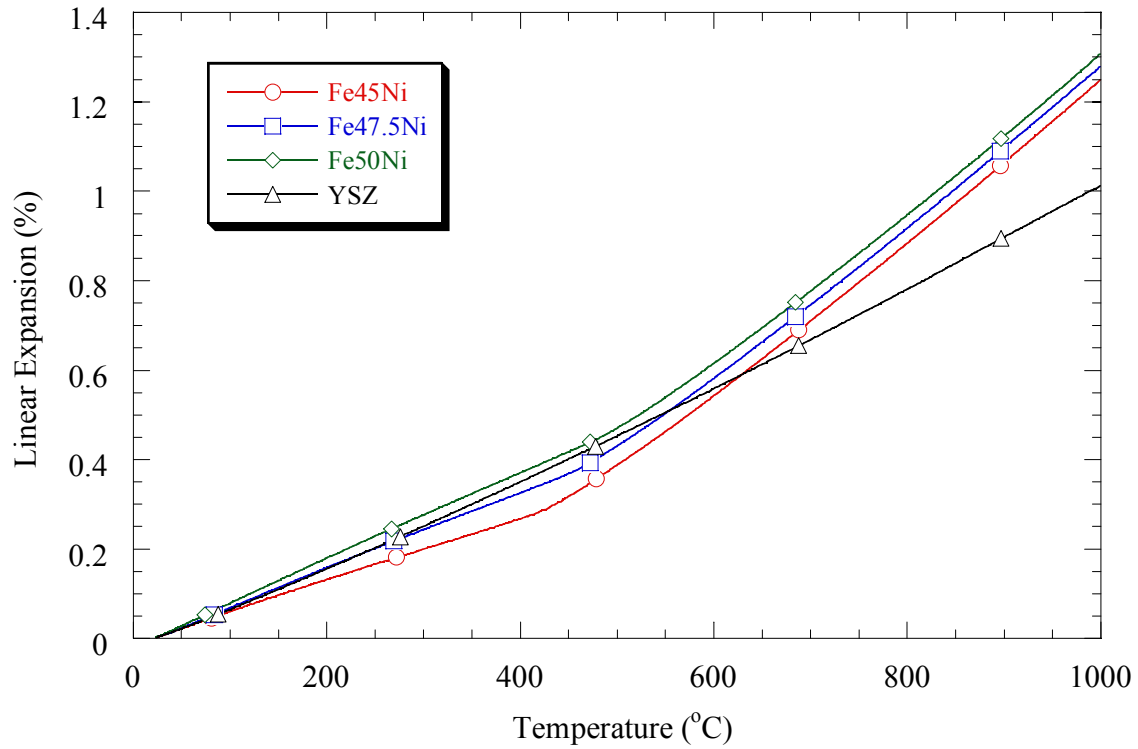
Figure 4.32 Linear expansion of Fe-Ni and YSZ compositions used in the SOFC platforms.

data in Figure 4.31 were derived. While the trends regarding the Curie temperature are not as apparent within these plots it is the difference in these curves that result in the evolution of residual stress. This will be further discussed in Section 4.7.1.4.

4.7.1.2   Density

Density measurements for the alloys are outlined in Table 4.6. Comparing the values in Table 4.6 with those in Table 4.3 shows that the porosity in the platform alloys is greater than those found in the lone interconnect accentuating the effects of constrained sintering. Porosity within the samples appears to decrease slightly with increasing nickel content. This is possibly due to catalytic effects that nickel plays in the reduction process. Regardless, the densities for the metal should provide a good compromise between

hermeticity and porosity knockdown of mechanical properties, which would better equip the metal to aid in the accommodation of stresses.

Table 4.6 Density values for fuel cell components as determined by Archimedes measurements. Theoretical values calculated from rule of mixtures.

Sample Composition	$\rho_{experimental}$ (g/cm^3)	$\rho_{theoretical}$ (g/cm^3)	Theoretical Density (%)
Fe45Ni (1)	7.486	8.302	90.18 %
Fe45Ni (2)	7.499	8.302	90.33 %
Fe47.5Ni (1)	7.543	8.328	90.57 %
Fe47.5Ni (2)	7.580	8.328	91.02 %
Fe50Ni (1)	7.599	8.353	90.97 %
Fe50Ni (2)	7.631	8.353	91.36 %
Ni	8.714	8.910	97.80 %
YSZ	5.908	6.050	97.65 %

4.7.1.3   M

echanical properties

Mechanical properties (Young's modulus, Poisson's ratio) for YSZ are outlined in Table 4.7 and were obtained from the literature. [1] Softening effects from temperature increase are also included. Mechanical properties [Young's modulus (E), Poisson's ratio (ν), Shear modulus (μ), Bulk modulus (B) and Lame's constant (λ)] obtained from wave speed measurements for relevant FeNi compositions as well as a nickel standard are summarized in Table 4.8.   The general trends observable from this table indicate an increase in values as the nickel content increases.   Of particular interest for coding is the Young's modulus of the materials.   The last column in Table 4.8 estimates the moduli for fully dense compositions using Equation 2.5.14.

Figure 4.33 compares the experimental values with those found from several sources in the literature. From the literature data it is seen that a rule of mixtures for the modulus is not observed. Instead, the moduli decreases from that of iron as the invar composition (~Fe36Ni) is approached and then increases to a value of ~210-230 GPa for pure nickel.

The trend is similar to that observed for coefficient of thermal expansion and other thermodynamic values. [25] Around the invar composition, the energy difference between the non-magenetic low spin state and magnetic high spin state grows low enough to promote the transition between the two resulting in magnetovolume effects such as an increase in lattice parameter and subsequent decline in modulus due to the diminished bond strength. So these results are unsurprising in light of the intimate relationship that both modulus and CTE values have with atomic bond strength. This trend is of interest however as weaker materials could serve to accommodate stresses by

Table 4.7 Mechanical property data for YSZ illustrating the softening effects of temperature. [1]

Temperature (°C)	Elastic Modulus (GPa)	Poisson's Ratio
25	190	0.308
100	187	0.309
300	178	0.310
500	170	0.311
600	166	0.312
700	161	0.312
800	157	0.313
1000	148	0.314

Table 4.8 Mechanical property data for various FeNi alloys obtained from wave speed measurements.

Sample	λ [GPa]	E [GPa]	μ [GPa]	B [GPa]	ν	%TD	E_{dense}
Fe45Ni 1	61.693	117.473	45.623	92.108	0.287	90.180	166.815
Fe45Ni 2	65.934	118.135	45.591	96.328	0.296	90.330	166.811
Fe47.5Ni 1	92.114	123.942	46.517	123.126	0.332	90.570	173.432
Fe47.5Ni 2	86.913	130.093	49.315	119.789	0.319	91.020	178.996
Fe50Ni 1	60.202	130.951	51.585	94.592	0.269	90.970	180.590
Fe50Ni 2	89.363	136.083	51.671	123.811	0.317	91.360	184.959
Ni	209.926	191.938	69.782	256.448	0.375	97.800	208.151
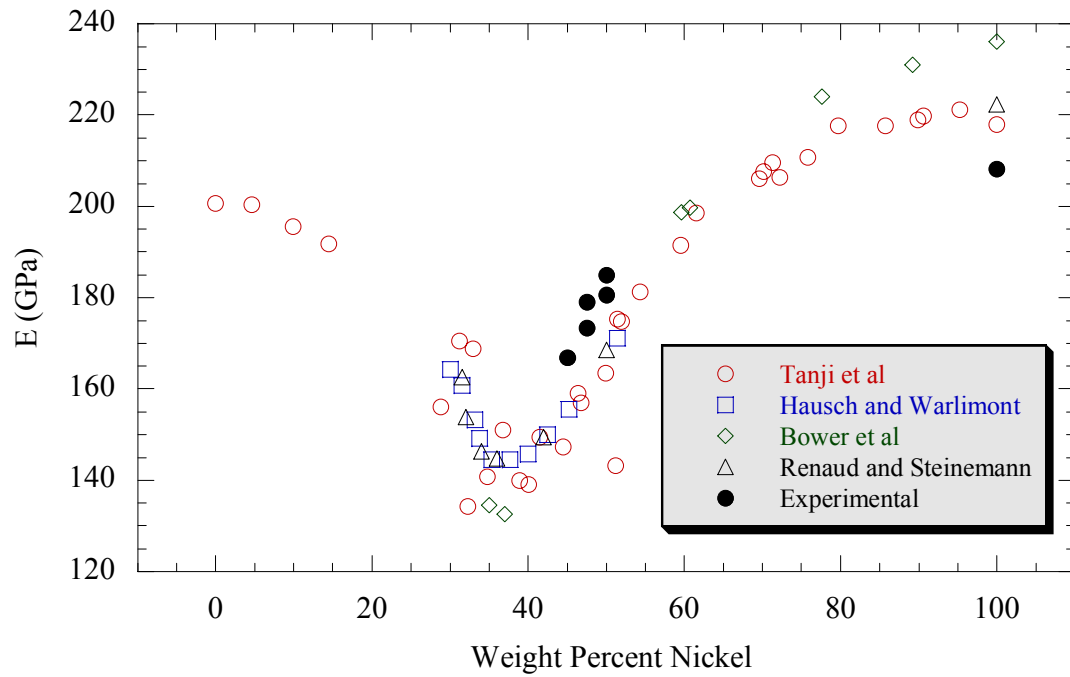
Figure 4.33 Comparison of experimental and literature values [82-85] of Young's modulus in FeNi binary alloys as a function of nickel content. The values follow a similar trend for CTE in that a minimal value is observed around the invar (Fe36Ni) composition.
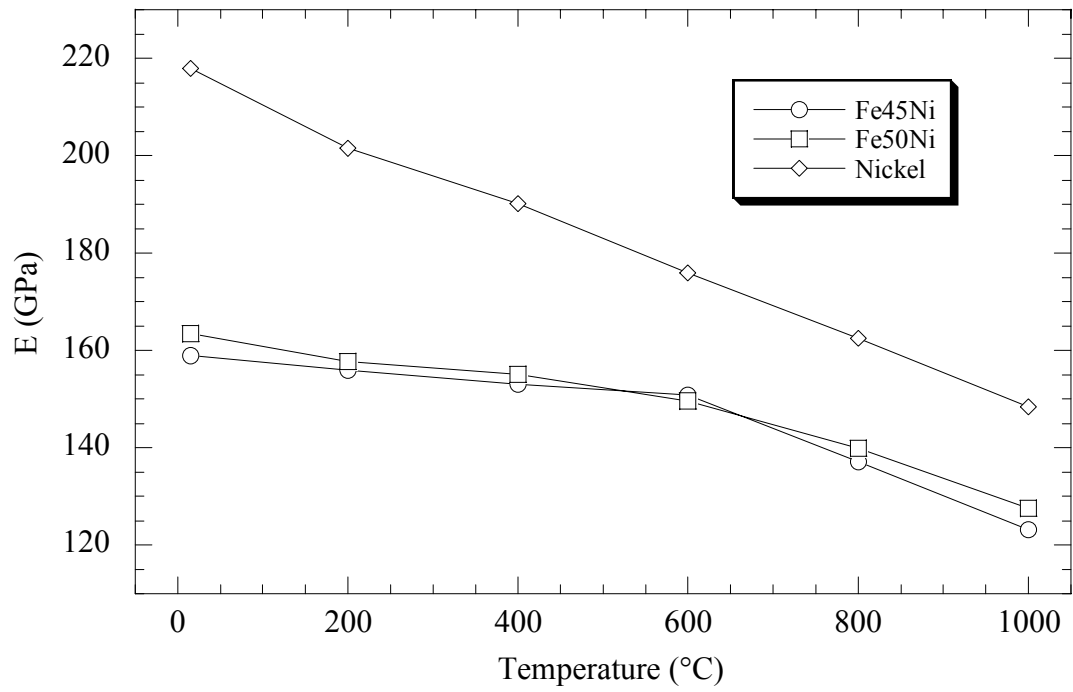
Figure 4.34 Elastic modulus as a function of temperature for various Fe-Ni samples illustrating softening effects in the metal, after [82].
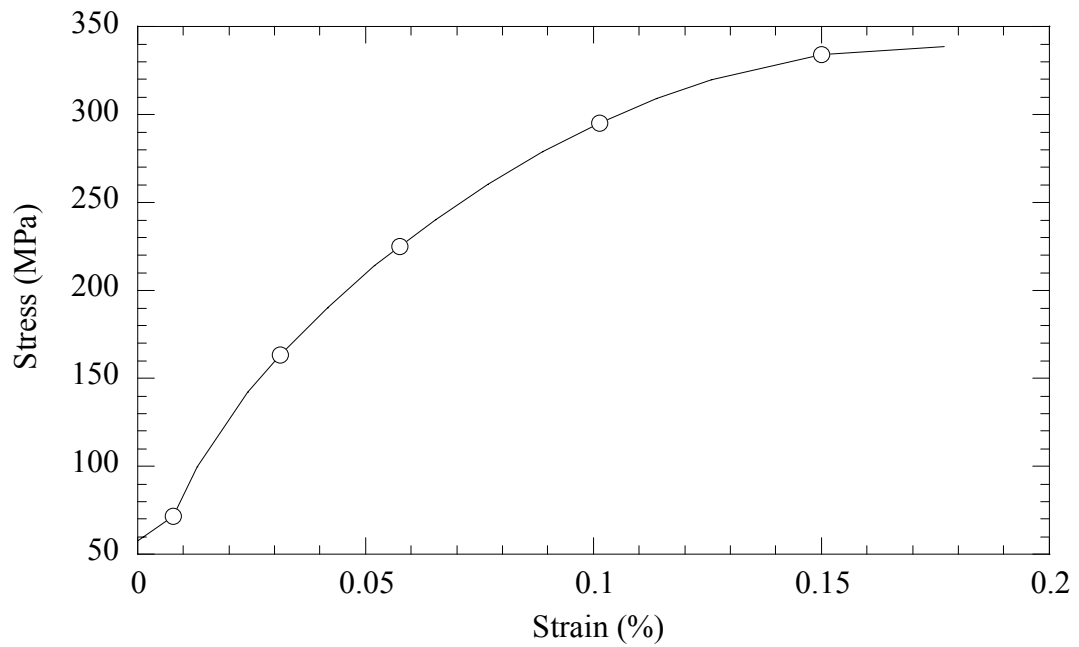
Figure 4.35 Fe50Ni stress-strain curve used to model plasticity effects for Fe-Ni alloys in FEM simulations, after [14].

yielding or plastically deforming.

The influence of temperature on elastic moduli for the Fe-Ni alloys was estimated from data found in the literature. Figure 4.34, from data taken from Tanji *et. al.* [82]illustrates the softening effects of several Fe-Ni based metals. Plasticity of the Fe-Ni alloys was estimated by a stress strain curve for Fe50Ni found from the literature. [14] (Figure 4.35) The influence of compositional differences upon the plastic effects was assumed negligible and this data was used for all three Fe-Ni compositions.

4.7.1.4   Zero Stress Temperature

Figure 4.36 is a plot of room temperature residual stress within the YSZ layer as a function of possible zero stress temperatures as calculated from section 3.9.1. The experimental residual stress values from XRD measurements are plotted as well. The temperature range of 500-700°C was chosen because of the likelihood that the zero stress temperature would lie within this span. The effects of the thermal expansion differences for different Fe-Ni alloys upon residual stress become apparent within this graph. Trends indicate that an increase in nickel content results in an increasingly compressive residual stress. The importance of establishing the zero stress temperature becomes evident as the residual stress in the ceramic layer of the platform can vary ~125 MPa over a zero stress temperature range of 200°C.

The point where these calculated curves coincide with the experimental XRD residual stress values should be the actual residual stress temperature. The zero stress temperatures of the FeNi/YSZ systems obtained from this procedure are summarized in Table 4.9.
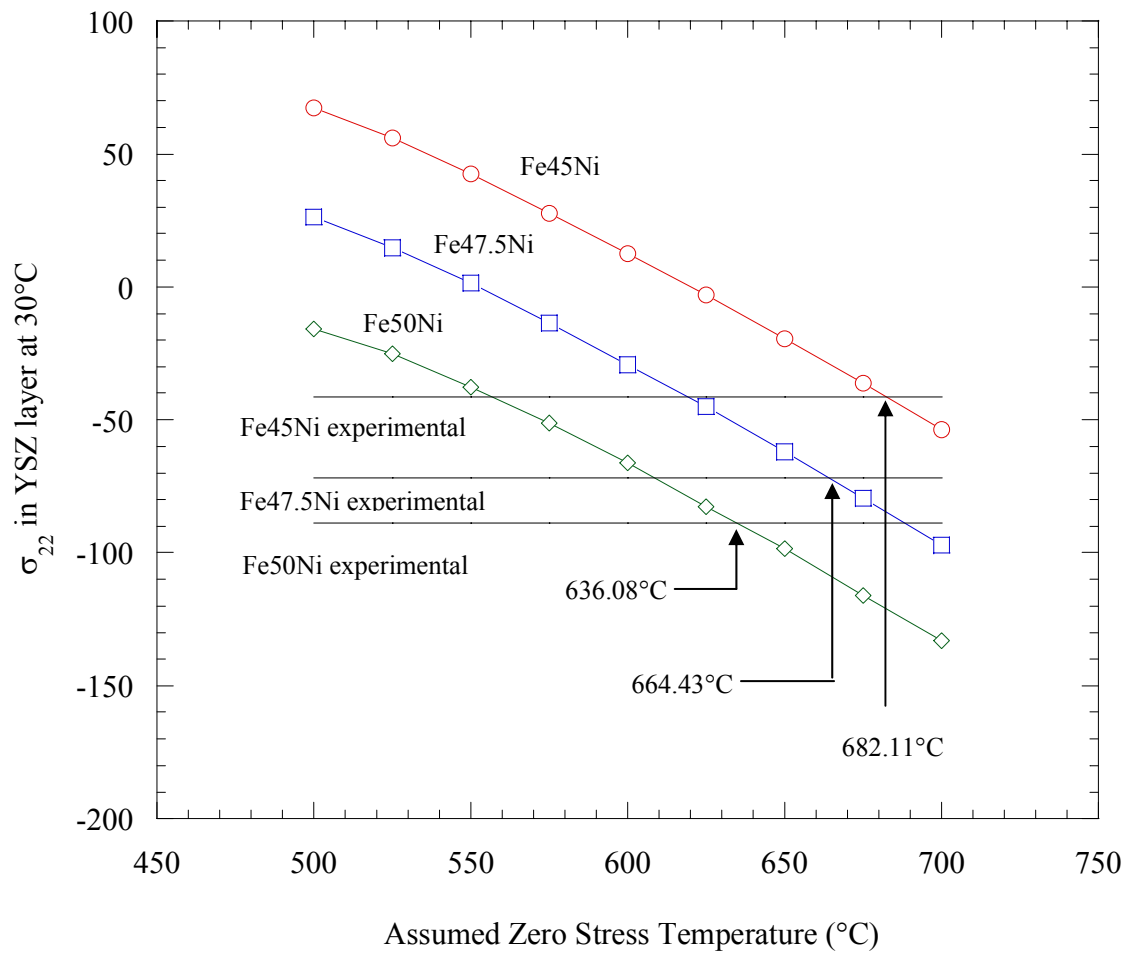
Figure 4.36 Graph of calculated room temperature residual stress in the YSZ layers as a function of zero stress temperature. Comparing experimental values (black lines) with calculated values, the actual zero stress temperature can be extrapolated.

Table 4.9 Zero stress temperatures for Fe-Ni/YSZ couples determined as a function of composition.

Interconnect Alloy Composition (wt%)	Zero Stress Temperature (°C)
Fe45Ni	682.11
Fe47.5Ni	664.43
Fe50Ni	636.08

Figure 4.37 demonstrates a trend in zero stress temperature. It is seen that the zero stress temperature increases with decreasing nickel content in the alloys, implying a rule o9f mixtures effect. The melting temperature of iron and nickel are 1538°C and 1455°C respectively. Figure 4.37 also compares the experimentally derived zero stress temperatures with the melting temperature of each alloy extrapolated from the Fe-Ni phase diagram. The melting temperature also follows a rule of mixtures type behavior and could possibly serve in establishing the zero stress temperature by serving as a basis for establishing creep temperature, a possible influence behind the zero stress temperature.

Both curves follow similar trends as a function of composition. The ratio of zero stress temperature to melting temperature also follows a similar trend and is ~44% for Fe50Ni and ~47% for Fe45Ni. This ratio would be expected to be constant in following with a rule of mixtures theory. One possible explanation for this observation could lie with the results in Table 4.6. It is seen that the average porosity in these alloys increases with decreasing nickel content. The increased porosity could serve as barriers to recrystallization or other diffusion based annealing mechanisms and thus necessitate higher temperatures.
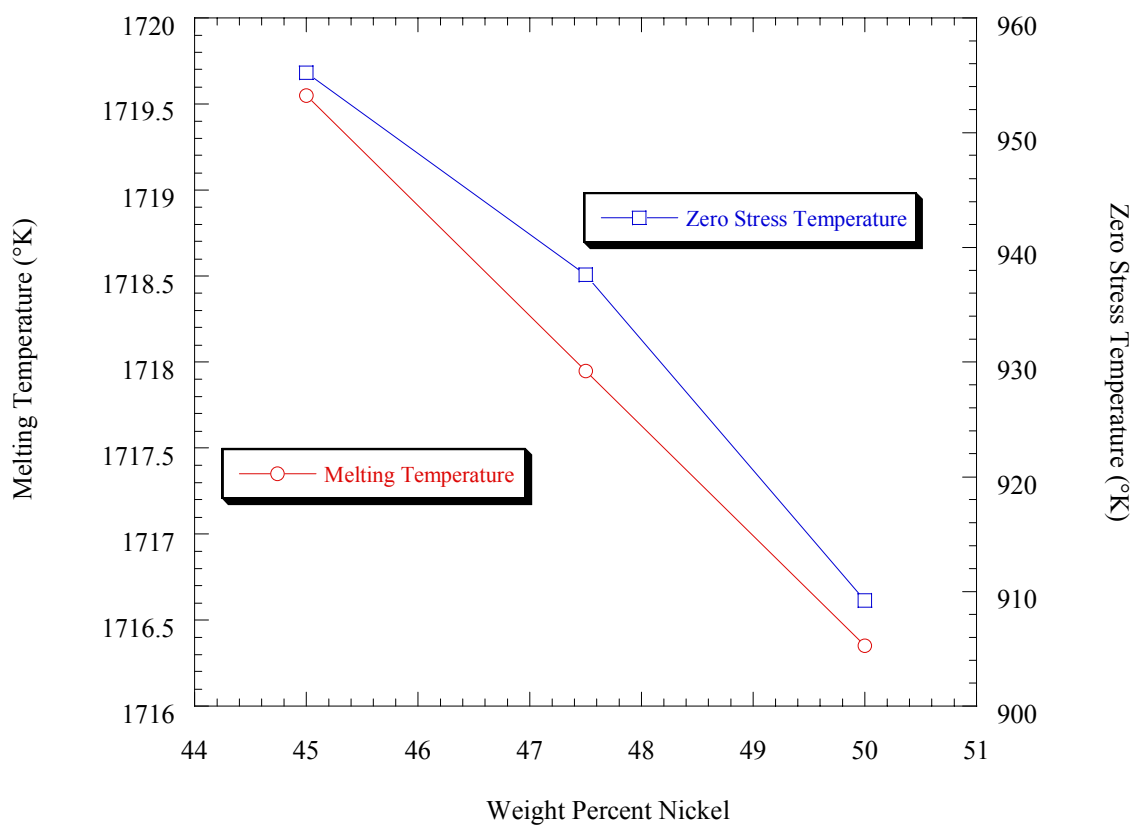
Figure 4.37 Zero stress temperature and melting temperature comparison for the FeNi alloys used in this study.

4.8 FEM Results

The ABAQUS software allows for various components of the stress tensor to be pictorially plotted on the sample geometry. (Figure 4.38 and Figure 4.39) Figure 4.38 outlines the distribution of σ_{33} stresses throughout the YSZ/Fe45Ni fuel cell platform and Figure 4.39 plots the σ_{22} stresses within the same platform. As expected, the stresses in the σ_{33} direction tend to be tensile within the metallic layers and compressive in the ceramic layers. On the outside walls, peak stress values appear to exist in regions adjacent to the interface, with values being greatest in the center and dropping off as the end is approached. This is apparent from the top of the platform as seen in Figure 4.38B. The tensile/compressive stress couple is more apparent in the inner walls of the platform (Figure 4.38D) with the peak values occurring in areas adjacent to or within the horizontal walls. Stress values were seen to vary from extremes of -203.9 MPa to $+133.8$ MPa.

Stress values for σ_{22} also exhibit a particular distribution within each layer. Stress values are observed to be tensile within the ceramic layer and compressive in the interconnect layer. Peak tensile values in the ceramic occur on the outside walls within the middle of the layer and at the ends of the layer, both within the middle and at the edge of the interface. Values for σ_{22} are seen to vary from -308.4 MPa to +397.1 MPa.

Stress tensors were compiled in a report file for all the elements comprising each platform. From these files, a distribution of a particular stress tensor at various points of the platform could be established. Stress tensors are taken from elements comprising
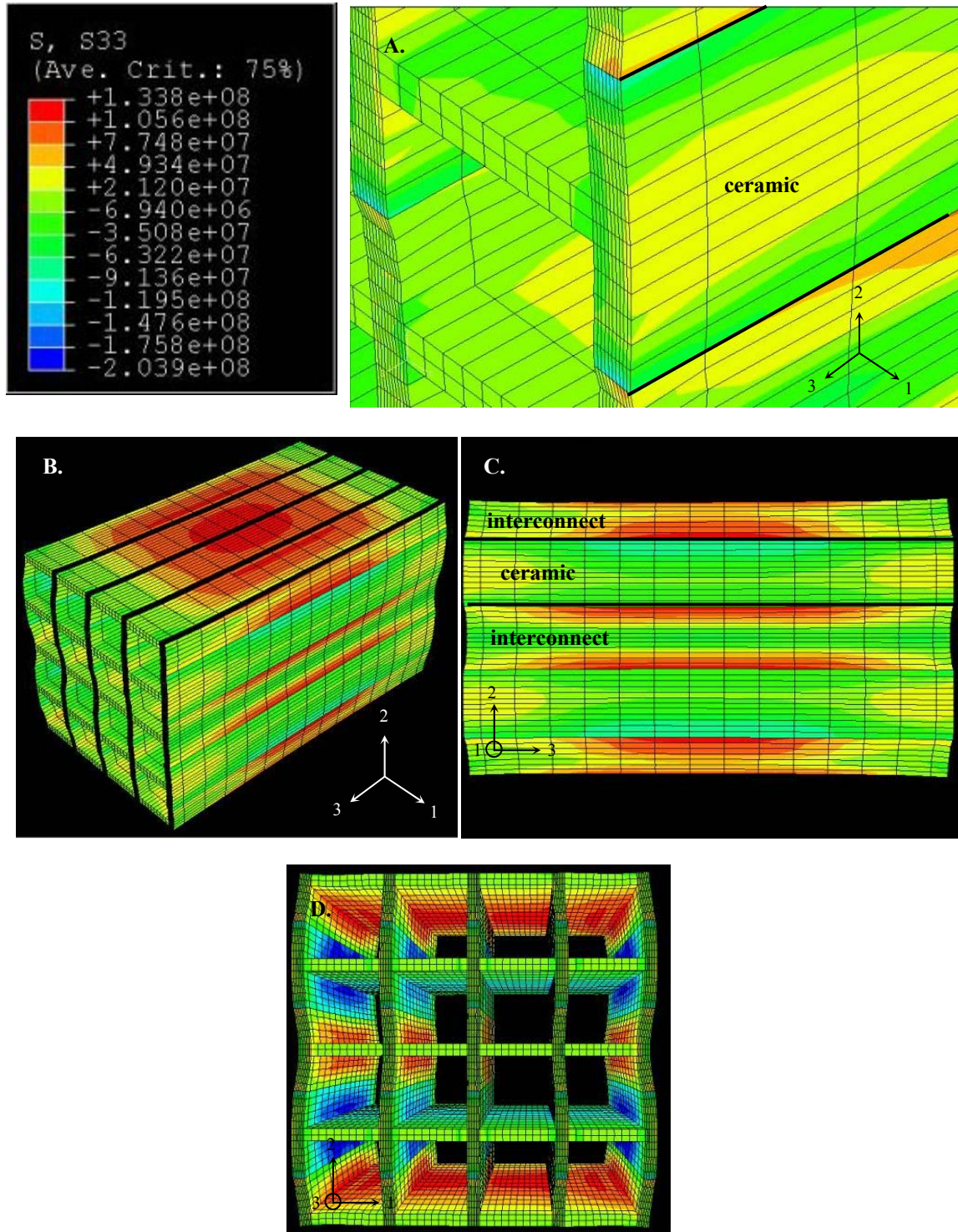
Figure 4.38 FEM results for σ_{33} profile in Fe45Ni/YSZ sample. A.) Close up view of σ_{33} stress distribution in ceramic layer. B.) σ_{33} distribution in whole platform. C.) Side view of σ_{33} distribution in the platform. D.) Cross sectional view of σ_{33} distribution within the entire platform.
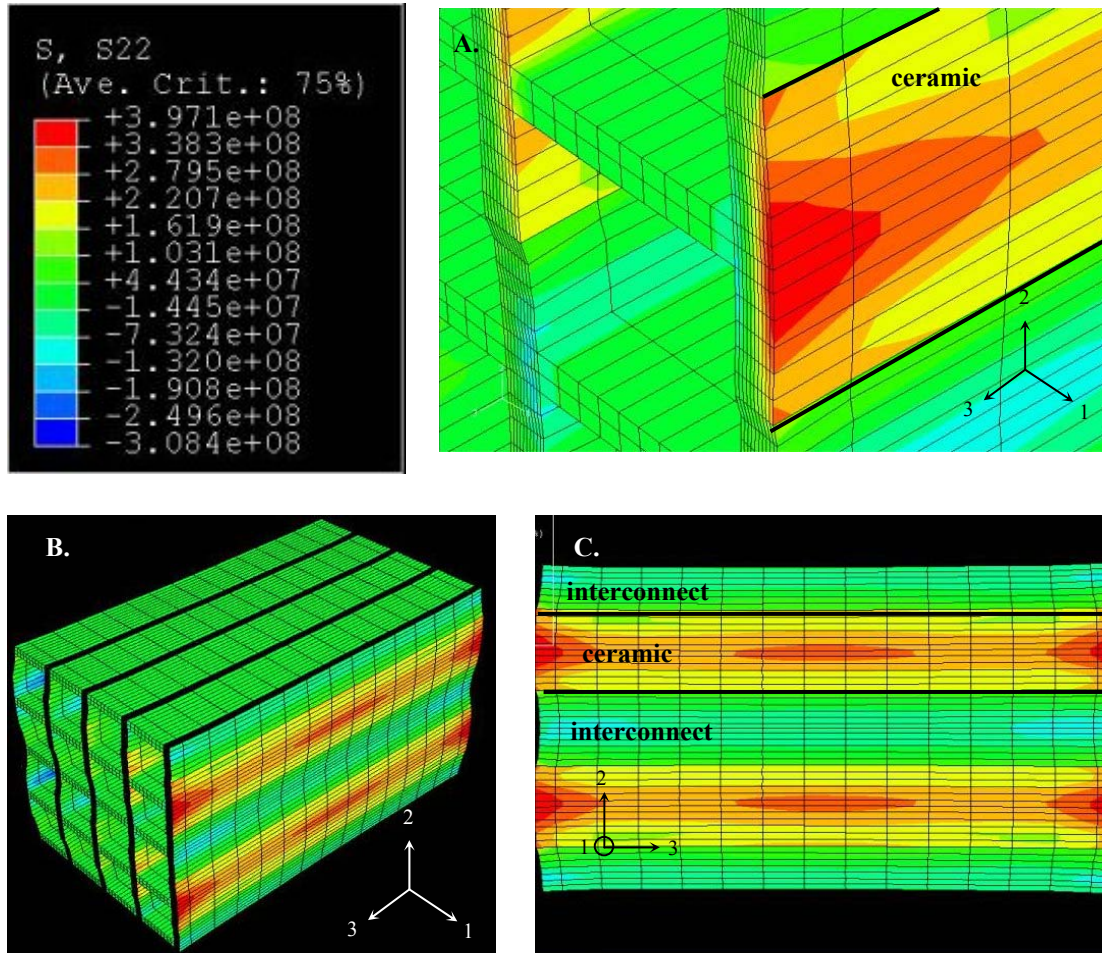
Figure 4.39 FEM results for σ_{22} profile in Fe45Ni/YSZ sample. A.) Close up view of σ_{22} stress distribution in ceramic layer. B.) σ_{22} distribution in whole platform. C.) Side view of σ_{22} distribution in the platform.

the region through the middle of the ceramic layer along the outermost walls. This region corresponded to those characterized by x-ray diffraction. By changing certain elements of the coding, the discretization of the wall elements could be adjusted so that the stress along the wall could be obtained at various depths.

Figure 4.40 shows the σ_{22} values along the length of the platform from the middle of a ceramic layer. The different curves represent stress values at various depths going further into the YSZ wall. Figure 4.41 plots the corresponding σ_{33} values. The experimental values taken from the exact middle of the layer are also plotted along with these curves. Experimental values for σ_{22} matched well with stress values deeper within the wall. This is explained by the fact that x-rays do not measure superficial aspects of a sample, but penetrate a certain depth within the sample. Penetration depth of the x-ray is dependent upon the sample, x-ray source, and diffraction angle and is quantified by [74]:

$$x = \frac{K_x \sin \theta}{2\mu} \qquad (4.7.1)$$

where x is the penetration depth, μ is the mass absorption coefficient (which is composition dependent), θ is the diffraction angle and G_x is the fraction of the total diffracted intensity. Assuming a range of zirconia densities and diffraction intensites gives a range of penetration depth of ~20-40 μm. This range matches well for the experimental XRD σ_{33} value; however, the expected σ_{22} stress lies at a depth ~100 μm below the surface.
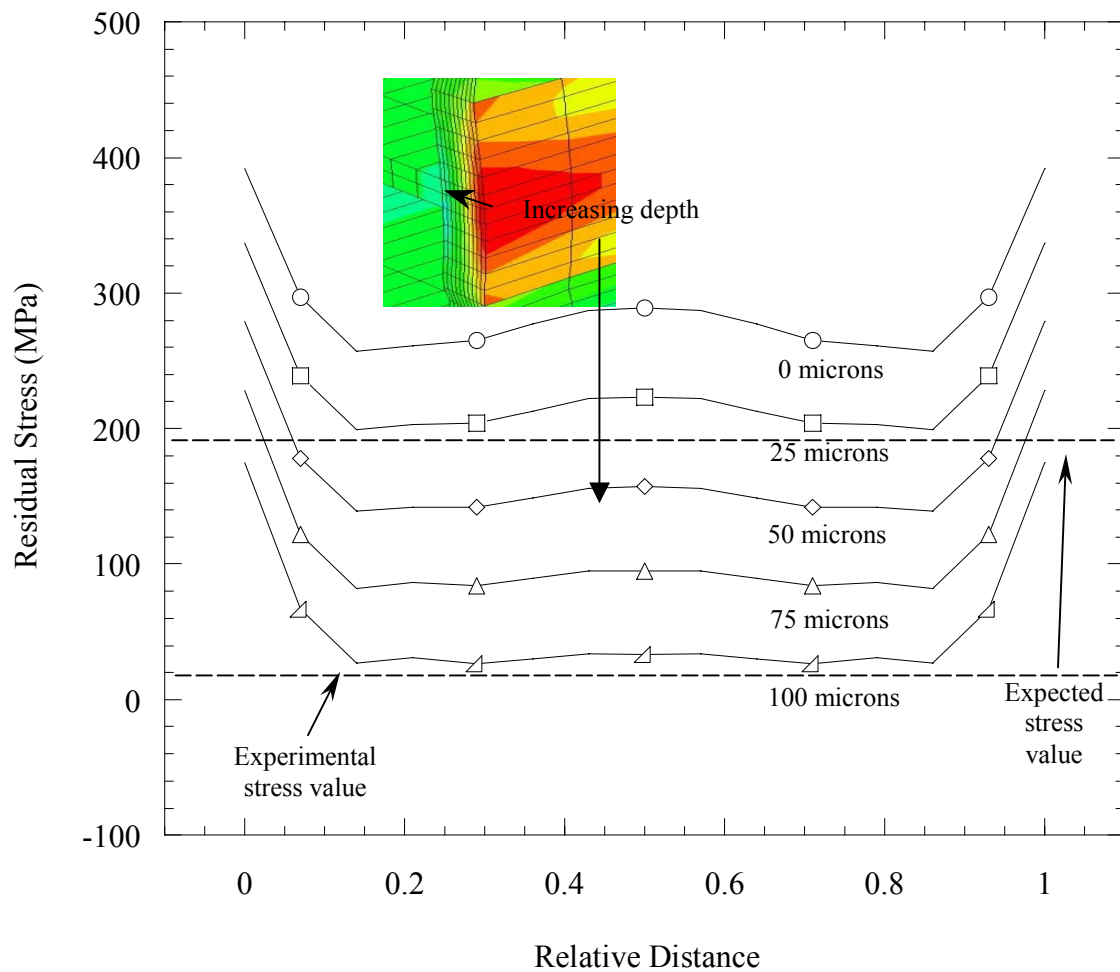
Figure 4.40 σ_{22} **residual stress distribution in the middle of the ceramic layer of the FEM Fe45Ni/YSZ fuel cell platform as a function of wall depth. The XRD experimental value from the middle of the layer is also included.**
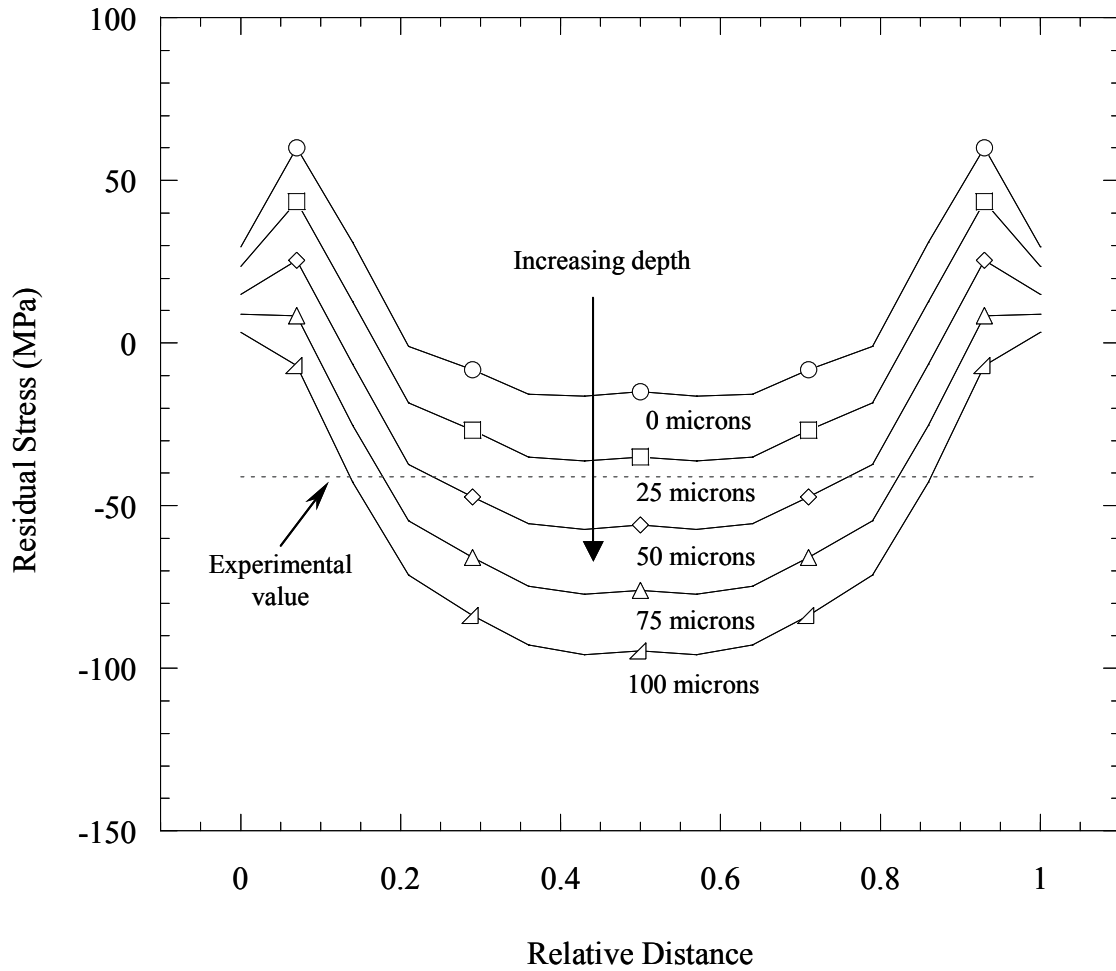
Figure 4.41 σ_{33} residual stress distribution in the middle of the ceramic layer of the FEM Fe45Ni/YSZ fuel cell platform as a function of wall depth. The XRD experimental value from the middle of the layer is also included.

The residual stress value expected at the x-ray penetration depth of 20-40 μm is ~200 MPa. Stress values grow even larger as the surface is approached. The tensile strength of fully dense YSZ is 245 MPa [86] so the material is expected to fail. The reduced stress observed is indicative of the deduction that the stress has been relieved in that direction due to crack formation. Figure 4.42 is a micrograph of the electrolyte portion of the fuel cell platform. Microcracks were found in the ceramic layer parallel
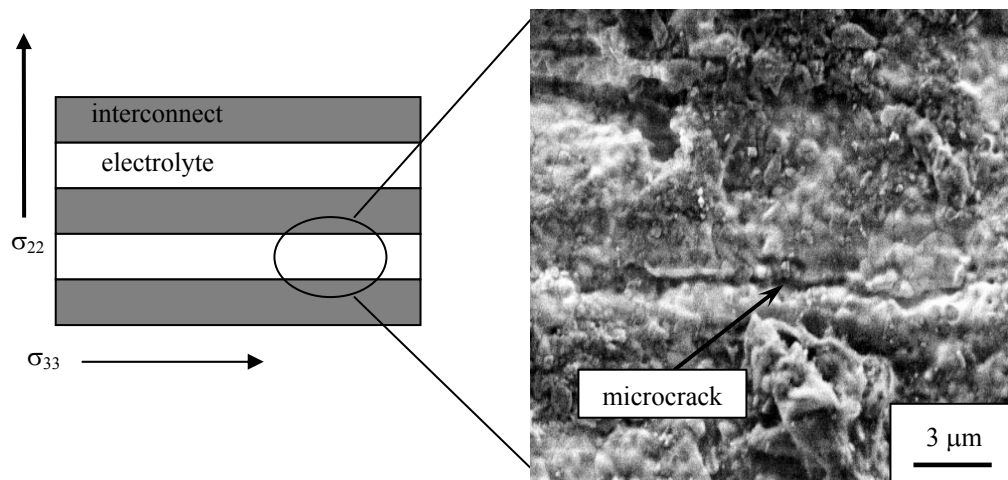
Figure 4.42 Micrograph of the electrolyte portion of Fe-Ni/YSZ fuel cell platform illustrating the presence of microcracks within the microstructure.

to the extrusion direction. Cracking in this direction would not be expected to effect σ_{33} stress values since these arise due to the interfacial shear stresses (and the interface remains unaffected) but would relieve and diminish σ_{22} values. Other possible stress relieving mechanisms could include any remnant porosity present in either phase, or debonding of the interface.

Table 4.10 Finite element stress tensors in the YSZ layers of the various fuel cell platforms corresponding to those areas measured from x-ray diffraction. Values were obtained from elements at a depth 25 microns into the platform.

Sample ID	σ_{11} [MPa]	σ_{22} [MPa]	σ_{33} [MPa]	σ_{12} [MPa]	σ_{13} [MPa]	σ_{23} [MPa]
Fe45Ni	3.76	222.00	-36.20	2.53	0.60	-9.59
Fe47.5Ni	3.77	238.00	-60.70	3.00	0.69	-10.40
Fe50Ni	3.10	221.00	-86.10	3.15	0.71	-9.80
*Fe45Ni**	-	22 ± 5	-41 ± 2	-	-	-
*Fe47.5Ni**	-	4 ± 2	-63 ± 3	-	-	-
*Fe50Ni**	-	20 ± 4	-87 ± 1	-	-	-

(*) For the sake of comparison, the experimental residual stress values are included as well.

Table 4.10 summarizes the modeled stress tensors in the ceramic layers of the various fuel cell platforms taken from elements corresponding to the areas where x-ray diffraction stress values were obtained. It should be noted that the shear stress tensors are relatively small in comparison with the primary stress values and so the biaxial stress state assumed for the $\sin^2\psi$ can be considered valid. For comparison's sake the data from x-ray diffraction measurements are included as well. The σ_{33} values for each fuel cell platform are in fair agreement with the FEM values however the σ_{22} values are unequal, presumably due to the microcracking discussed above. Again, these stress values that the model predicts are within the range of the tensile strength of YSZ so they are not unreasonable.

The agreement of the stress values obtained by XRD strain analysis and through finite element calculations demonstrates the validity of the model. In particular, this corroborates the zero stress temperature theory expounded on previously.

5   Conclusions

It was previously shown that co-extrusions of a hybrid electrolyte/interconnect fuel cell platform could be produced from oxide/metal powder precursors. Processing issues arise during the subsequent reduction/co-sintering of the layers and residual stress development in the platform during cooldown. Co-extrusions comprised of a YSZ electrolyte paired with several binary Fe-Ni compositions (Fe45Ni, Fe47.5Ni, Fe50Ni) were fabricated and fired.

Sintering curves were obtained for the alloy and electrolyte as well as precursors of the alloy.   SEM and XRD techniques were used to further characterize reduction/sintering of the alloy. The use of metallic powders rather than manipulation of solids loading was observed to be more effective at altering overall shrinkage. Alloy sintering was seen to occur in two stages. Shrinkage initially occurred at ~350°C as magnetite reduced and necks initially formed between particles. Rates leveled off at ~600°C and densification proceeded once more at 800°C as densification and grain growth round out the microstructural evolution of the alloy. Interdiffusion of the reduced iron and nickel particles did not occur until temperatures coinciding with the densification of the compact. XRD results indicated that iron diffused into nickel to form the final solid solution.

Sintering curves for the yttria-stabilized zirconia demonstrated that densification does not begin until ~1000°C. A Fe_3O_4-Ni compact fired under a non-reducing atmosphere was seen to begin sintering at ~825°C. It would thus appear that this system is resigned to a constrained sintering situation and porosity within the interconnect is

inevitable. Optical micrographs of the interconnect cross section indicate a substantial amount of porosity, however the hermeticity of the layer remains uncompromised.

XRD residual stress measurements could not be conducted within the metallic interconnect because of excessive grain growth. Stresses in the zirconia layer were observed to vary as a function of interconnect composition implying that thermal expansion manipulation could control the resultant residual stress. The Fe45Ni interconnect was observed to produce the lowest degree of residual stress within the electrolyte.

The temperature where residual stresses evolve, or the zero stress temperature was a key parameter for modeling. An analytical method to calculate the zero stress temperature based on room temperature XRD stress analysis and differential expansion stress calculations as a function of temperature was presented. The zero stress temperatures for the three platforms were found to lie in a range of 630-680°C, which is consistent with the values proposed by Eisele [63]. Zero stress temperatures were seen to increase with increasing nickel content suggesting that a rule of mixtures effect may be in play.

The melting temperature of the alloys were also seen to have a compositional dependence and was believed to also play a role in determining the zero stress temperature by establishing temperatures at which creep occurs. Young's modulus was also observed to vary with composition with a trend similar to the invar behavior. The manipulation of modulus as a function of composition could also serve as a method for relieving stresses through diminished mechanical properties.

Finite element modeling demonstrated residual stress distributions corresponding to those expected from theory. Stresses parallel to the layers (σ_{33}) were found to be greatest at the material interface and diminish as the end of the layer is approached. Stresses perpendicular to the extrusion direction (σ_{22}), which is of more concern to the ceramic electrolyte increases as the edges of the layer draw near. Theoretical and experimental values were found to correlate well in the σ_{33} direction. Experimental values in the σ_{22} direction however were found to be substantially lower than those predicted by the model. Finite element stress values predicted for this direction are in the vicinity of the tensile strength for yttria-stabilized zirconia. Further analysis found small microcracks in the electrolyte that relieved the stresses in this direction, but left the stresses in the σ_{33} direction untouched. The good agreement between experimental and model stress values also serves as indirect confirmation of the zero stress temperature calculations.

6   Recommendations for Future Work

The Fe-Ni/YSZ materials system was chosen because of thermal expansion considerations.   Further sintering and residual stress studies of material systems incorporating other desired properties of the interconnect such as oxidation resistance could establish limitations and trade-offs between desired properties.

Further systematic co-sintering studies would also be useful. It is well known that densification curves can be manipulated by a variety of parameters including particle size distribution, heating rates, and green packing densities. The effects of different particle morphologies or oxide types on sintering could also be a potential area of additional research.

Zero stress temperatures were found for systems over a small compositional range. This data suggested that a rule of mixtures/melting temperature effect might exist. Experiments over a larger range could provide additional insight into compositional influence on zero stress temperature. Additional high temperature mechanical tests on samples with similar compositions could also serve to corroborate zero stress temperature calculations and give further insight into the types of diffusional mechanisms for stress relaxation.

The materials data and finite element modeling could be employed to investigate and develop additional platform geometries that could result in a lower degree of constrained sintering and/or residual stress. Possible geometries that could potentially lower thermal stresses include single hybrid cellular layers and single monolithic layers with outer coatings of additional materials.

A. Appendix
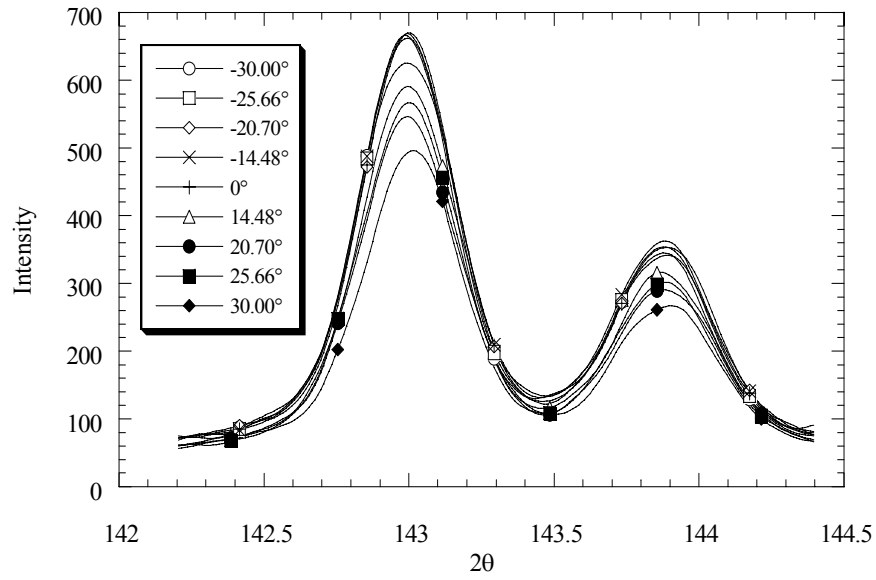
Figure A.1 Smoothed XRD peaks (YSZ, (620)) measured as a function of ψ angle in the (s22) direction on the YSZ/Fe47.5Ni platform.
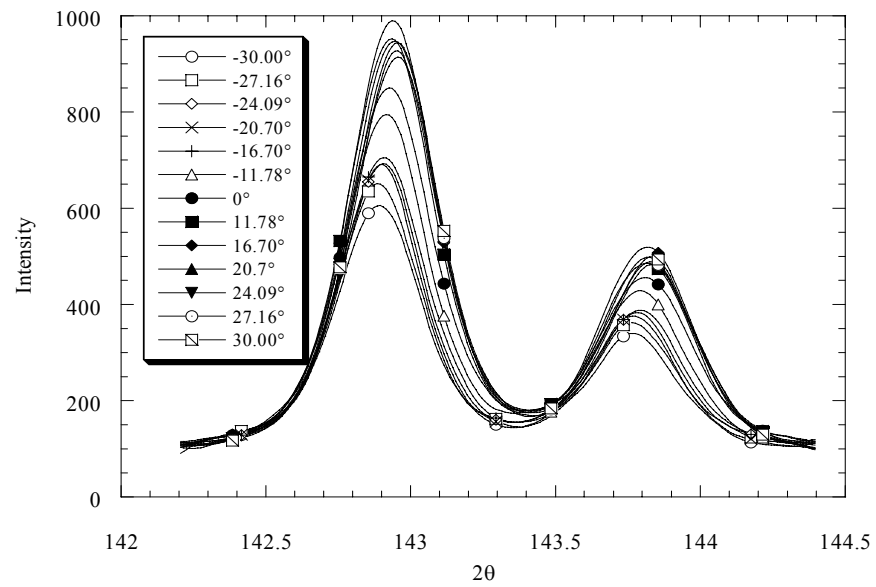
Figure A.2 Smoothed XRD peaks (YSZ, (620)) measured as a function of ψ angle in the (σ$_{22}$) direction on the YSZ/Fe50Ni platform.
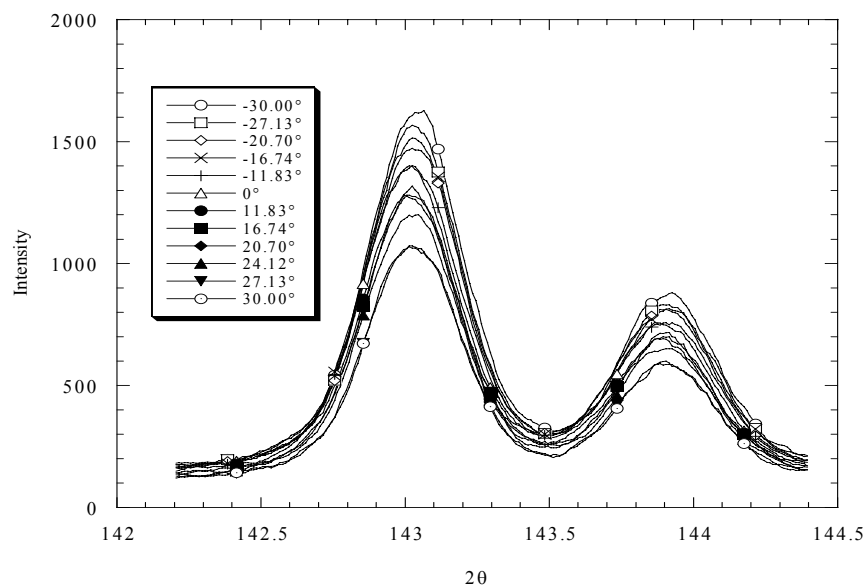
Figure A.3 Smoothed XRD peaks (YSZ, (620)) measured as a function of ψ angle in the (σ_{33}) direction on the YSZ/Fe45Ni platform.
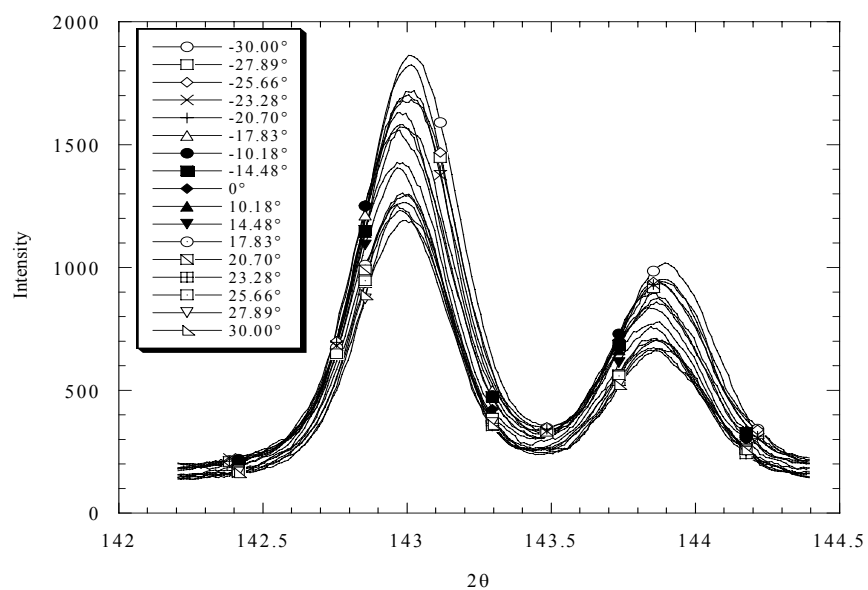
Figure A.4 Smoothed XRD peaks (YSZ, (620)) measured as a function of ψ angle in the (σ_{33}) direction on the YSZ/Fe47.5Ni platform.
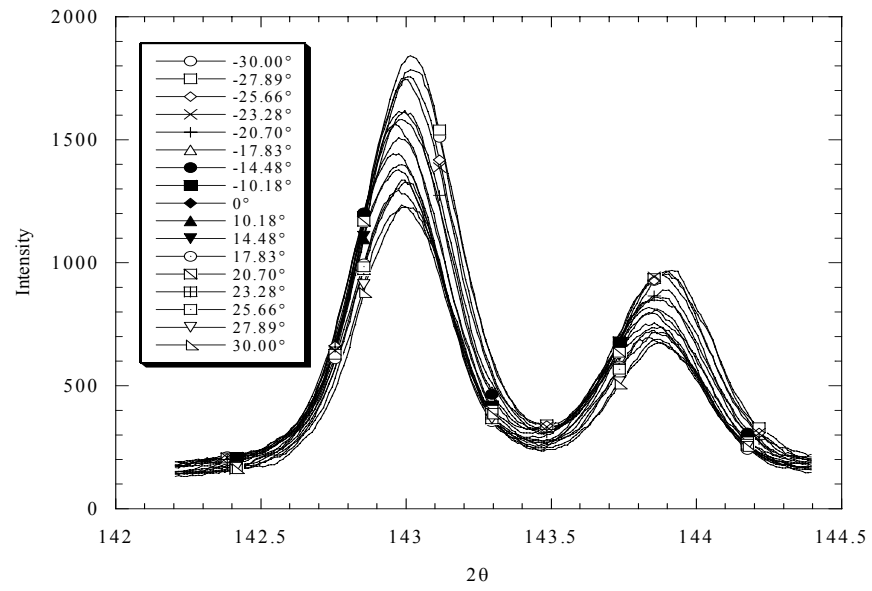
Figure A.5 Smoothed XRD peaks (YSZ, (620)) measured as a function of ψ angle in the (σ_{33}) direction on the YSZ/Fe50Ni platform.
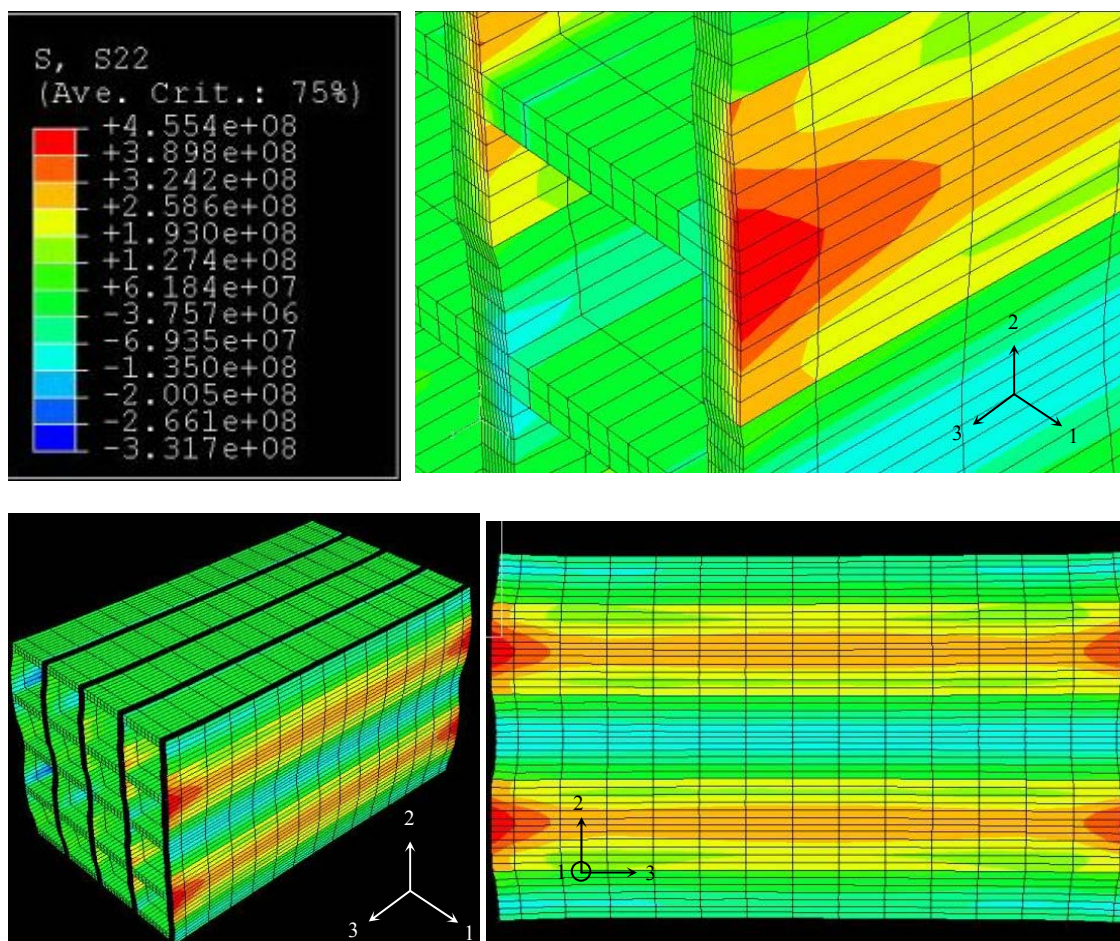
Figure A.6 Finite element results for the σ_{22} stress distribution in the Fe47.5Ni/YSZ platform.
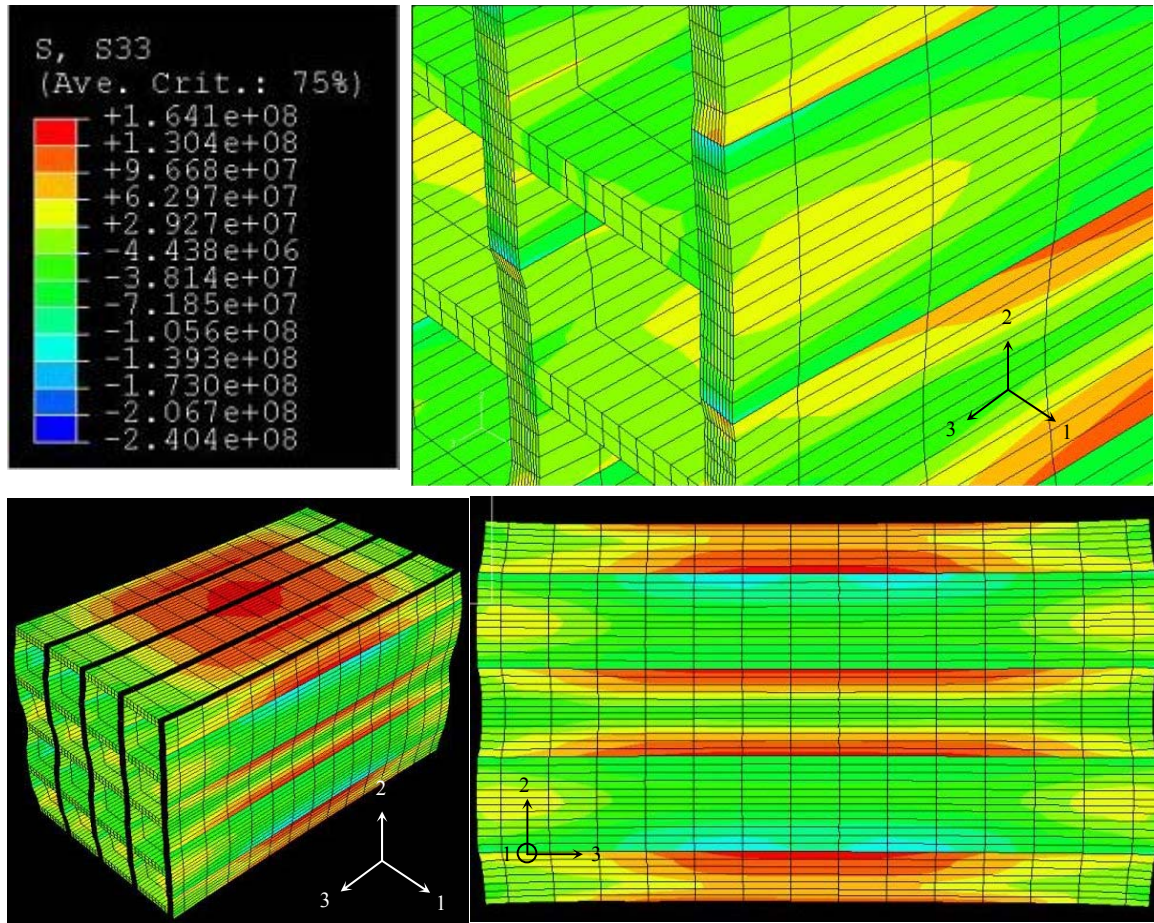
Figure A.7 Finite element results for the σ_{33} stress distribution in the Fe47.5Ni/YSZ platform.
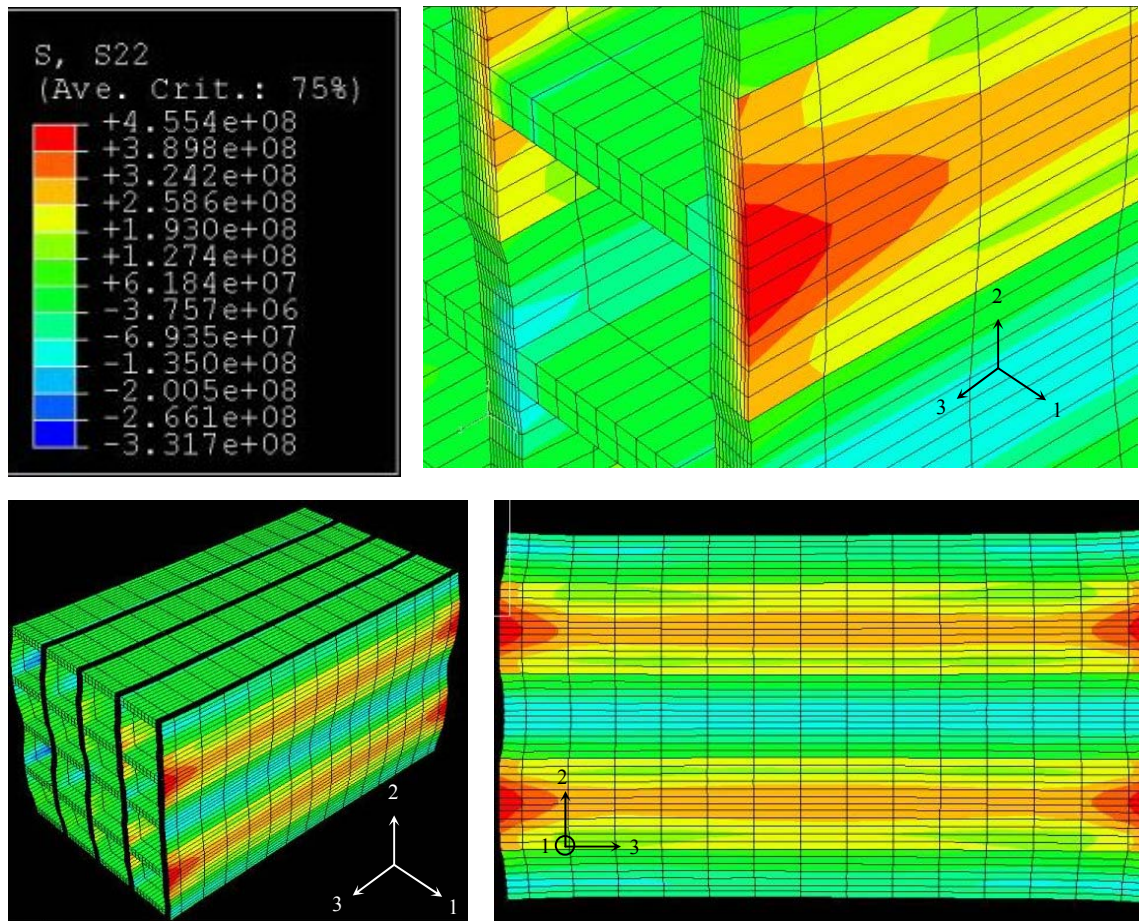
Figure A.8 Finite element results for the σ_{22} stress distribution in the Fe50Ni/YSZ platform.
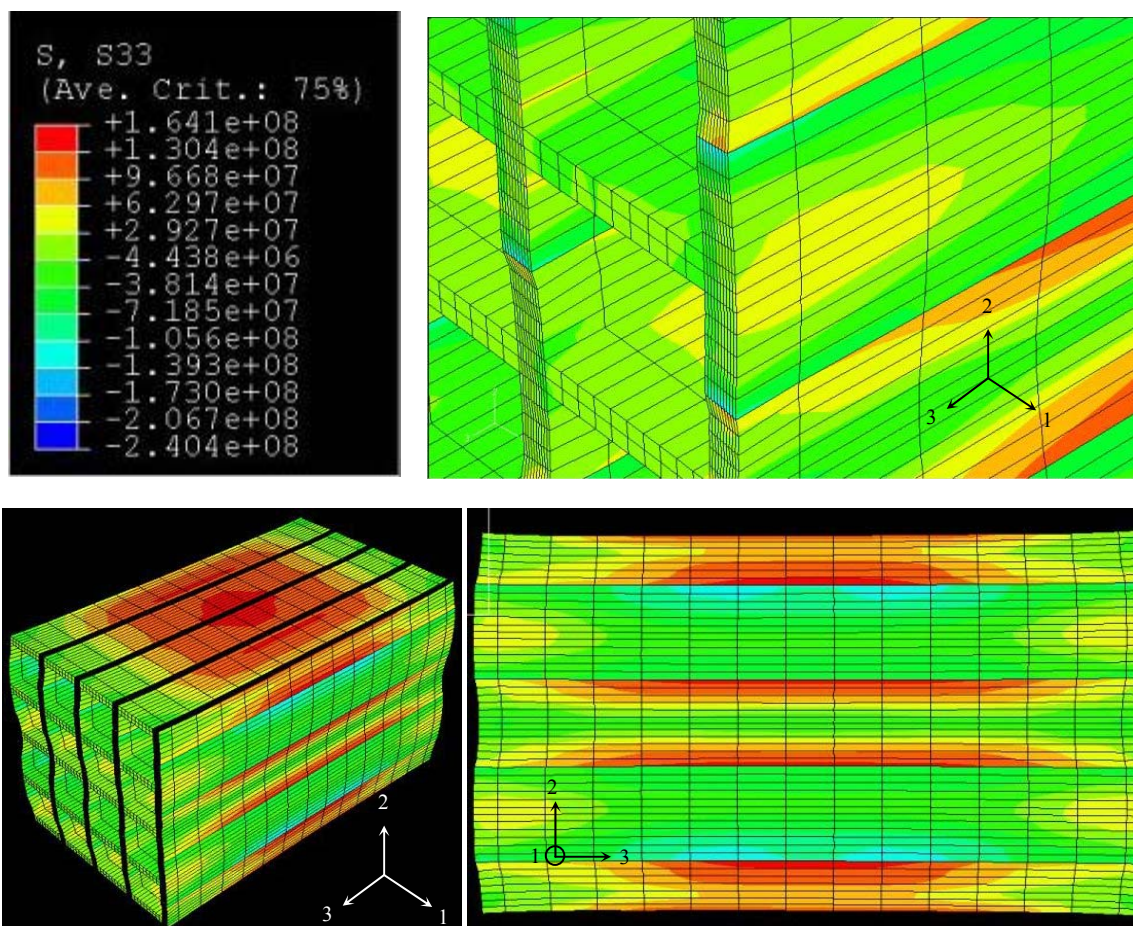
Figure A.9 Finite element results for the σ_{33} stress distribution in the Fe50Ni/YSZ platform.

References

1. LeMasters, J.A., *Thermal Stress Analysis of LCA-based Solid Oxide Fuel Cells*, in *Mechanical Engineering*. 2004, Georgia Institute of Technology: Atlanta, GA.

2. Grove, W.R., *On Voltaic Series and the Combination of Gases by Platinum.* Philos. Mag. Ser. 3, 1839. **14**: p. 127-30.

3. Minh, N.Q., *Ceramic Fuel Cells.* Journal of the American Ceramic Society, 1993. **76**(3): p. 563-88.

4. Singhal, S., *Ceramic Fuel Cells for Stationary and Mobile Applications.* American Ceramic Society Bulletin, 2003: p. 9601-9610.

5. Steele, B.C.H., *Material Science and Engineering: The Enabling Technology for the Commercialisation of Fuel Cell Systems.* Journal of Materials Science, 2001. **36**: p. 1053-68.

6. Kordesch, K. and G. Simader, *Fuel Cells and Their Applications*. 1996, New York: VCH Publishers, Inc.

7. Larminie, J. and A. Dicks, *Fuel Cell Systems Explained*. 2000, Chichester, West Sussex: J.Wiley.

8. Nernst, W., *Uber Die Elektrolytische Leitung Fester Korper Bei Sehr Hohen Temperaturen.* Z. Elektrochem., 1899. **6**: p. 41-43.

9. Möbius, H.H., *On the History of Solid Electrolyte Fuel Cells.* Journal of Solid State Electrochemistry, 1997. **1**: p. 2-16.

10. Badwal, S.P.S., F.T. Ciacchi, and D. Milosevic, *Scandia-Zirconia Electrolytes for Intermediate Temperature Solid Oxide Fuel Cell Operation.* Solid State Ionics, 2000. **136-137**: p. 91-99.

11. Kharton, V.V., et al., *Ceria-based Materials for Solid Oxide Fuel Cells.* Journal of Materials Science, 2000. **36**: p. 1105-17.

12. Ralph, J.M., A.C. Schoeler, and M. Krumpelt, *Materials for Lower Temperature Solid Oxide Fuel Cells.* Journal of Materials Science, 2001. **36**: p. 1161-72.

13. Yang, Z.G., J.W. Stevenson, and P. Singh, *Solid Oxide Fuel Cells.* Advanced Materials and Processes, 2003: p. 1-4.

14. Church, B.C., *Fabrication and Characterization of Solid Oxide Fuel Cell Interconnect Alloys*, in *Materials Science and Engineering*. 2004, Georgia Institute of Technology: Atlanta, GA.

15. Yang, Z.G., et al., *Selection and Evaluation of Heat-Resistant Alloys for SOFC Interconnect Applications.* Journal of the Electrochemical Society, 2003. **150**(9): p. A1188-A1201.

16. Cassidy, M., G. Lindsay, and K. Kendall, *The Reduction of Nickel-Zirconia Cermet Anodes and the Effects on Supported Thin Electrolytes.* Journal of Power Sources, 1996. **61**: p. 189-92.

17. Zhu, W.Z. and S.C. Deevi, *Development of Interconnect Materials for Solid Oxide Fuel Cells.* Materials Science and Engineering A, 2003. **A348**: p. 227-43.

18. Huang, K., P.Y. Hou, and J.B. Goodenough, *Characterization of Iron-Based Alloy Interconnects for Reduced Temperature Solid Oxide Fuel Cells.* Solid State Ionics, 2000. **129**: p. 237-50.

19. Tietz, F., H.-P. Buchkremer, and D. Stöver, *Components Manufacturing for Solid Oxide Fuel Cells.* Solid State Ionics, 2002. **152-53**: p. 373-81.

20. Hilpert, K., et al., *Chromium Vapor Species over Solid Oxide Fuel Cell Interconnect Materials and Their Potential for Degradation Processes.* Journal of the Electrochemical Society, 1996. **143**(11): p. 3642-47.

21. Zhu, W.Z. and S.C. Deevi, *Opportunity of Metallic Interconnects for Solid Oxide Fuel Cells: A Status on Contact Resistance.* Materials Research Bulletin, 2003. **38**: p. 957-72.

22. Ramanathan, L.V., *Corrosion Control with Rare Earths.* Corrosion Prevention and Control, 1998. **45**(3): p. 87-92.

23. *ASM Handbook Vol. 3, Alloy Phase Diagrams*. 1992, Materials Park, OH: ASM International.

24. Guillaume, C.E., *Recherches sur les aciers au nickel. Dilatations aux temperatures elevees; resistance electrique.* Acad. Sci., 1897. **125**: p. 235-38.

25. Abrikosov, I.A., O. Eriksson, and P. Soderlind, *Theoretical Aspects of the Fe_cNi_{1-c} Invar Alloy.* Physical Review B, 1995. **51**(2): p. 1058-63.

26. Schilfgaarde, M., I.A. Abrikosov, and B. Johansson, *Origin of the Invar Effect in Iron-Nickel Alloys.* Nature, 1999. **400**: p. 46-49.

27. Wassermann, E.F., *The Invar Problem.* Journal of Magnetism and Magnetic Materials, 1991. **100**: p. 346-62.

28.   Benbow, J. and B. J., *Paste Flow and Extrusion*. 1993, New York: Oxford University Press, Inc.

29.   Linderoth, S., et al., *Investigations of Metallic Alloys for Use As Interconnects in Solid Oxide Fuel Cell Stacks*. Journal of Materials Science, 1996: p. 5077-82.

30.   Oh, R., *The Influence of Honeycomb Dies on Paste Extrusion Mechanics*, in *Material Science and Engineering*. 2002, Georgia Insititue of Technology: Atlanta, GA.

31.   Hurysz, K.M., *Paste Extrusion for Fine Mechanics*, in *Materials Science and Engineering*. 2001, Georgia Institute of Technology: Atlanta, GA.

32.   Seay, W., *Capillary Rheometry Evaluation of Honeycomb Extrusion Pastes*, in *Material Science and Engineering*. 2001, Georgia Institute of Technology: Atlanta, GA.

33.   Rauch, W., et al. *Low Cost Solid Oxide Fuel Cell Stack Design Using Extruded Honeycomb Technology*. in *Eighth International Symposium on Solid Oxide Fuel Cells, SOFC VIII*. 2003. Paris, France.

34.   Liang, Z. and S. Blackburn, *Co-Extrusion of Solid Oxide Fuel Cell Elements*. Ceramic Engineering and Science Proceedings, 1999. **20**(4): p. 587-94.

35.   Crumm, A.T. and J.W. Halloran, *Fabrication of Microconfigured Multicomponent Ceramics*. Journal of the American Ceramic Society, 1998. **81**(4): p. 1053-57.

36.   Liang, Z. and S. Blackburn, *Design and Characterisation of a Co-extruder to Produce Trilayer Ceramic Tubes Semi-Continuously*. Journal of the European Ceramic Society, 2001. **21**: p. 883-92.

37.   Cochran, J., et al., *Extrusion and Thermo-chemical Processing of Layered Linear Cellular Alloys*. Materials Science Forum, 2003. **426-432**: p. 4295-4300.

38.   El-Geassy, A.A. and M.I. Nasr, *Effect of Sintering on the Structure of Hematite and Its Behavior During Reduction*. Canadian Metallurgy Quarterly, 1990. **29**(3): p. 185-91.

39.   Cores, A., et al., *Kinetic Irregularities in Joint Reduction of Nickel and Iron Oxides Under Non-Isothermal Conditions*. Ironmaking and Steelmaking, 1989. **16**(6): p. 446-49.

40.   Nasr, M.I., et al., *Effect of Nickel Oxide Doping on the Kinetics and Mechanism of Iron Oxide Reduction*. ISIJ International, 1995. **35**(9): p. 1043-1049.

41.   Nadler, J., *The Hydrogen Reduction of Iron and Chromium Oxides*, in *Materials Science and Engineering*. 2003, Georgia Institute of Technology: Atlanta, GA.

42. Clark, J.L., *Dynamic and Quasi-static Mechanical Properties of Fe-Ni Alloy Honeycomb*, in *Materials Science and Engineering*. 2004, Georgia Institute of Technology: Atlanta, GA.

43. Mak, T.C.W. and G.D. Zhou, *Crystallography in Modern Chemistry*. 1992, New York, NY: John Wiley and Sons.

44. Barsoum, M., *Fundamentals of Ceramics*. McGraw-Hill Series in Materials Science and Engineering. 1997, New York: McGraw-Hill.

45. Shaw, N.J., *Densification and Coarsening During Solid State Sintering of Ceramics: A Review of the Models I. Densification.* Powder Metallurgy International, 1989. **21**(3): p. 16-21.

46. Coble, R.L., *Effects of Particle Size Distribution in Initial-Stage Sintering.* Journal of the American Ceramic Society, 1973. **56**(9): p. 461-66.

47. Patterson, B.R. and L.A. Benson. *The Effect of Powder Size Distribution on Sintering*. in *Annual Powder Metallurgy Conference*. 1983. New Orleans, LA: Metal Powder Industries Federation.

48. Zheng, J. and R. J.S., *The Different Roles of Forming and Sintering on Densification of Powder Compacts.* American Ceramic Society Bulletin, 1992. **71**(9): p. 1410-16.

49. Bordia, R.K. and G.W. Scherer, *On Constrained Sintering - III. Rigid Inclusions.* Acta Metallurgica, 1988. **36**(9): p. 2411-16.

50. Bordia, R.K. and G.W. Scherer, *On Constrained Sintering - I. Constitutive Model for a Sintering Body.* Acta Metallurgica, 1988. **36**(9): p. 2393-97.

51. Bordia, R.K. and R. Raj, *Sintering Behavior of Ceramic Films Constrained by a Rigid Substrate.* Journal of the American Ceramic Society, 1985. **68**(6): p. 287-92.

52. Bordia, R.K. and A. Jagota, *Crack Growth and Damage in Constrained Sintering Films.* Journal of the American Ceramic Society, 1993. **76**(10): p. 2475-85.

53. Cai, P.Z., D.J. Green, and G.L. Messing, *Constrained Densification of Alumina/Zirconia Hybrid Laminates, I: Experimental Observation of Processing Defects.* Journal of the American Ceramic Society, 1997. **80**(8): p. 1929-39.

54. Cheng, T. and R. Raj, *Flaw Generation During Constrained Sintering of Metal-Ceramic and Metal-Glass Multilayer Films.* Journal of the American Ceramic Society, 1989. **72**(9): p. 1649-55.

55.   Champion, Y., et al., *Sintering of Copper Nanopowders Under Hydrogen: An In-Situ X-Ray Diffraction Analysis.* Materials Science and Engineering A, 2003. **A360**: p. 258-63.

56.   Nascimento, R.M., A.N. Klein, and A.E. Martinelli, *Microstructure and Thermal Expansion Behavior of Sintered Fe-Ni-Co Alloys.* The International Journal of Powder Metallurgy, 1998. **34**(6): p. 37-45.

57.   James, J.D., et al., *A Review of Measurement Techniques for the Thermal Expansion Coefficient of Metals and Alloys at Elevated Temperatures.* Measurement Science and Technology, 2001. **12**: p. R1-R15.

58.   Virkar, A.V., J.L. Huang, and R.A. Cutler, *Strengthening of Oxide Ceramics by Transformation- Induced Stresses.* Journal of the American Ceramic Society, 1987. **70**(3): p. 164-70.

59.   Chartier, T., D. Merle, and J.L. Besson, *Laminar Ceramic Composites.* Journal of the European Ceramic Society, 1995. **15**: p. 101-107.

60.   Bao, Y., S. Su, and J.L. Huang, *An Uneven Strain Model for Analysis of Residual Stress and Interface Stress in Laminate Composites.* Journal of Composite Materials, 2002. **36**(14): p. 1769-78.

61.   Sergo, V., et al., *Edge Stresses in Alumina/Zirconia Laminates.* Journal of the American Ceramic Society, 1997. **80**(7): p. 1633-38.

62.   Munz, D. and Y.Y. Yang, *Stresses Near the Free Edge of the Interface in Ceramic-to-Metal Joints.* Journal of the European Ceramic Society, 1994. **13**: p. 453-60.

63.   Eisele, P.L., *Characterization of Material Behavior During the Manufacturing Process of a Co-Extruded Solid Oxide Fuel Cell*, in *Mechanical Engineering.* 2004, Georgia Institute of Technology: Atlanta, GA.

64.   Hehn, L., et al., *Measurement of Residual Stresses in Al_2O_3/Ni Laminated Composites Using an X-Ray Diffraction Technique.* Journal of Materials Science, 1995. **30**: p. 1277-82.

65.   Shieu, F.-S. and S.L. Sass, *Dislocation Mechanisms for the Relaxation of Thermal Stress at Metal-Ceramic Interfaces.* Acta Metallurgica, 1991. **39**(4): p. 539-47.

66.   Ramakrishnan, N. and V.S. Arunachalam, *Effective Elastic Moduli of Porous Solids.* Journal of Materials Science, 1990. **25**: p. 3930-37.

67.   Bocchini, G.F., *The Influence of Porosity on the Characteristics of Sintered Materials.* The International Journal of Powder Metallurgy, 1986. **22**(3): p. 185-202.

68. Boccaccini, A.R., *Incorporation of Porosity to Control the Residual Thermal Stresses in Ceramic Composites and Laminates.* The European Physical Journal of Applied Physics, 1998. **2**: p. 197-202.

69. Chiu, C.-C., *Residual Stresses in Ceramic Coatings as Determined from the Curvature of a Coated Strip.* Materials Science and Engineering A, 1992. **A150**: p. 139-48.

70. Kese, K. and D.J. Rowcliffe, *Nanoindentation Method for Measuring Residual Stress in Brittle Materials.* Journal of the American Ceramic Society, 2003. **86**(5): p. 811-16.

71. Atar, E., et al., *Residual Stress Estimation of Ceramic Thin Films by X-Ray Diffraction and Indentation Techniques.* Scripta Materialia, 2003. **48**: p. 1331-36.

72. Adachi, T., et al., *Measurement of Microscopic Stress Distribution of Multilayered Composite by Residual Stress Analysis.* Materials Letters, 2003. **57**: p. 3057-62.

73. Pintschovius, L., et al., *Experimental and Theoretical Investigation of the Residual Stress Distribution in Brazed Ceramic-Steel Components.* Materials Science and Engineering A, 1994. **A177**: p. 55-61.

74. Cullity, B.D., *Elements of X-Ray Diffraction.* 2nd ed. 1978, Reading, MA: Addison-Wesley Publishing Company, Inc.

75. Noyan, I.C. and J.B. Cohen, *Residual Stress-Measurement by Diffraction and Interpretation.* 1987, New York: Springer-Verlag Inc.

76. Vermeulen, A.C., *The Sensitivity of Focusing, Parallel Beam and Mixed Optics to Alignment Errors in XRD Residual Stress Measurements.* Materials Science Forum, 2005. **490-91**: p. 131-136.

77. Yang, J. and J.I. Goldstein, *Magnetic Contribution to the Interdiffusion Coefficients in BCC (α) and FCC (γ) Fe-Ni Alloys.* Metallurgical and Materials Transactions A, 2004. **35A**: p. 1681-90.

78. Smithells, C.J., *Smithell's Metal Reference Book.* 7th ed, ed. E.A. Brandes and G. Brook. 1992, London: Butterworths.

79. Ivensen, V.A., *Densification of Metal Powders During Sintering.* 1973, New York, NY: Plenum Publishing Corp.

80. Matsuyama, M., K. Ashida, and T. Takeuchi, *Application of ^{63}Ni to the Reduction Mechanism of Fe-Ni Oxides.* Appl. Radiat. Isot., 1991. **42**(12): p. 1153-58.

81. Eigenmann, B., B. Scholtes, and E. Macherauch, Mat.-wiss. U. Werkstofftech, 1989. **20**: p. 314-25.

82. Tanji, Y., Y. Nakagawa, and S. Seinemann, *Anamalous Elastic Properties of Fe-Ni (fcc) Alloys and Their Invar Properties.* Physica B, 1982. **119**(1-2): p. 109-14.

83. Hausch, G. and H. Warlimont, *Single Crystalline Elastic Constants of Fe-Ni Invar Alloys.* Physics Letters A, 1972. **41**(5): p. 437-39.

84. Bower, D.I., E. Claridge, and I.S.T. Tsong, *Low Temperature Elastic Constants and Specific Heats of FCC Nickel-Iron Alloys.* Phys. Stat. Sol., 1968. **29**: p. 617-25.

85. Renaud, P. and S.G. Steinemann, *High Temperature Elastic Constanst of FCC Fe-Ni Invar Alloys.* Physica B, 1989. **161**: p. 75-78.

86. Schneider, S.J., ed. *Ceramics and Glasses*. Engineered Materials Handbook. Vol. 4. 1991, ASM International.

Vita

Raymond Oh was born on September 8, 1976 in Evanston, Illinois to Soo-Gun and Hyae-Young Lee Oh. He graduated in 1994 from Ewing High School in Ewing, NJ. After attending the University of Minnesota in Minneapolis, MN he graduated with a Bachelor of Science in Materials Science and Engineering in the spring of 1999. The following fall he enrolled in the graduate Materials Science and Engineering program at the Georgia Institute of Technology in Atlanta, GA, where he received his Masters of Science degree in May, 2002 with a thesis entitled "The Influence of Honeycomb Dies on Paste Extrusion Mechanics". Raymond received the degree Doctor of Philosophy in Materials Science and Engineering from Georgia Tech in May 2006.